

國立臺灣大學電機資訊學院光電工程學研究所



博士論文

Graduate Institute of Photonics and Optoelectronics
College of Electrical Engineering and Computer Science
National Taiwan University
Doctoral Dissertation

玻璃包覆晶體光纖之寬頻光子元件

Glass-Clad Crystal Fiber Based Broadband Photonic Devices

鄭東祐

Dong-Yo Jheng

指導教授：黃升龍 博士

Advisor: Sheng-Lung Huang, Ph.D.

中華民國 104 年 1 月

January, 2015

國立臺灣大學博士學位論文
口試委員會審定書

玻璃包覆晶體光纖之寬頻光子元件
Glass-Clad Crystal Fiber Based Broadband
Photonic Devices

本論文係鄭東祐君（學號 F95941056）在國立臺灣大學
光電工程學研究所完成之博士學位論文，於民國 104 年 1 月
27 日承下列考試委員審查通過及口試及格，特此證明

口試委員：

黃升龍

（指導教授）

賴映杰

孔文昌

林恭如

張宏鈞

王 倫

所 長

林恭如

中文摘要



寬頻光源是許多應用中的關鍵元件，例如光纖通訊以及光學同調斷層掃描術。本論文展示了以玻璃包覆之晶體光纖所製成之寬頻光子元件，所使用之晶體光纖，皆先以雷射加熱基座生長法生長單晶纖心，再以共提拉雷射加熱基座生長法進行玻璃包覆。

本論文展示了利用硼矽酸玻璃包覆摻鉻釷鋁石榴石晶體光纖所製作的高亮度寬頻光源。藉由最佳化退火參數，在低泵浦功率下其量子產率接近 95%。在功率為 1.4 瓦的藍光半導體雷射泵浦下，由直徑 25 微米的晶體纖心中輸出的螢光功率達到 19.9 毫瓦，對應的輸出亮度為每平方公釐每單位立體角 30.3 瓦特。此一高亮度寬頻光源適合應用在光學同調斷層掃描術。

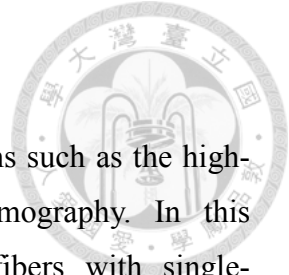
本文中成功製作出半球形外部共振腔摻鉻釷鋁石榴石雙纖衣晶體光纖雷射，其斜線效率達到 17.3%，閾值泵浦功率為 56 毫瓦。此外我們也建立了一套分佈式的數值模擬程式來模擬晶體光纖雷射與放大器，藉由擬合搭配不同穿透率輸出耦合透鏡的雷射效率，求得晶體光纖之傳輸損耗為每公分 0.01 分貝。同時我們也模擬了摻鉻釷鋁石榴石晶體光纖放大器的效能，當使用 10 公分長的高濃度摻鉻釷鋁石榴石晶體光纖時，得到在 1431 奈米波長下的峰值增益為 22.7 分貝。

本文中也發展出了可調波長的摻鉻釷鋁石榴石雙纖衣晶體光纖雷射，藉由旋轉準直式外部共振腔中的單片式雙折射濾波片，雷射輸出波長可由 1353 奈米調至 1509 奈米，閾值泵浦功率為 70 毫瓦。在調整輸出波長的過程中，也觀察到了由不同橫模干涉所導致的波長跳躍。

為了減少橫模數量與降低傳輸損耗，本文成功製作了由 N-SF57 與 N-LaSF9 兩種高折射率玻璃所包覆的少模純釷鋁石榴石晶體光纖，並對其特性進行量測。最後，我們也設計出由 N-LaSF9 與 N-LaSF41 玻璃所包覆的摻鉻釷鋁石榴石晶體光纖，可以在 1 到 1.7 微米的波長範圍內達到單一橫模導光。

關鍵字：晶體光纖、寬頻光源、可調波長雷射、摻鉻釷鋁石榴石、摻鉻釷鋁石榴石

Abstract



Broadband light sources are the key components in applications such as the high-capacity optical communication and the optical coherence tomography. In this dissertation, broadband photonic devices based on glass-clad fibers with single-crystalline cores were demonstrated. The cores of crystal fibers were grown with the laser-heated pedestal growth (LHPG) method, and then cladded with glass using the co-drawing LHPG process.

High-brightness broadband light source was presented with the Pyrex-clad Ce^{3+} :YAG crystal fiber pumped with a blue laser diode. By optimizing the annealing conditions, the quantum yield under low pump power was estimated to be 95%. A 19.9-mW fluorescence output from the crystal fiber core with a 25- μm diameter was achieved with a 1.4-W pump power, and the corresponding radiance was $30.3 \text{ W mm}^{-2} \text{ sr}^{-1}$. This high-brightness broadband light source is useful for the optical coherence tomography.

Hemispherical external-cavity Cr^{4+} :YAG double-clad crystal fiber lasers have been demonstrated with a 17.3% slope efficiency and a 56-mW threshold pump power. A simulation program with distributed model for the crystal fiber laser and amplifier was developed. The propagation loss extracted by fitting the laser performances with different output couplers was 0.01 dB/cm. Performance of the Cr^{4+} :YAG crystal fiber amplifiers were also simulated, and a 22.7-dB gain at 1431 nm can be achieved with a 10-cm crystal fiber with enhanced concentration.

Broadband tunable laser from 1353 to 1509 nm was demonstrated with the Cr^{4+} :YAG double-clad crystal fiber. The laser output wavelength was tuned by rotating a single-plate birefringent filter within the collimated external cavity. The laser threshold was 70 mW in the presence of the birefringent filter. The wavelength tuning was discrete due to the interference between the transverse modes.

High-index-glass-clad crystal fibers have been developed for decreasing the number of transverse modes and reducing the propagation loss. Few-mode pure YAG crystal fibers cladded with N-SF57 and N-LaSF9 glasses were successfully fabricated. Finally, we also proposed designs of N-LaSF9-clad and N-LaSF41-clad Cr^{4+} :YAG crystal fibers which can achieve single-mode guiding over the wavelength range from 1 to 1.7 μm .

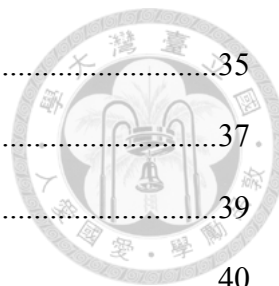
Key words: crystal fiber, broadband light source, tunable laser, Cr^{4+} :YAG, Ce^{3+} :YAG

Table of Contents

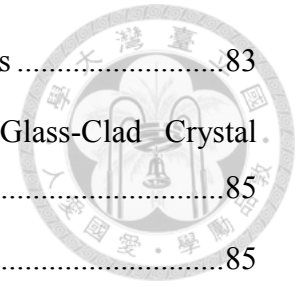


中文摘要	i
Abstract	ii
Table of Contents	iii
List of Figures	vi
List of Tables	xiii
Chapter 1 Introduction.....	1
Chapter 2 Theory of Crystal Fiber Light Sources	5
2.1 Energy Diagram and Rate Equations of Ce ³⁺ :YAG Crystals.....	5
2.1.1 Energy Diagram of Ce ³⁺ :YAG	5
2.1.2 Rate Equations of Ce ³⁺ :YAG	9
2.2 Energy Diagram and Rate Equations of Cr ⁴⁺ :YAG	12
2.2.1 Energy Diagram of Cr ⁴⁺ :YAG	12
2.2.2 Rate Equations of Cr ⁴⁺ :YAG.....	18
2.3 Power Evolution Equations of Broadband Light Propagating in Crystal Fibers	20
2.3.1 Broadband Spontaneous Emission in Crystal Fibers.....	21
2.3.2 Power Evolution Equations in Crystal Fibers.....	22
2.4 Conversion Efficiency and Brightness of Broadband Light Sources	23
2.5 Modeling of Crystal Fiber Lasers and Amplifiers	29
2.5.1 The Lumped Model for Cr ⁴⁺ :YAG Crystal Fiber Laser.....	29
2.5.2 The Distributed Model for Cr ⁴⁺ :YAG Crystal Fiber Laser	31
Chapter 3 High-Brightness Broadband Light Sources by Ce³⁺:YAG Crystal Fibers	35
3.1 Fabrication of Ce ³⁺ :YAG Crystal Fibers.....	35

3.1.1	Laser-Heated Pedestal Growth System.....	35
3.1.2	Single Crystal Fiber Growth.....	37
3.1.3	Thermal Annealing	39
3.1.4	Glass Cladding Process.....	40
3.2	Conversion Efficiency Optimization of Ce ³⁺ :YAG Crystal Fibers.....	41
3.3	High-Brightness Ce ³⁺ :YAG Crystal Fiber Light Source.....	44
Chapter 4 Broadly Tunable and Low-Threshold Cr⁴⁺:YAG Double-Clad Crystal Fiber Lasers.....		50
4.1	Fabrication of Cr ⁴⁺ :YAG Double-Clad Crystal Fibers for Laser Applications	50
4.1.1	Double-Clad Crystal Fiber Growth	50
4.1.2	Dielectric Coating Deposition	53
4.2	Fluorescence Lifetime Thermal Loading and Polarization-Dependent Gain of Cr ⁴⁺ :YAG Double-Clad Crystal Fiber	55
4.2.1	Fluorescence Lifetime Thermal Loading.....	55
4.2.2	Polarization-Dependent Gain.....	57
4.3	Efficient and Low-Threshold External-Cavity Crystal Fiber Lasers.....	59
4.3.1	Hemispherical External-Cavity Crystal Fiber Lasers	60
4.3.2	Collimated External-Cavity Crystal Fiber Lasers.....	63
4.4	Broadly-Tunable Crystal Fiber Lasers.....	67
4.4.1	Wavelength Tuning with Uncoated Pellicle Etalon	67
4.4.2	Wavelength Tuning with Diffraction Grating	69
4.4.3	Wavelength Tuning with Birefringent Filter.....	72
4.5	Design of Cr ⁴⁺ :YAG Crystal Fiber Amplifiers	74
Chapter 5 Toward Single-Mode YAG Crystal Fibers.....		81
5.1	Tuning Glass Refractive Index with Annealing Treatment	81



5.2	Characteristics of High-Index-Glass-Clad Crystal Fibers	83
5.3	Measuring the Guiding Properties of High-Index-Glass-Clad Crystal Fibers	85
5.3.1	Refractive Index Profiling	85
5.3.2	Near-Field Mode Imaging	86
5.3.3	Far-Field Intensity Distribution	87
5.4	High-Index-Glass-Clad Pure YAG Crystal Fibers	89
5.4.1	Few-Mode N-SF57-Clad YAG Crystal Fiber	89
5.4.2	Few-Mode N-LaSF9-Clad YAG Crystal Fiber	90
5.5	Design of Single-Mode Cr ⁴⁺ :YAG Crystal Fiber.....	93
Chapter 6	Conclusions and Future Work.....	98
References	100



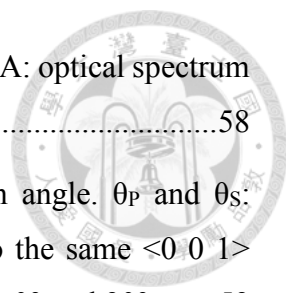
List of Figures



Fig. 2.1.	Detailed energy diagram of Ce ³⁺ :YAG [27].	5
Fig. 2.2.	Ground state absorption cross section of Ce ³⁺ :YAG. Calculated from data in [27].	6
Fig. 2.3.	Ce ³⁺ :YAG fluorescence spectrum at room temperature. Solid line: measured fluorescence line shape. Dashed line: fitted fluorescence line shape. Dotted line: calculated emission cross section.	8
Fig. 2.4.	The net signal cross section of Ce ³⁺ :YAG [27].	9
Fig. 2.5.	Simplified energy diagram of Ce ³⁺ :YAG. Solid arrows: absorptive or emissive transitions. Dotted arrows: non-radiative relaxations.	10
Fig. 2.6.	Schematic of the Cr:YAG crystal structure	13
Fig. 2.7.	The Tanabe-Sugano diagram for d ₂ configuration in tetrahedral coordination [37]. The vertical dashed line indicates the crystal field strength of YAG crystal.	14
Fig. 2.8.	Energy level diagram of the Cr ⁴⁺ ions doped in YAG host. Center wavelength of the pump absorption: λ _{p1} = 609 nm, λ _{p2} = 665 nm, λ _{p3} = 893 nm, λ _{p4} = 1034 nm, λ _{p5} = 1124 nm [38].	14
Fig. 2.9.	Ground-state absorption spectra of Cr ³⁺ and Cr ⁴⁺ ions in YAG [39].	15
Fig. 2.10.	Fluorescence lifetime of the Cr ⁴⁺ :YAG crystal.	16
Fig. 2.11.	Cr ⁴⁺ :YAG emission spectra. Solid line: measured fluorescence line shape. Dashed line: fitted fluorescence line shape. Dotted line: calculated emission cross section spectrum.	17
Fig. 2.12.	Simplified Cr ⁴⁺ :YAG energy diagram. Solid arrows: radiative transitions. Dotted arrows: non-radiative transitions.	19
Fig. 2.13.	A schematic drawing of the crystal fiber broadband light source.	24
Fig. 2.14.	Reflectance at the crystal fiber end face for different polarization states. The rays propagates with angles in the shaded region are unguided by the crystal	

	fiber.....	25
Fig. 2.15.	Radiance intensity distribution of Ce^{3+} :YAG crystal fiber. Unit: $W\ sr^{-1}$	27
Fig. 2.16.	The conversion efficiency of Ce^{3+} :YAG crystal fiber broadband light source versus the numerical aperture of the collection lens.....	28
Fig. 2.17.	Radiance distribution of the Ce^{3+} :YAG crystal fiber broadband light source. The radial unit is $W\ mm^{-2}\ sr^{-1}$. The shape is different from radiance intensity distribution in Fig. 2.15 due to the $\cos\theta$ term in Eq. (2.50).....	29
Fig. 2.18.	Schematic of boundary conditions in crystal fiber laser modeling.....	32
Fig. 2.19.	Comparison between the lumped model and the distributed model. The thin lines are for $L = 2$ mm and the thick lines are for $L = 50$ mm. Solid lines: lumped model. Dashed lines: distributed model.....	34
Fig. 2.20.	The intra-cavity pump power distribution along the crystal fiber. Solid line: lumped model. Dashed line: distributed model.....	34
Fig. 3.1.	Schematic of the LHPG system. $M_1 \sim M_5$: mirrors. PC: personal computer.....	36
Fig. 3.2.	A schematic illustration of the growth chamber. The CO_2 laser beam after the reflexicon is a doughnut-shaped beam instead of two split beams.....	37
Fig. 3.3.	Illustrations of the single crystal fiber growth. Left: Before the crystal fiber growth. Right: During the crystal fiber growth.....	38
Fig. 3.4.	Annealing temperature profiles with a soaking time of 4 hours. Solid line: programed profile. Dashed line: Actual profile.....	40
Fig. 3.5.	Left: Illustration of the glass cladding process. Right: Photo of the crystal fiber during the cladding process.....	41
Fig. 3.6.	Setup for measuring the forward fluorescence. LD: laser diode. L_1-L_3 : aspheric lenses. LPF: long-wavelength-pass filter. PD: photo diode.....	42
Fig. 3.7.	Fluorescence power versus absorbed pump power for an as-grown crystal fiber and a crystal fiber annealed with 1-hr soaking time.....	43
Fig. 3.8.	Conversion efficiency versus the 1000 °C soaking time.....	44
Fig. 3.9.	The backward fluorescence measurement setup. BBM: broadband mirror. L_1	

	and L ₂ : aspheric lenses. DBS: dichroic beam splitter. LD: laser diode. PD: photo diode. Solid arrow: pump propagation direction. Hollow arrow: fluorescence propagation direction.....	45
Fig. 3.10.	The output fluorescence power versus the incident pump power.....	46
Fig. 3.11.	Normalized fluorescence spectra of the Ce ³⁺ :YAG backward fluorescence with and without BBM.	46
Fig. 3.12.	Radiance distribution of the high-brightness crystal fiber light source. The unit of the radial scale is W mm ⁻² sr ⁻¹	47
Fig. 3.13.	Setup of SMF28e-pigtailed Ce ³⁺ :YAG light source.	48
Fig. 3.14.	Fluorescence power output from SMF28e fiber.	48
Fig. 3.15.	Fluorescence spectrum output from SMF28e fiber.	49
Fig. 4.1.	An illustration of the CD-LHPG growth of the Cr ⁴⁺ :YAG double-clad crystal fiber. The inset photo showing the funnel-shpaed molten zone was captured during the fiber growth.	51
Fig. 4.2.	An illustration of sapphire-tube-assisted LHPG system.....	52
Fig. 4.3.	Refractive index profile of a Cr ⁴⁺ :YAG double-clad crystal fiber.....	53
Fig. 4.4.	Transmission spectra of the coatings on both ends of the crystal fiber.	54
Fig. 4.5.	End photo of coated crystal fiber. (a) Input end (HR), (b) Output end (AR).	54
Fig. 4.6.	Fluorescence lifetime measurement setup. LD: laser diode; L ₁ ~L ₅ : aspheric lenses; C: chopper; HWP: half-wave plate; LPF: long-wavelength-pass filter; PD: photo diode.	55
Fig. 4.7.	Decay of the fluorescence intensity after blocking-off the pump. Blue dots: measured data. Red line: the exponential fit with a time constant of 4.17 μs.	56
Fig. 4.8.	Fluorescence lifetime vs. absorbed pump power for bulk and crystal fiber.....	57
Fig. 4.9.	The polarization-dependent gain measurement setup. LD: laser diode; L ₁ ~L ₅ : lenses; HWP: half-wave plate; BS: beam splitter; ND: neutral density	



filter; P: polarizer; LPF: long-wavelength pass filter; OSA: optical spectrum analyzer.....58

Fig. 4.10. The double-pass gross gain vs. the pump polarization angle. θ_P and θ_S : polarization angles of pump and signal with respect to the same $\langle 0 0 1 \rangle$ crystal axis, respectively. The $\langle 0 0 1 \rangle$ crystal axes are at 0° and 90°59

Fig. 4.11. The double-pass gross gain vs. the signal polarization angle.59

Fig. 4.12. Setup of the hemispherical ECCFL.60

Fig. 4.13. Transmission spectra of the output couplers.....61

Fig. 4.14. Residual pump power of Cr^{4+} :YAG crystal fiber.....61

Fig. 4.15. The performance of the hemispherical ECCFL with different output coupler transmittance. Markers: measured data. Solid lines: numerical simulation.62

Fig. 4.16. Laser output spectrum under 400-mW pump power. The resolution of the OSA is 0.08 nm. OSNR: optical signal-to-noise ratio.62

Fig. 4.17. The experiment setup for measuring the loss of the collimated external cavity. M: HR mirror; FC: fiber coupler; Numbers: number of ports of FC. The slashes indicate the FC/APC connectors.64

Fig. 4.18. The measured external cavity loss with different intra-cavity collimators. Refer to Table 4.2 for lens details.65

Fig. 4.19. Collimated ECCFL setup.....66

Fig. 4.20. Performance of collimated ECCFL.66

Fig. 4.21. Output spectrum of collimated ECCFL. The resolution bandwidth of the optical spectrum analyzer is 0.07 nm.67

Fig. 4.22. Transmittance of Thorlabs BP108 uncoated pellicle beamsplitter with a 45° angle of incidence [60].68

Fig. 4.23. Setups of tunable ECCFLs with uncoated pellicle beamsplitter. Upper: hemispherical cavity. Lower: collimated cavity.69

Fig. 4.24. Laser peak wavelengths vs. pellicle tilt angle in the hemispherical and the collimated ECCFLs.69

Fig. 4.25.	Setup of the tunable ECCFL with a Littrow-mounted diffraction grating. DG: diffraction grating.	70
Fig. 4.26.	Diffraction efficiency of the grating. Measured near the Littrow configuration.	70
Fig. 4.27.	Output power of the tunable ECCFL with a Littrow-mounted grating at the laser peak wavelength of 1452 nm.	71
Fig. 4.28.	The laser tuning spectrum and the laser output spectra at the two extreme wavelengths. The laser tuning spectrum was recorded using the “maximum hold” function of the optical spectrum analyzer while rotating the diffraction grating.	71
Fig. 4.29.	Setup of the tunable ECCFL with a birefringent filter.	72
Fig. 4.30.	Laser wavelength vs. the rotation angle of the BRF. Dashed line: Theoretical tuning curves of the BRF. Dots: Measured laser wavelengths. Background contours: Single-pass p-polarized transmittance of the BRF.	72
Fig. 4.31.	Dots: The laser output power vs. laser output wavelengths under 400-mW pump power. Lines: four example spectra lasing at 1357, 1393, 1443, and 1494 nm. The OSA resolution bandwidth is 1 nm.	73
Fig. 4.32.	Output beam profile at the laser wavelength of 1477 nm.	74
Fig. 4.33.	Schematic plots of different Cr ⁴⁺ :YAG crystal fiber amplifier schemes. (a) SPSP; (b) SPDP; (c) DPDP.	75
Fig. 4.34.	Performance of different schemes of the Cr ⁴⁺ :YAG crystal fiber amplifier. The input signal power is -30 dBm and the fiber length is 10 cm.	76
Fig. 4.35.	Excited state population of different schemes of Cr ⁴⁺ :YAG crystal fiber amplifiers. The pump power is 1 watt and the crystal fiber length is 20 cm. The lines of the SPSP and the SPDP schemes are very close.	77
Fig. 4.36.	Simulated optical gain versus the length of Cr ⁴⁺ :YAG crystal fibers with different Cr ⁴⁺ concentrations under 10-W and 2-W pumping in the DPDP scheme.	78
Fig. 4.37.	Simulated optical gain versus total pump power under different input signal	

	power. The length of the crystal fiber is 20 cm. The lines with the input signal from -30 dBm to -10 dBm are very close to each other.....	79
Fig. 4.38.	Gain versus the input signal level for a 10-cm long crystal fiber.....	79
Fig. 4.39.	Small-signal gain spectra of a 10-cm long Cr ⁴⁺ :YAG crystal fiber under different pump powers.....	80
Fig. 5.1.	Dispersion curves of YAG and 4 types of high-index glasses from 0.4 to 1.8 μm.....	82
Fig. 5.2.	The changes of refractive indices of several glass types as functions of the annealing rate.....	83
Fig. 5.3.	Number of LP modes of an optical fiber per one polarization [48].....	84
Fig. 5.4.	The V value of an N-LaSF41-clad crystal fiber with a core diameter of 20 μm. The cladding index was assume to be the bulk index. The shaded region indicates the wavelength range of single-mode operation.....	85
Fig. 5.5.	Experimental setup for imaging the modes of the HIGC crystal fiber. OBJ ₁ and OBJ ₂ : objective lenses; BS: beam splitter; TL: tube lens; EP: eye piece; CF: crystal fiber; L: aspheric lens; CCD: charge-coupled device.....	87
Fig. 5.6.	Experimental setup of measuring the far-field distribution of the HIGC crystal fiber.....	87
Fig. 5.7.	Schematic illustration of the rays propagate in and output from an unguided crystal fiber.....	88
Fig. 5.8.	The near-field mode profiles of the N-SF57-clad YAG crystal fiber measured at (a) 780 nm, (b) 633 nm, and (c) 532 nm. (d) Simulated profile using the intensities of the lowest 4 modes.....	90
Fig. 5.9.	Microscope photos of the N-LaSF9-clad YAG crystal fiber endface, (a) bright field (left), (b) dark field (right). The diameters of the fiber core and cladding are 40 and 945 μm, respectively.....	91
Fig. 5.10.	Near-field mode profiles of the as-grown N-LaSF9-clad YAG-core fiber measured at (a) 532 nm, (b) 633 nm, (c) 780 nm, and (d) 1064 nm.....	91
Fig. 5.11.	Far-field intensity distribution of the as-grown N-LaSF9-clad pure YAG	

	crystal fiber measured at (a) 650 nm, (b) 780 nm, and (c) 1064 nm. The growth speed was 2 mm/min.	92
Fig. 5.12.	The far-field intensity distribution of the N-LaSF9-clad pure YAG crystal fiber with a 10-mm/min growth speed at (a) 650 nm, (b) 780 nm, (c) 1064 nm and (d) 1550 nm.	93
Fig. 5.13.	Dispersion curves of YAG and the 4 high-index glasses from 950 nm to 1750 nm.	94
Fig. 5.14.	The V values of the N-LaSF9-clad crystal fibers with an index drop of -0.0086 in the cladding due to fast annealing. The gray horizontal lines represents $V=2.405$, below which the fiber is single-mode.	95
Fig. 5.15.	The V values of the N-LaSF41-clad crystal fibers with an index rise of 0.0011 in the cladding due to slow annealing.	95
Fig. 5.16.	The V values of the N-SF57-clad crystal fibers with an index rise of 0.0026 in the cladding due to slow annealing.	96
Fig. 5.17.	The V values of the SF57-clad crystal fibers with an index rise of 0.0011 in the cladding due to slow annealing.	96

List of Tables



Table 2.1.	Summary of optical parameters of Ce^{3+} :YAG	12
Table 2.2.	Summary of optical parameters of Cr^{4+} :YAG.....	20
Table 3.1.	Characteristics of Ce:YAG crystal fiber light source and Thorlabs high-power LED light sources. [56].....	47
Table 4.1.	Cavity parameters used in the simulation. The values of R_2^p and R_2^s vary with the output couplers.....	63
Table 4.2.	Lenses used in the measurement of round-trip loss of the collimated external cavity.....	64
Table 5.1.	List of Sellmeier constants of YAG and high-index glasses.....	82
Table 5.2.	The transition temperatures, the softening temperatures, and the annealing coefficients of the high-index glasses.....	83
Table 5.3.	Properties of the designed single-mode Cr^{4+} : YAG crystal fibers with different high-index glass cladding.....	97

Chapter 1

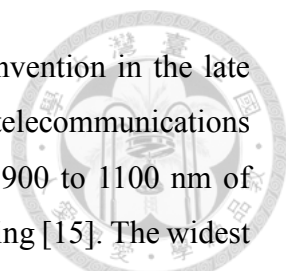
Introduction



Optical coherence tomography is an imaging technique which allows *in situ* examination of the biomedical tissues [1]. The axial resolution is inversely proportional to the bandwidth of the light source. A light source with non-Gaussian spectrum would lead to side-lobes in the detected signal, and thus result in false structures in the final image [2]. Therefore, a broad and Gaussian-like source spectrum is preferred in the optical coherence tomography system. In addition to the spectral shape, brightness of the light source is also important for the signal to noise ratio. Conventional incandescent sources, such as the tungsten-halogen lamp, offer broad and smooth spectra, whereas the brightness is low due to the large emitter size. Supercontinuum light source [3] has ultra-high brightness across a broad wavelength range, but there are many structures in the output spectrum, and the cost is high due to the requirement of the ultra-fast pump source. The fluorescence spectra of some solid-state crystals, such as $\text{Ce}^{3+}:\text{YAG}$, $\text{Ti}^{3+}:\text{Al}_2\text{O}_3$, $\text{Cr}^{4+}:\text{Mg}_2\text{SiO}_4$, and $\text{Cr}^{4+}:\text{YAG}$, are broadband and Gaussian-like, but brightness of the fluorescence output from the bulk crystal is usually low due to the divergence of both pump and fluorescence lights.

Optical communication is another field demanding the broadband light sources [4]. After the invention of the zero-water-peak glass fibers [5], the transmission window of the fiber network spans from 1280 to 1630 nm. There are mature technologies such as the erbium-doped fiber amplifier [6] and the semiconductor optical amplifier [7], but the operation bandwidth of a single device is still limited. New technologies possible to cover the whole communication windows include the bismuth doped fibers [8] and the $\text{Cr}^{4+}:\text{YAG}$ crystal fibers.

The $\text{Ce}^{3+}:\text{YAG}$ was first reported in 1967 [9] as a new phosphor material for uses in the cathode-ray tubes. It has a near-unity quantum yield and a short lifetime of about 68 ns. $\text{Ce}^{3+}:\text{YAG}$ has a broadband yellow emission spectrum from 500 to 700 nm. There are two absorption peaks centered at 340 and 450 nm. Since the invention of the high-efficiency GaN light-emitting diodes [10], $\text{Ce}^{3+}:\text{YAG}$ has been the most common phosphor used in the white light-emitting diode, due to its high conversion efficiency and the high color rendering index of the mixed white light [11].



The Cr⁴⁺:YAG crystal has been extensively studied since its invention in the late 1980s [12]. The broadband emission from 1.2–1.7 μm is usable in telecommunications [13] and remote sensing [14]. The wide absorption spectrum from 900 to 1100 nm of Cr⁴⁺:YAG is also attractive due to the feasibility of direct diode pumping [15]. The widest laser tuning range without replacing cavity optics was 230 nm (1340–1570 nm) [16]. The typical threshold pump power ranges from 400 mW [17] to more than 1 watt [16], [18].

Crystal fibers provide large surface-area-to-volume ratio than bulk crystal, hence the thermal dissipation is better. The crystal fiber is also more efficient than bulk laser in the aspect of the pump confinement. For example, considering a Cr⁴⁺:YAG bulk laser with a 1064-nm pump, the Rayleigh range of the pump beam with 20-μm 1/e² focal diameter in the crystal is about 1.07 mm. Since the typical length for a crystal fiber with a 20-μm core diameter is several centimeters, high pumping and lasing intensity can be maintained in the crystal fiber over a length more than an order of magnitude longer than in the bulk crystal. Therefore, the threshold pump power of the crystal fiber laser can be significantly lower than a bulk laser, due to a much higher averaged pump intensity. For broadband incoherent light sources with bulk crystals, the fluorescence emitted from different axial positions leads to lower brightness. With a crystal fiber, all fluorescence power collected by the waveguide structure exit from the small core area on the output end, resulting in higher brightness than the bulk crystals.

The laser-heated pedestal growth (LHPG) method is a crucible-free crystal growth technique which can fabricate high-quality small-diameter crystal fibers with low contamination [19]. A modification of this method, the co-drawing LHPG method, is capable of cladding the crystal fiber with glass to reduce the propagation loss [20], and reducing the core diameter for the double-clad crystal fibers with fused silica as the cladding material [13]. The sapphire-tube-assisted co-drawing LHPG method enhances the temperature stability with the heat-capacitance of a sapphire tube, result in improved core uniformity and lower propagation loss [21].

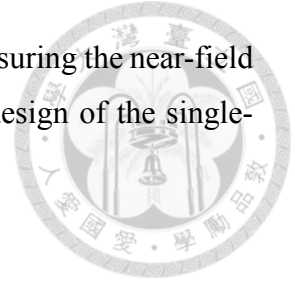
High-brightness white light source based on diode-pumped Ce³⁺:YAG double-clad crystal fiber has been demonstrated in the previous work [22]. Efficient Cr⁴⁺:YAG crystal fiber laser has also been demonstrated with an 80-mW threshold pump power with only passive cooling [23]. The laser cavity was formed by multilayer coatings deposited on both ends of the crystal fiber and the output wavelength was free-running at 1420.27 nm.

For a tunable laser, the cavity should be extended to outside of the crystal fiber, so a wavelength selective element can be incorporated.

Reducing the number of the guided modes can enhance the beam quality output from the crystal fiber. Decreasing the index difference between the core and the cladding can also lower the propagation loss [24]. For tunable laser applications, single-mode crystal fibers can avoid the wavelength hopping due to the multimode-interference effect. Methods for reducing the mode numbers in waveguides with single-crystalline cores include the adhesive-free crystal bonding [25], the ceramics cladding [26], and the high-index glass cladding.

The dissertation contains four main chapters. In chapter 2, the theories of the crystal fiber broadband light sources were introduced. The energy diagrams and the rate equations of $\text{Ce}^{3+}:\text{YAG}$ and $\text{Cr}^{4+}:\text{YAG}$ are introduced. A spectrally-resolved distributed model of the broadband crystal fiber light source was described, as well as another simpler model for estimating the conversion efficiency and the brightness of incoherent light sources. In chapter 3, high brightness light source based on $\text{Ce}^{3+}:\text{YAG}$ crystal fiber with a single-layer Pyrex cladding is demonstrated. By optimizing the thermal annealing conditions, the conversion efficiency approached the theoretical limit under 100-mW pumping. A 19.9-mW fluorescence power was emitted from the fiber core with 25- μm diameter under 1.4 W pumping, corresponding to a radiance of $30.3 \text{ W mm}^{-2} \text{ sr}^{-1}$. Chapter 4 presents a passively-cooled tunable $\text{Cr}^{4+}:\text{YAG}$ crystal fiber laser with a low threshold pump power and a broad tuning range. Both hemispherical and collimated external-cavity crystal fiber lasers (ECCFLs) were built for the tunable laser experiment. The loss of the collimated external cavity was evaluated and found to be smaller for the intra-cavity collimators with shorter focal lengths. The slope efficiency and the threshold pump power were 17.3% and 56 mW for the hemispherical external-cavity crystal fiber laser, and 13% and 104 mW for the collimated ECCFL. Moreover, tunable lasers have been demonstrated by using the diffraction grating, the pellicle beam splitter, or the birefringent filter (BRF) as the wavelength tuning elements. By rotating the single-plate BRF in the collimated ECCFL, a tuning range of 156 nm was obtained without any re-alignment of the laser cavity. The threshold pump power at the peak wavelength was 70 mW with the BRF. In chapter 5, the design, fabrication, and characterization of the high-index-glass-clad crystal fibers are described. N-SF57-clad and N-LaSF9-clad pure YAG crystal fibers were

fabricated, and their waveguide properties were characterized by measuring the near-field mode profiles and the far-field intensity distributions. Finally, the design of the single-mode Cr⁴⁺:YAG crystal fiber was proposed.





Chapter 2

Theory of Crystal Fiber Light Sources

In this chapter, we describe the theoretical background of $\text{Ce}^{3+}:\text{YAG}$ and $\text{Cr}^{4+}:\text{YAG}$ crystals.

2.1 Energy Diagram and Rate Equations of $\text{Ce}^{3+}:\text{YAG}$ Crystals

2.1.1 Energy Diagram of $\text{Ce}^{3+}:\text{YAG}$

Cerium is a rare-earth element with the electronic configuration of $[\text{Xe}]4f^15d^16s^2$. At trivalent state there is a single 4f electron outside the xenon core. The energy diagram of Ce^{3+} ions doped in YAG is shown in Fig. 2.1.

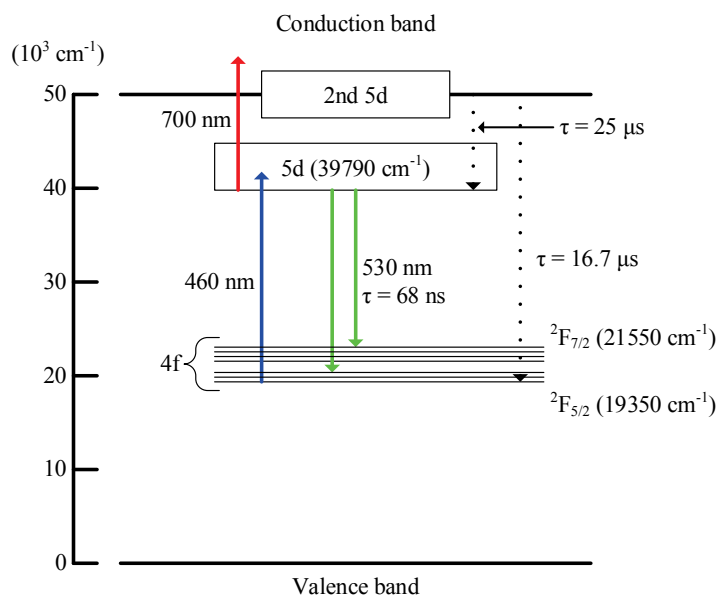


Fig. 2.1. Detailed energy diagram of $\text{Ce}^{3+}:\text{YAG}$ [27].

The broadband yellow emission comes from the transition between the 4f and 5d orbitals. The 4f orbital is not sensitive to the crystal field due to the shielding of the outer $5s^25p^6$ orbitals. The spin-orbit coupling splits the 4f states into $^2F_{5/2}$ and $^2F_{7/2}$ with the latter unoccupied at room temperature. However, the crystal field effect has strong impact on the excited 5d state. The 5d orbitals are split by the crystal field and appear as broad bands at room temperature. Many of the 5d bands lie above the conduction band of the

YAG crystal except the lowest two. The second lowest 5d bands partially overlaps with the conduction band.

The ground state absorption (GSA) spectrum of $\text{Ce}^{3+}:\text{YAG}$ is shown in Fig. 2.2. The two broad peaks centered at 460 nm and 340 nm correspond to the transition from the $^2F_{5/2}$ level to the lowest and the second lowest 5d bands, respectively. When the electron is excited to the upper 5d bands, it can non-radiatively relax to the lowest 5d bands with a lifetime less than 2 ns [28].

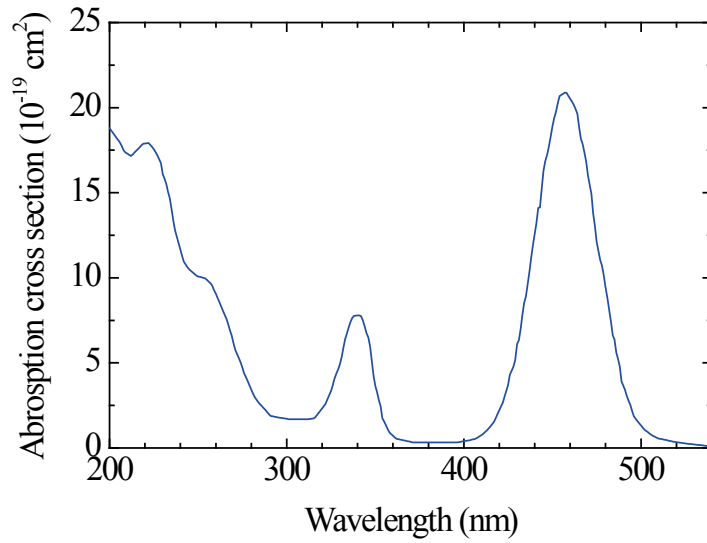


Fig. 2.2. Ground state absorption cross section of $\text{Ce}^{3+}:\text{YAG}$. Calculated from data in [27].

The broadband fluorescence of $\text{Ce}^{3+}:\text{YAG}$, as shown in Fig. 2.3, consists of two unresolved peaks which correspond to the transition from the lowest 5d band to $^2F_{5/2}$ and $^2F_{7/2}$ levels. The fluorescence lifetime, τ_f , is 68 ns at room temperature [27]. Because the $\text{Ce}^{3+}:\text{YAG}$ has a quantum yield very close to unity at room temperature [29], the radiative lifetime τ_r can be assumed to be equal to the fluorescence lifetime. The 3-dB bandwidth of the fluorescence is typically around 100 nm.

The emission cross section spectrum, σ_e , as a function of wavelength λ can be derived from the bulk fluorescence spectrum $I(\lambda)$ with the Füchtbauer–Ladenburg equation (sometimes referred to as the McCumber method) [30], [31]:

$$\sigma_e(\lambda) = \frac{\lambda^5 I(\lambda)}{8\pi n^2 c \tau_r \int I(\lambda) \lambda d\lambda} \quad (2.1)$$

where n is the refractive index and c is the speed of light in vacuum. Note that the λ in the integration in the denominator was often mistakenly omitted in many literatures. Assume the shape of the line shape function, $\hat{g}(\nu)$, is Gaussian in the frequency domain, then the shape of $\sigma_e(\lambda)$ in the wavelength domain can be expressed as [32]:

$$\sigma_e(\lambda) = \frac{c^2}{8\pi n^2 \nu^2 \tau_r} \hat{g}(\nu) \propto \lambda^2 \exp\left(-\left(\frac{\lambda - \lambda_0}{K\lambda}\right)^2\right) \quad (2.2)$$

where λ_0 is the peak wavelength of \hat{g} and K is a bandwidth-related factor. This spectrum has a long tail in the long-wavelength side and does not appear as Gaussian due to the non-linear conversion between wavelength domain and frequency domain. Then the shape of the bulk fluorescence spectrum in the wavelength domain can be calculate from (2.1) and (2.2):

$$I(\lambda) \propto \lambda^{-3} \exp\left[-\left(\frac{\lambda - \lambda_0}{K\lambda}\right)^2\right] \quad (2.3)$$

This equation indicates a blue shift of the fluorescence spectrum with respect to the $\sigma_e(\lambda)$. The physical origin behind this blue shift is the higher emission probability for short wavelength photons due to higher optical mode density.

The Ce^{3+} :YAG fluorescence can be fitted by a combination of two fluorescence line shape functions in (2.3) with different weighting, λ_0 , and K values. The fitted result shows λ_0 are 522.6 nm and 570.7 nm for each line shape function. We then used the fitted curve to calculate the spectrum of σ_e with the Füchtbauer–Ladenburg equation in (2.1). The radiative lifetime and the refractive index used in the calculation are 68 ns and 1.835, respectively. The fitted fluorescence spectrum and the calculated spectrum of σ_e are also shown in Fig. 2.3. The calculated σ_e has a peak value of $48 \times 10^{-19} \text{ cm}^2$ at the wavelength of 573 nm.

The excited state absorption (ESA) takes place between the lowest 5d band and the

conduction band. The spectrum of signal ESA cross section σ_{esa}^s subtracted by the emission cross section σ_e is shown in Fig. 2.4. The spectrum shown in Fig. 2.4 is peaked at 700 nm and has positive values over the entire fluorescence wavelength range, thus impede the possibility of laser operation with the Ce³⁺:YAG crystal. By adding $\sigma_e(\lambda)$ to this spectrum, the value of σ_{esa}^s at 573 nm is estimated to be $71.6 \times 10^{-19} \text{ cm}^2$. The position of the lowest 5d band is about 10000 cm^{-1} lower than the edge of the conduction band, thus the ESA spectrum can extend to 1 μm at the long wavelength side. About 40% of the electrons excited to the conduction band transfer back to the lowest 5d state again, and the other 60% decay to the ground state non-radiatively. The overall lifetime of the electrons excited to the conduction band is 10 μs . Simple calculation from the above values gives that the lifetimes are 25 μs and 16.7 μs for relaxations to the lowest 5d band and the ground state, respectively.

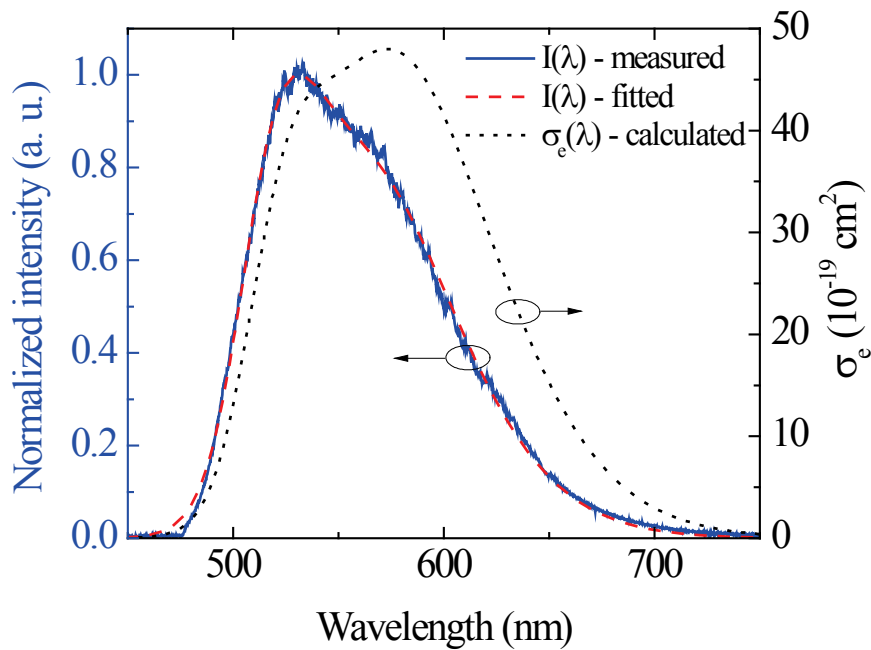


Fig. 2.3. Ce³⁺:YAG fluorescence spectrum at room temperature. Solid line: measured fluorescence line shape. Dashed line: fitted fluorescence line shape. Dotted line: calculated emission cross section.

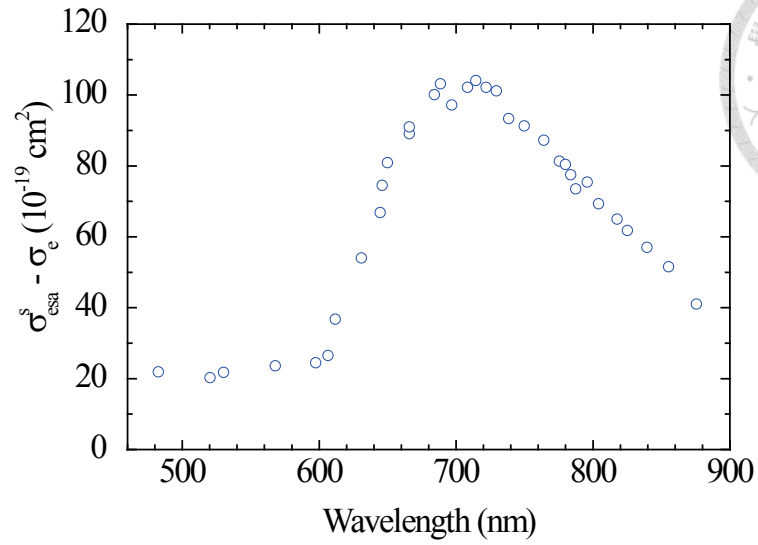


Fig. 2.4. The net signal cross section of $\text{Ce}^{3+}:\text{YAG}$ [27].

2.1.2 Rate Equations of $\text{Ce}^{3+}:\text{YAG}$

To formulate the rate equations of $\text{Ce}^{3+}:\text{YAG}$, we simplify the energy diagram to Fig. 2.5. The ground state is the $^2F_{5/2}$ level and the excited metastable state is the lowest 5d band. Due to the existence of the usually unoccupied $^2F_{7/2}$ level, the system can be represented as a 4-level system. The small overlap between the ground-state absorption spectrum and the emission spectrum also support this assumption. The pump and signal ESA transitions to the conduction band and the non-radiative relaxations from the conduction band are also included in this model.

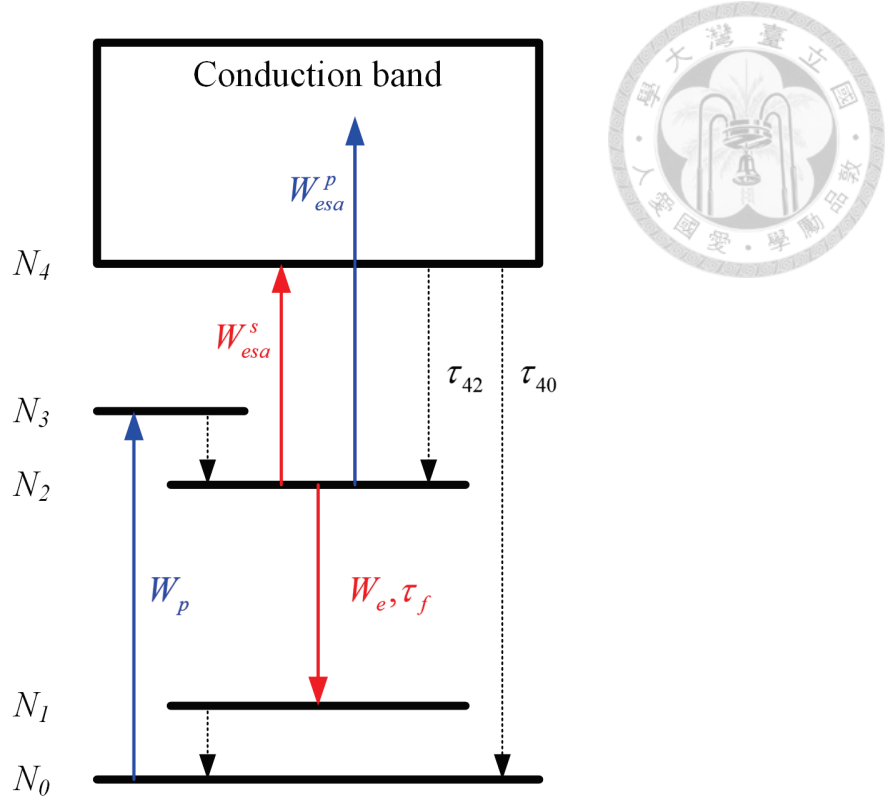


Fig. 2.5. Simplified energy diagram of $\text{Ce}^{3+}:\text{YAG}$. Solid arrows: absorptive or emissive transitions. Dotted arrows: non-radiative relaxations.

In a 4-level system, the terminating levels for both absorption and stimulated emission are rapidly depopulated to fast non-radiative relaxations:

$$N_1 \approx N_3 \approx 0 \quad (2.4)$$

So we have

$$N_T \approx N_0 + N_2 + N_4 \quad (2.5)$$

Where N_T is the doping concentration of Ce^{3+} ions, and N_0 to N_4 are the populations at the levels shown in Fig. 2.5. The rate equations can be written as:

$$\frac{dN_0}{dt} = -N_0 W_p + N_2 W_e + \frac{N_2}{\tau_f} + \frac{N_4}{\tau_{40}} \quad (2.6)$$

$$\frac{dN_2}{dt} = N_0 W_p - N_2 W_e - \frac{N_2}{\tau_f} - N_2 (W_{esa}^p + W_{esa}^s) + \frac{N_4}{\tau_{42}} \quad (2.7)$$

$$\frac{dN_4}{dt} = N_2 (W_{esa}^p + W_{esa}^s) - \frac{N_4}{\tau_{40}} - \frac{N_4}{\tau_{42}} \quad (2.8)$$

where τ_f is the fluorescence lifetime, τ_{40} is the lifetime of the transition between the conduction band and ground state, and τ_{42} is the lifetime of the transition between the conduction band and the excited state. W_p , W_e , W_{esa}^p , and W_{esa}^s are the transition probabilities of the ground state absorption, the stimulated emission, pump ESA, and signal ESA, respectively. These probabilities are expressed as following:

$$W_p = \frac{\sigma_a I_p \lambda_p}{hc} \quad (2.9)$$

$$W_e = \frac{\sigma_e I_s \lambda_s}{hc} \quad (2.10)$$

$$W_{esa}^p = \frac{\sigma_{esa}^p I_p \lambda_p}{hc} \quad (2.11)$$

$$W_{esa}^s = \frac{\sigma_{esa}^s I_s \lambda_s}{hc} \quad (2.12)$$

where σ_a is the GSA cross section at the pump wavelength λ_p , σ_e is the stimulated emission cross section at the signal wavelength λ_s , σ_{esa}^p is the ESA cross section at pump wavelength, σ_{esa}^s is the ESA cross section at signal wavelength, I_p is the pump intensity, I_s is the signal (or fluorescence) intensity, c is the speed of light in vacuum, and h is Planck's constant.

The populations and the optical intensity reach a steady state in continuous wave applications. By letting the equations (2.6) to (2.8) equal to zero, the steady-state solutions are found to be:

$$N_2 = N_T \frac{W_p \tau_f}{1 + W_p \tau_f + W_e \tau_f + W_{ESA} \tau_f \tau_4 (W_p + \tau_{40}^{-1})} \quad (2.13)$$

$$N_0 = N_T - N_2 (1 + W_{ESA} \tau_4) \quad (2.14)$$

$$N_4 = N_2 W_{ESA} \tau_4 \quad (2.15)$$

The parameters of Ce³⁺:YAG are summarized in the following table. All the cross section values and the lifetime values are directly cited or calculated based on the data

from [27]. The pump wavelength is chosen to be 446 nm used in the experiments. The signal wavelength is chosen to be the peak wavelength of the emission cross section spectrum, which is 573 nm. The pump ESA cross section at the pump wavelength of 446 nm was extrapolated from the spectrum in Fig. 2.4 to be $20 \times 10^{-19} \text{ cm}^2$.

Table 2.1. Summary of optical parameters of $\text{Ce}^{3+}:\text{YAG}$

Parameters	Symbol	Value
Refractive index (at 446 nm)	n	1.850
Refractive index (at 573 nm)	n	1.834
Absorption cross section (at 446 nm)	σ_a	$16.8 \times 10^{-19} \text{ cm}^2$
Emission cross section (at 573 nm)	σ_e	$48 \times 10^{-19} \text{ cm}^2$
Pump excited state absorption (at 446 nm)	σ_{esa}^p	$20 \times 10^{-19} \text{ cm}^2$
Signal excited state absorption (at 573 nm)	σ_{esa}^s	$71.6 \times 10^{-19} \text{ cm}^2$
Fluorescence lifetime (at 300 K)	τ_f	68 ns
Radiative lifetime (at 300 K)	τ_r	68 ns
Conduction band lifetime	τ_4	10 μs
Conduction band lifetime (to ground state)	τ_{40}	16.7 μs

2.2 Energy Diagram and Rate Equations of $\text{Cr}^{4+}:\text{YAG}$

2.2.1 Energy Diagram of $\text{Cr}^{4+}:\text{YAG}$

Chromium is a transition metal element with the electronic configuration of $[\text{Ar}]3d^54s^1$. When doped in the YAG crystal, most of the chromium ions are in the trivalent state. By co-doping with Ca^{2+} or Mg^{2+} ions for charge compensation, some of the chromium ions are in the tetravalent state. The crystal structure of YAG is shown in Fig. 2.6. The Cr^{3+} ions substitute the Al^{3+} ions in either the octahedron or the tetrahedron sites, whereas the Cr^{4+} ions only substitute the Al^{3+} ions in the tetrahedron sites. The broadband near-infrared fluorescence at 1.4 μm comes from the Cr^{4+} ions.

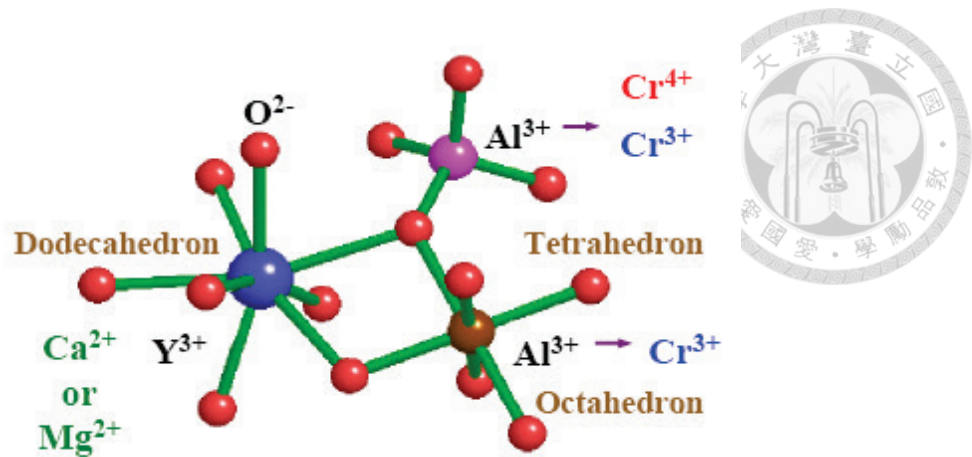


Fig. 2.6. Schematic of the Cr:YAG crystal structure

The electronic configuration of the Cr^{4+} ion is $[\text{Ar}]3d^2$ with two free electrons in the 3d orbitals outside the argon core. Since there is no shielding for the two 3d electrons, the Cr^{4+} ion is sensitive to the crystal field. The local symmetry of an ideal tetrahedron site is T_d with 3 S_4 symmetry axes. However, in the Cr^{4+} :YAG crystal the tetrahedron is elongated along a crystallographic axis, thus the local symmetry is lowered to D_{2d} symmetry with one S_4 symmetry axis [33].

The effect of crystal field on the splitting of the d-shell energy levels can be described by the Tanabe-Sugano diagram [34]. The Tanabe-Sugano diagram for tetrahedrally coordinated d_2 ions is shown in Fig. 2.7. In T_d symmetry, the 3F state is split by the crystal field into 3A_2 , 3T_2 and 3T_1 states. The normalized crystal field strength parameter (Dq/B) of YAG crystal is 1.78 [35], which is close to the cross point of 3T_2 state and the 1E state. Although the two states are close in energy level, it was confirmed by piezospectroscopic studies that the broadband NIR emission originates from 3T_2 state but not 1E state [36]. When the symmetry is lowered to D_{2d} , the 3A_2 state becomes 3B_1 , the 3T_2 state is split into 3B_2 and 3E states, and the 3T_1 state is split into 3A_2 and 3E states. The electron-phonon coupling broadens the spectra of transitions among these states. The energy diagram appeared in Fig. 2.8 depicts the level splitting in Cr^{4+} :YAG and indicates the energy of each level.

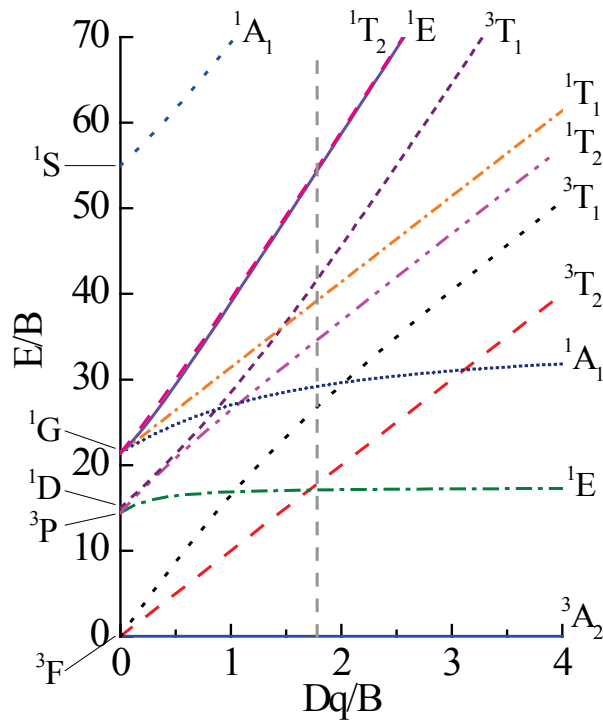


Fig. 2.7. The Tanabe-Sugano diagram for d_2 configuration in tetrahedral coordination [37]. The vertical dashed line indicates the crystal field strength of YAG crystal.

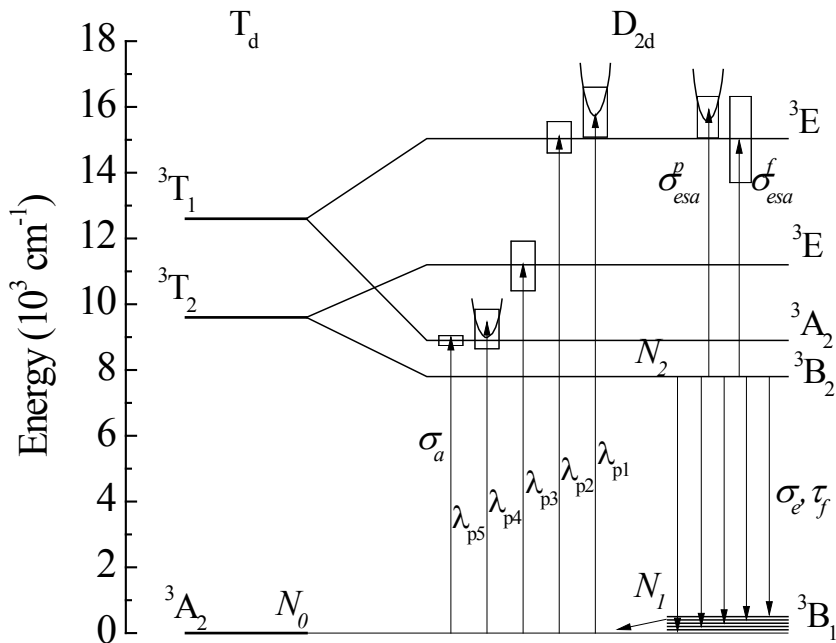


Fig. 2.8. Energy level diagram of the Cr^{4+} ions doped in YAG host. Center wavelength of the pump absorption: $\lambda_{p1}=609\text{ nm}$, $\lambda_{p2}=665\text{ nm}$, $\lambda_{p3}=893\text{ nm}$, $\lambda_{p4}=1034\text{ nm}$, $\lambda_{p5}=1124\text{ nm}$ [38].

The extensive Cr⁴⁺ ground state absorption spectrum shown in Fig. 2.9 actually combines several absorption bands centered at wavelengths indicated in Fig. 2.8. Excitation at 1064 nm induces transition from ³B₁(³A₂) to ³A₂(³T₁). The excited electrons quickly relax to ³B₂(³T₂), which is the metastable excited state for the broadband NIR emission. The Cr³⁺ centers in YAG have strong absorption at wavelengths shorter than 700 nm, which is also shown in Fig. 2.9. Therefore the most suitable pump wavelength region for Cr⁴⁺ centers in YAG is between 800 to 1200 nm.

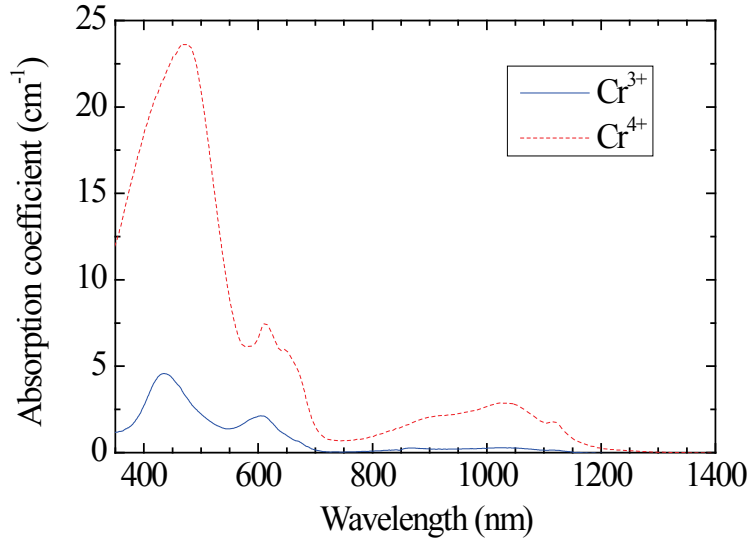


Fig. 2.9. Ground-state absorption spectra of Cr³⁺ and Cr⁴⁺ ions in YAG [39].

The electrons at the metastable state relaxed to the ground state radiatively or non-radiatively. The non-radiative lifetime τ_{nr} is strongly dependent on the temperature because the non-radiative transition can be enhanced by the electron-phonon coupling effect. The radiative lifetime τ_r is also dependent on but much less sensitive to the temperature, and can be assumed to be constant over a limited temperature range. The fluorescence lifetime, τ_f , can then be expressed as:

$$\frac{1}{\tau_f(T)} = \frac{1}{\tau_r} + \frac{1}{\tau_{nr}(T)} \quad (2.16)$$

where T is the crystal temperature. A linear fit of the fluorescence lifetime of some transition-metal-doped laser crystals in the temperature range from 0 to 100 °C has been found by Sennaroglu as [40]:

$$\tau_f(T) = \tau_f^0 - \tau_f^T(T - T_0) \quad (2.17)$$

where τ_f^0 is the fluorescence lifetime at the temperature T_0 and τ_f^T is a constant with a value of $0.0416 \mu\text{s}/^\circ\text{C}$ for $\text{Cr}^{4+}:\text{YAG}$. The τ_f of our $\text{Cr}^{4+}:\text{YAG}$ crystal fiber was measured to be $4.2 \mu\text{s}$ [41] at $T = 300 \text{ K}$. By calculating $\tau_f(T)$ calculated with (2.17), we can see a large decrease of lifetime from 5.3 to $1.1 \mu\text{s}$ from 0 to 100°C , as shown in Fig. 2.10.

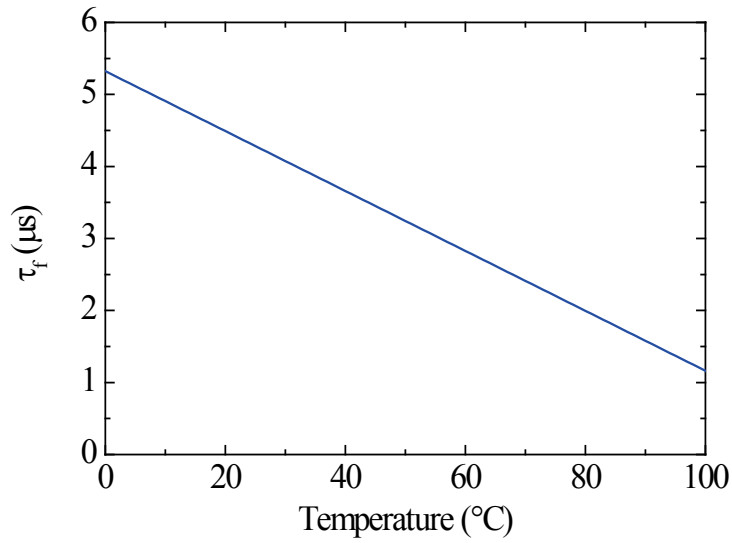


Fig. 2.10. Fluorescence lifetime of the $\text{Cr}^{4+}:\text{YAG}$ crystal.

The quantum yield is defined as the ratio of the number of emitted photons to the number of absorbed photons, which is equal to:

$$\eta_{QY}(T) = \tau_f(T) / \tau_r \quad (2.18)$$

Since the η_{QY} of $\text{Cr}^{4+}:\text{YAG}$ was fitted to be 22% at the temperature of 300 K [42], we can get a τ_r of $19.1 \mu\text{s}$ and a τ_{nr} of $5.38 \mu\text{s}$ at 300 K.

The measured $\text{Cr}^{4+}:\text{YAG}$ emission spectrum of bulk crystal is shown in Fig. 2.11. The broadband fluorescence spans from 1100 to 1700 nm and peaks at 1380 nm. The dips near the vicinity of the peak is due to water vapor absorption in the air path. The emission cross section spectrum of $\text{Cr}^{4+}:\text{YAG}$ can be found with the same method used in the previous section. Although the fluorescence of $\text{Cr}^{4+}:\text{YAG}$ belongs to an ensemble of transitions, its spectrum can be well fitted by a single fluorescence line shape function of

(2.3). The Füchtbauer–Ladenburg equation in (2.1) was then used to find the spectral shape of σ_e . These spectra are plotted in Fig. 2.11 as well. The σ_e has a peak value of $2.67 \times 10^{-19} \text{ cm}^2$ at 1431 nm and a 3-dB bandwidth of 304 nm, covering from 1291 to 1605 nm.

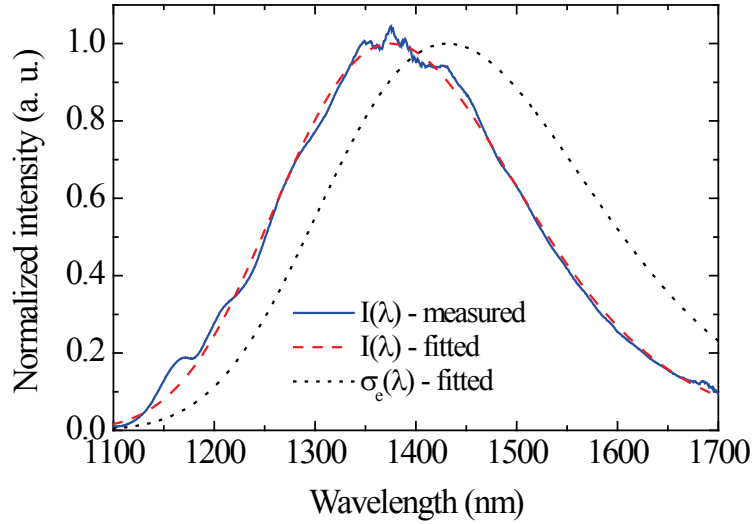


Fig. 2.11. Cr^{4+} :YAG emission spectra. Solid line: measured fluorescence line shape. Dashed line: fitted fluorescence line shape. Dotted line: calculated emission cross section spectrum.

ESAs at both pump and signal wavelengths excite electrons from ${}^3\text{B}_2({}^3\text{T}_2)$ to ${}^3\text{E}({}^3\text{T}_1)$. These electrons will then non-radiatively relax back to ${}^3\text{B}_2({}^3\text{T}_2)$ with a very short lifetime less than 100 ns [43], [44], thus the influence of ESA on the excited state population can be neglected in CW applications. There is no explicitly presented spectrum of the signal ESA cross section, σ_{esa}^s , or the pump ESA cross section, σ_{esa}^p , in the literature. Instead, two ratios were used to define the magnitude of ESA:

$$f_L \equiv \frac{\sigma_{esa}^s}{\sigma_e} \quad (2.19)$$

$$f_p \equiv \frac{\sigma_{esa}^p}{\sigma_a} \quad (2.20)$$

These ratios are actually functions of wavelength. However, due to the lack of knowledge on the details in the spectral shape of signal ESA, a constant value of f_L was

used. The value of f_p was given at the wavelengths of 1060, 946, and 914 nm as 0.19, 0.27, and 0.36, respectively [45]. Therefore, the 1060-nm pump is more preferred than the other two wavelengths because of the minor pump ESA.

The optical transitions exhibits strong polarization dependence for Cr⁴⁺:YAG. When the pump beam is polarized along the S₄ axis, the ground-state absorption cross section is 20 times higher than that with the pump beam polarized orthogonal to the S₄ axis [46]. Similarly, the emission cross section is higher for the signal beam polarized along the S₄ axis [17], [46].

Despite the relatively simple local symmetry of the Cr⁴⁺ ions, the overall polarization dependence of the Cr⁴⁺:YAG crystal is more complicated. There are three groups of Cr⁴⁺ ions in a Cr⁴⁺:YAG crystal, each with the S₄ axis parallel to a <0 0 1> crystal axis. As a result, the Cr⁴⁺:YAG lasers have best performance when the polarizations of both the pump and the signal are parallel to the same crystal axis. Since there is no intrinsic birefringence in the YAG crystal, any stress-induced birefringence can rotate the laser polarization away from the crystal axes and induced the depolarization loss [47].

In this dissertation, we only consider the situation with pump beam polarized along a crystallographic axis of the Cr⁴⁺:YAG crystal. Furthermore, we assume that the pump beam only excites the Cr⁴⁺ sites with the S₄ axis parallel to the pump polarization. The excitation of the other two groups of Cr⁴⁺ sites can be reasonably ignored due to the much smaller GSA cross section when the pump polarization and the S₄ axes are orthogonal, as previously mentioned.

2.2.2 Rate Equations of Cr⁴⁺:YAG

To summarize, Cr⁴⁺:YAG is a 4-level laser material with additional pump and signal ESAs. The simplified energy diagram is shown in Fig. 2.12. The energy levels which can interact with the pump or the fluorescence are numbered as level 0 to 5. Since we only assume one group of the sites are excited, and the three groups of sites are identical, then the concentration of the site should be:

$$N_T = \frac{N_D}{3} \quad (2.21)$$

where N_D is the doping concentration of the Cr⁴⁺ ions, and N_T is the total

concentration of the group of Cr^{4+} ions which can be selectively excited with the linear polarized pump. Since the lifetimes of levels 3, 4, and 5 are very short compared with the fluorescence lifetime, τ_f , we have:

$$N_1 \approx N_3 \approx N_5 \approx 0 \quad (2.22)$$

Thus we can assume:

$$N_T = N_g + N_2 \quad (2.23)$$

where N_g is the ground state population and N_2 is the excited state population.

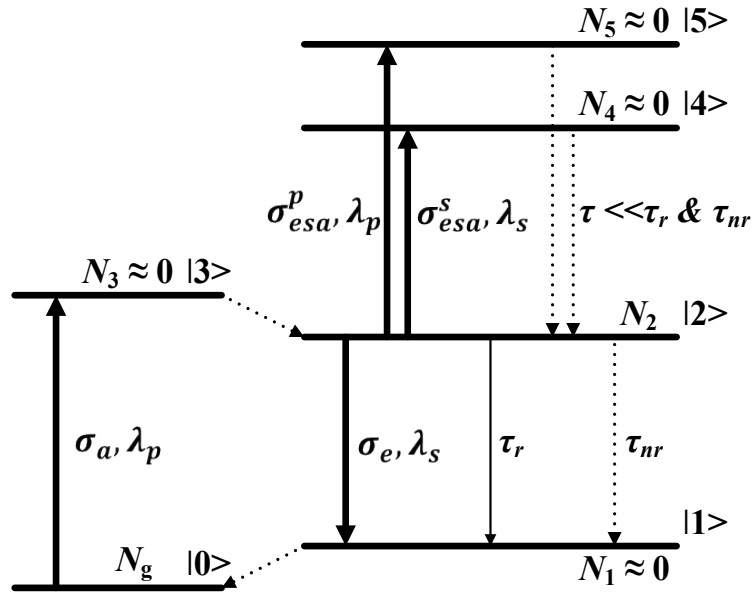


Fig. 2.12. Simplified Cr^{4+} :YAG energy diagram. Solid arrows: radiative transitions. Dotted arrows: non-radiative transitions.

The rate equation describing the temporal change of the excited state population can then be written as:

$$\frac{dN_2}{dt} = N_g R_{03} - N_2 W_{21} - \frac{N_2}{\tau_f} \quad (2.24)$$

where R_{03} is the transition probability of the ground state absorption, and W_{21} is the transition probability of the stimulated emission. These parameters are defined as:

$$R_{03} = \frac{I_p \sigma_a \lambda_p}{hc} \quad (2.25)$$

$$W_{21} = \sum_N \frac{I_s(\lambda_i) \sigma_e(\lambda_i) \lambda_i}{hc} \quad (2.26)$$

where I_p is the pump intensity at the pump wavelength λ_p , and $I_s(\lambda_i)$ is the signal intensity in the i th wavelength slot centered at λ_i . The signal intensity was divided into N slots to take into account different wavelengths in the broad emission spectrum.

Finally, by equating (2.24) to zero, the steady-state equation is derived as:

$$N_2(z) = N_T \frac{R_{03}(z)}{R_{03}(z) + W_{21}(z) + 1/\tau_f} \quad (2.27)$$

The optical parameters of Cr^{4+} :YAG are summarized in Table 2.2.

Table 2.2. Summary of optical parameters of Cr^{4+} :YAG

Parameters	Symbol	Value
Refractive index (at 1431 nm)	n	1.809
Absorption cross section (at 1064 nm)	σ_a	$22 \times 10^{-19} \text{ cm}^2$
Emission cross section (at 1431 nm)	σ_e	$2.67 \times 10^{-19} \text{ cm}^2$
Pump excited state absorption (at 1064 nm)	σ_{esa}^p	$5.1 \times 10^{-19} \text{ cm}^2$
Signal excited state absorption (at 1431 nm)	σ_{esa}^s	$1.28 \times 10^{-19} \text{ cm}^2$
Fluorescence lifetime (at 300 K)	τ_f	4.2 μs
Radiative lifetime (at 300 K)	τ_r	19.1 μs
Non-radiative lifetime (at 300 K)	τ_{nr}	5.38 μs
Thermal lifetime coefficient (0 to 100 °C)	τ_{fT}	0.0416 $\mu\text{s}/^\circ\text{C}$

2.3 Power Evolution Equations of Broadband Light Propagating in Crystal Fibers

The power evolution equations describe the evolution of pump and signal powers along the crystal fiber. Although the energy diagram and polarization properties are quite different for Ce^{3+} :YAG and Cr^{4+} :YAG crystals, they share the same power evolution equations since both crystals are 4-level systems with additional pump and signal ESAs.

2.3.1 Broadband Spontaneous Emission in Crystal Fibers

Before discussing the power evolution equations in crystal fibers, it is helpful to derive the equations of the spontaneous emission intensity emitted from an active ion and captured by a crystal fiber. The spectral density of the spontaneous emission intensity in the frequency range from ν to $\nu + d\nu$ per one polarization can be expressed as [48]:

$$S_{sp}(\nu)d\nu = h\nu \frac{c}{n} \sigma_e(\nu) M(\nu) d\nu \quad (2.28)$$

where $S_{sp}(\nu)$ is the spectral power density of the spontaneous emission, and $M(\nu)$ is the density of the optical modes. In a three dimensional resonator, such as a bulk crystal, the optical mode density is expressed as:

$$M_{3D}(\nu) = \frac{8\pi n^3 \nu^2}{c^3} \quad (2.29)$$

While in a one dimensional resonator, such as a single mode optical fiber, the mode density becomes:

$$M_{1D}(\nu) = \frac{2n}{c} \cdot \frac{1}{A_{1D}} \quad (2.30)$$

The term A_{1D} is the cross sectional area of the 1D resonator.

Our crystal fibers are mostly highly multimode fibers. The geometry of highly multimode fiber is similar to a 3D resonator with limited acceptance angle. Equation (2.28) describes the optical power emitted into whole 4π solid angle. In an optical fiber the spontaneous emission can only be captured within the solid angle (considering only forward direction):

$$\Omega = 2\pi \left(1 - \frac{n_{clad}}{n_{core}} \right) \quad (2.31)$$

We can rewrite Eq. (2.28) in the wavelength domain with the use of (2.29):

$$S_{sp}(\lambda) = \frac{4\pi n_{core} (n_{core} - n_{clad}) hc^2}{\lambda^5} \sigma_e(\lambda) \quad (2.32)$$

This is the spectral density of spontaneous emission intensity per active ion per

polarization per direction in a highly multimode fiber. The fifth order dependence on the wavelength in the denominator is consistent with that in (2.1).

For single-mode or few-mode crystal fibers, such as those clad with high-index glass or ceramics, are similar to a 1D resonator. We can then rewrite (2.28) with (2.30) in the wavelength domain, and divide it by 2 for considering only forward direction:

$$S_{sp}(\lambda) = \frac{M(\lambda)hc^2}{\lambda^3 A_{core}} \sigma_e(\lambda) \quad (2.33)$$

This is the spectral density of spontaneous emission intensity per active ion per polarization per direction in a single-mode or few-mode fiber. A_{core} is the cross sectional area of core. $M(\lambda)$ is the number of transverse modes in the crystal fiber at wavelength λ . Although this equation was derived for few-mode fibers, it can also be extended to highly-multimode fibers. For highly-multimode fibers the transverse mode numbers can be approximated as [49]:

$$M(\lambda) \approx \frac{2\pi A_{core}}{\lambda^2} (n_{core}^2 - n_{clad}^2) \quad (2.34)$$

By substituting (2.34) into (2.33) we can get:

$$S_{sp}(\lambda) = \frac{4\pi n_{core} (n_{core} - n_{clad}) hc^2}{\lambda^5} \sigma_e(\lambda) \cdot \frac{n_{core} + n_{clad}}{2n_{core}} \quad (2.35)$$

The result is close to (2.32). In this dissertation, we choose (2.32) to treat highly multimode crystal fibers instead of (2.35) which depends on more approximations.

2.3.2 Power Evolution Equations in Crystal Fibers

The pump light propagate in the Ce^{3+} :YAG crystal fiber encounters GSA, ESA and the propagation loss. The equation describing the evolution of the pump power P_p in the crystal fiber at the axial position z is:

$$\pm \frac{dP_p^\pm(z)}{dz} = - \left[\Gamma_p (N_g(z) \sigma_a + N_2(z) \sigma_{esa}^p) + \alpha_{pl}^p \right] P_p^\pm(z) \quad (2.36)$$

where Γ_p is the pump confinement factor and α_{pl}^p is the propagation loss at the pump wavelength. The \pm sign indicates two different propagation directions, i. e., forward and

backward directions.

For the signal light (light within the emission wavelength bands, including the fluorescence), there is no GSA since $\text{Ce}^{3+}:\text{YAG}$ and $\text{Cr}^{4+}:\text{YAG}$ are both 4-level systems. Therefore, it will only encounter the ESA, the amplification by the stimulated emission, and the propagation loss. The spontaneous emission also contribute to the signal power. To accurately evaluate the broadband signal light at different wavelengths, the signal spectrum are divided into multiple slots in the wavelength domain. The equation describing the evolution of the signal power P_s in the i_{th} wavelength slot at the axial position z is then:

$$\pm \frac{dP_s^\pm(\lambda_i, z)}{dz} = \left\{ N_2(z) \Gamma_s \left[\sigma_e(\lambda_i) - \sigma_{esa}^s(\lambda_i) \right] - \alpha_{pl}^s \right\} P_s^\pm(\lambda_i, z) + 2N_2(z) A_{core} S_{sp}(\lambda_i) \Delta\lambda_i \quad (2.37)$$

where $\Delta\lambda_i$ is the width of the i_{th} wavelength slot centered at λ_i , and Γ_s is the signal confinement factor. The term $S_{sp}(\lambda_i)$ is the spectral power density of spontaneous emission per active ion per polarization per direction, as given by (2.32) for multimode crystal fibers and (2.33) for single-mode and few-mode crystal fibers. The factor of 2 before the spontaneous emission term is for taking into account the two polarization states. If only one polarization is considered, this factor should be dropped.

2.4 Conversion Efficiency and Brightness of Broadband Light Sources

For highly-doped $\text{Ce}^{3+}:\text{YAG}$ crystal fiber, the pump beam can be totally absorbed within less than 2 centimeters. In this case, the propagation loss or the ESA effect can be neglected. Besides, the $\text{Ce}^{3+}:\text{YAG}$ crystal is unlikely to be saturated by the pump due to the very short lifetime, so the population inversion remains almost constant along the whole crystal fiber. Therefore, there is no need to perform the propagation analysis in the previous section. Instead, a simpler model can be used to directly compute the conversion efficiency of the crystal fiber.

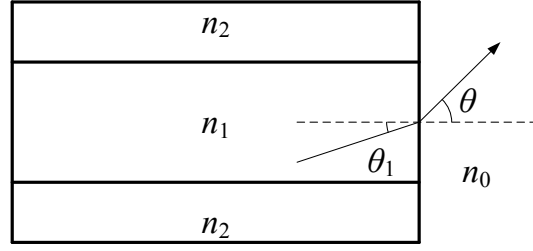


Fig. 2.13. A schematic drawing of the crystal fiber broadband light source.

A schematic drawing of the crystal fiber broadband light source is shown in Fig. 2.13. The refractive indices for the surrounding medium, crystal fiber core and the crystal fiber clad are n_0 , n_1 , and n_2 , respectively. For Pyrex-clad Ce^{3+} :YAG crystal fibers, the core and clad indices are 1.835 and 1.47, respectively. The numerical aperture of the crystal fiber is:

$$NA_f = \sqrt{n_1^2 - n_2^2} \quad (2.38)$$

The angle between the ray and the fiber axis is defined as θ_1 . The critical angle of the crystal fiber is:

$$\theta_c = \cos^{-1}(n_2/n_1) \quad (2.39)$$

The ray can be guided in the crystal fiber core only if $\theta_1 \leq \theta_c$. After the rays emerge the crystal fiber end face, the rays are refracted with a new angle θ with respect to the fiber axis:

$$\theta = \sin^{-1} \frac{n_1 \sin \theta_1}{n_0} \quad (2.40)$$

And after the refraction the critical angle becomes:

$$\theta'_c = \sin^{-1} \left(\frac{\sqrt{n_1^2 - n_2^2}}{n_0} \right) = \sin^{-1} \frac{NA_f}{n_0} \quad (2.41)$$

If the NA of the crystal fiber is larger than n_0 , the θ'_c will be clamped at $\pi/2$. Rays beyond that angle will be reflected back into the crystal fiber through total internal reflection (TIR) at the crystal fiber end. For the Pyrex-clad Ce^{3+} :YAG crystal fiber, the critical angle is 36.7° and 90° for θ_c and θ'_c , respectively. Because the critical angle is large, it is important to consider the reflectance of the fiber end face since it grows as θ



increases. The TE reflectance R_{TE} and the TM reflectance R_{TM} are expressed as functions of θ :

$$R_{TE}(\theta) = \left| \frac{\cos\theta - n_1/n_0 \cdot \sqrt{1 - (n_0/n_1)^2 \sin^2\theta}}{\cos\theta + n_1/n_0 \cdot \sqrt{1 - (n_0/n_1)^2 \sin^2\theta}} \right|^2 \quad (2.42)$$

$$R_{TM}(\theta) = \left| \frac{\cos\theta - n_0/n_1 \cdot \sqrt{1 - (n_0/n_1)^2 \sin^2\theta}}{\cos\theta + n_0/n_1 \cdot \sqrt{1 - (n_1/n_0)^2 \sin^2\theta}} \right|^2 \quad (2.43)$$

These reflectance can also be expressed as functions of θ_1 by substituting θ with θ_1 and exchanging n_0 and n_1 in the equations. The curves of reflectance versus θ_1 of Pyrex-clad Ce^{3+} :YAG crystal fibers are plotted in Fig. 2.14. Some of the guided rays that propagate with angles beyond the TIR angle of the end face are trapped inside the crystal fiber, until they are finally transferred into radiation modes through surface or bulk scattering processes.

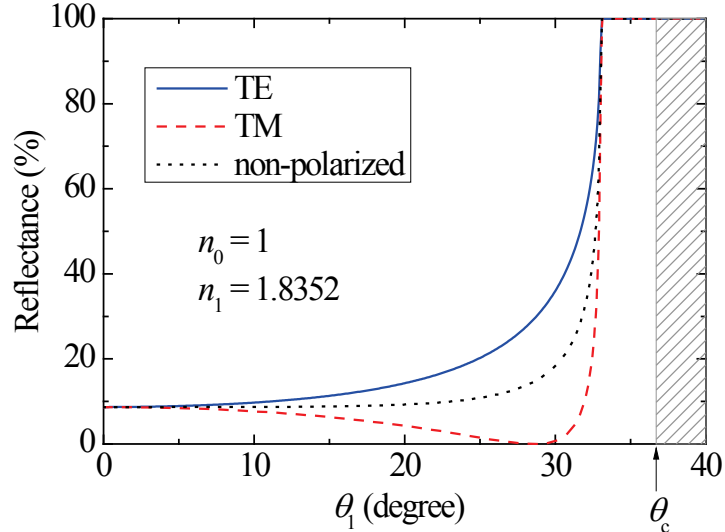


Fig. 2.14. Reflectance at the crystal fiber end face for different polarization states. The rays propagates with angles in the shaded region are unguided by the crystal fiber.

Because the Ce^{3+} :YAG fluorescence is unpolarized, we can calculate the unpolarized transmittance to be:

$$T(\theta) = 1 - \frac{R_{TE}(\theta) + R_{TM}(\theta)}{2} \quad (2.44)$$

Now we are going to compute the angular distribution of the crystal fiber broadband light source. Assume a bunch of fluorescence photons with a total power of P_1 are emitted somewhere inside the crystal fiber core and spread uniformly into the whole 4π solid angle, then the radiance intensity I_1 in the crystal fiber core is:

$$I_1 = \frac{dP_1}{d\Omega} = \frac{P_1}{4\pi} \quad (2.45)$$

The unit of radiance intensity is $\text{W}\cdot\text{sr}^{-1}$. Considering that the integration of the radiance intensity over a specific solid angle conserves after refraction (except the Fresnel loss), we can work out the radiance intensity distribution output from the crystal fiber end face into the surrounding medium:

$$I_0(\theta) = I_1 \frac{n_0^2}{n_1} \frac{\cos\theta}{\sqrt{n_1^2 - n_0^2 \sin^2\theta}} T(\theta) \quad (2.46)$$

This distribution can be integrated over the solid angle to get the total power:

$$P_0 = 2\pi \int_0^{\theta'_c} I_0(\theta) \sin\theta d\theta \quad (2.47)$$

where θ'_c is defined in (2.41). If a lens is used to collect the total power, the upper limit of the integration can be changed to the acceptance angle of the lens:

$$\theta_c'' = \sin^{-1} \frac{NA_L}{n_0} \quad (2.48)$$

where NA_L is the numerical aperture of the lens.

The optical to optical conversion efficiency is expressed as following:

$$\eta = T_{Lp} T_{Ls} T_p \eta_{QE} \eta_{QY} \frac{P_0}{P_1} \quad (2.49)$$

where T_{Lp} and T_{Ls} are the transmittance of the lenses used for pump coupling and fluorescence collection, if any. T_p is the pump transmittance at the surrounding medium into the crystal fiber core. This quantity can be derived with procedure above if the

radiance intensity distribution of the pump source is known, or one can use the transmittance under normal incidence if the pump is not too tightly focused. η_{QE} is quantum efficiency, which is defined as the ratio of signal photon energy to the pump photon energy. η_{QY} is the quantum yield defined as the ratio of the radiative transition rate to the total transition rate. The quantum efficiency and the quantum yield for the $\text{Ce}^{3+}:\text{YAG}$ crystal are 0.796 and 1, respectively, with the pump wavelength of 446 nm and the peak fluorescence wavelength of 560 nm.

For example, considering a broadband light source based on a Pyrex-clad $\text{Ce}^{3+}:\text{YAG}$ crystal fiber pumped with a 446-nm laser. The pump was assumed to be moderately focused, thus normal incidence transmittance of 91.1% was used for T_p . The transmittance of the pump focusing lens and the signal collection lens are both assumed to be 98%. The calculated radiance intensity distribution $I_0(\theta)$ is shown in Fig. 2.15. With the use of equations (2.47), (2.48), and (2.49), we can get the curve of optical to optical conversion efficiency versus the numerical aperture of the collection lens, as shown in Fig. 2.16.

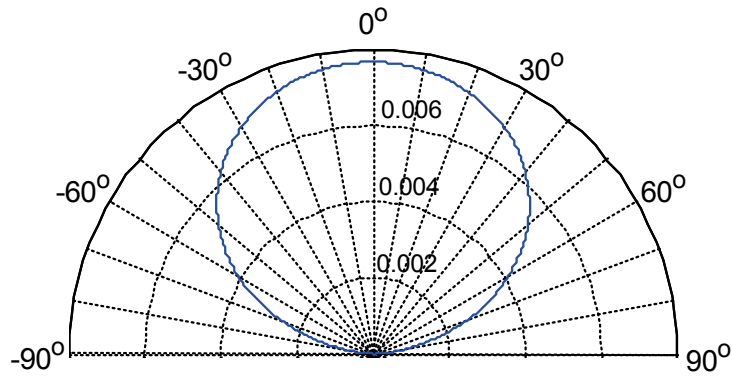


Fig. 2.15. Radiance intensity distribution of $\text{Ce}^{3+}:\text{YAG}$ crystal fiber.

Unit: W sr^{-1} .

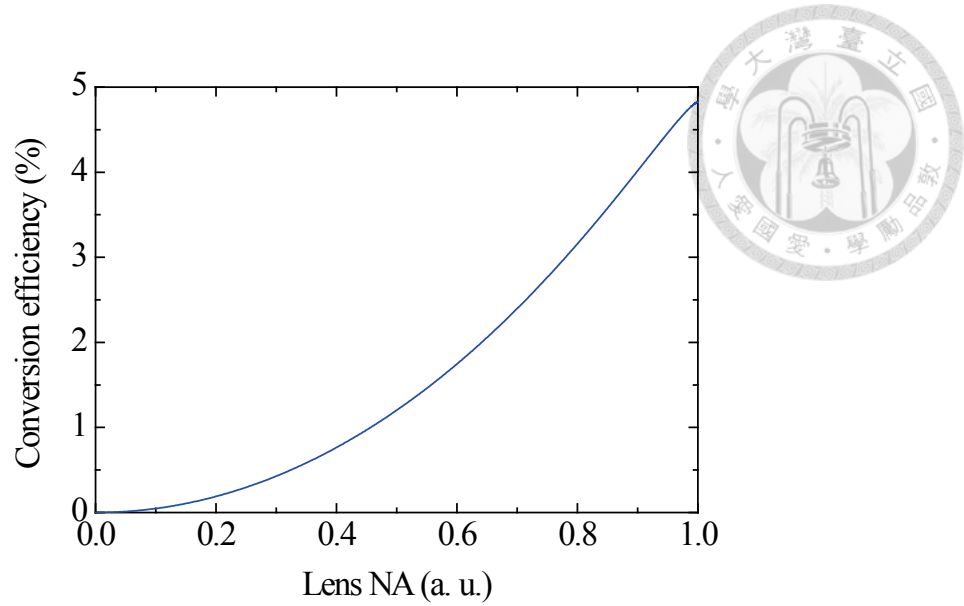


Fig. 2.16. The conversion efficiency of Ce^{3+} :YAG crystal fiber broadband light source versus the numerical aperture of the collection lens.

The brightness of a light source is a measure of the quantity of radiation emitted from a surface and falls within a given solid angle in a specified direction. The brightness is also called “radiance” and the SI unit $\text{W mm}^{-2} \text{sr}^{-1}$. It is denoted by L and is defined as following:

$$L = \frac{d^2P}{dA d\Omega \cos \theta} = \frac{I_0(\theta)}{A \cos \theta} \quad (2.50)$$

where A is the area of the emitter, which is the area of the crystal fiber core in our case. The brightness is usually a function of θ , except for a Lambertian source whose $I_0(\theta)$ is proportional to $\cos \theta$.

Following the previous example, if we assume that the crystal fiber has a core diameter of $25 \mu\text{m}$ and the input pump power is 500 mW , then we can calculate the radiance distribution of the Ce^{3+} :YAG light source, as shown in Fig. 2.17. The radiance has a peak value of $16.8 \text{ W mm}^{-2} \text{sr}^{-1}$ at the exit angle of $\pm 53^\circ$ and an on-axis value of $15.6 \text{ W mm}^{-2} \text{sr}^{-1}$.

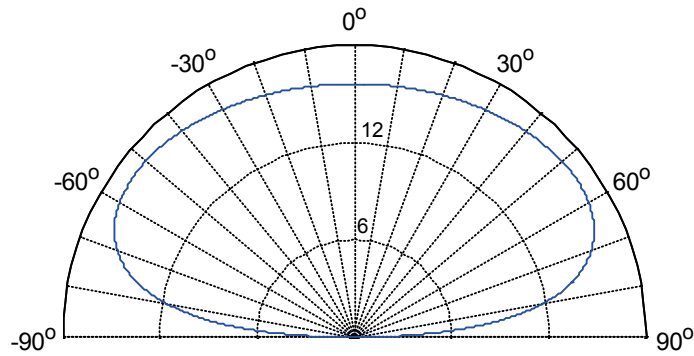


Fig. 2.17. Radiance distribution of the Ce^{3+} :YAG crystal fiber broadband light source. The radial unit is $\text{W mm}^{-2} \text{sr}^{-1}$. The shape is different from radiance intensity distribution in Fig. 2.15 due to the $\cos\theta$ term in Eq. (2.50).

2.5 Modeling of Crystal Fiber Lasers and Amplifiers

Theoretical modeling of lasers are required for the optimization of laser performance or the extraction of the material parameters by fitting the experimental results. For bulk Cr^{4+} :YAG lasers, a lumped model was used for the parameter extraction [16]. The lumped model was also applied to the Cr^{4+} :YAG crystal fiber laser [50]. However, the lumped model is not suitable for crystal fibers, because the optical power and the electron population may vary significantly along the crystal fiber. In this section, we discuss a distributed model which can model the crystal fiber laser more accurately.

2.5.1 The Lumped Model for Cr^{4+} :YAG Crystal Fiber Laser

In the lumped model, every parameters are assumed to constant along the crystal fiber and only dependent on time. There are two main equations in the lumped model, one is the rate equations of the population inversion in (2.24), which is repeated here for convenience:

$$\frac{dN_2}{dt} = N_g R_{03} - N_2 W_{21} - \frac{N_2}{\tau_f} \quad (2.51)$$

And the other is the rate equation of the intra-cavity signal power [50]:

$$\frac{dP_s(t)}{dt} = P_s(t) \left[\frac{c}{n} (\sigma_e - \sigma_{esa}^s) N_2(t) - \frac{1}{t_c} \right] \quad (2.52)$$



where t_c is the cavity photon lifetime defined as:

$$t_c = \frac{c \left[1 - R_1^s R_2^s \exp(-2\alpha_{pl}^s L) \right]}{2n_1 L} \quad (2.53)$$

in which R_1^s and R_2^s are the signal reflectance at the input and output end of the crystal fiber, n_1 is the refractive index of the crystal fiber core, and L is the crystal fiber length.

The laser output power P_{s_out} can be calculated by multiplying P_s with the output coupler transmittance $(1 - R_2^s)$. By solving the steady-state solution of (2.51) and (2.52), we arrive at the two sets of solutions:

$$P_{s_out} = \begin{cases} 0 & P_{in} < P_{th} \\ \eta_s (P_{in} - P_{th}) & P_{in} \geq P_{th} \end{cases} \quad (2.54)$$

Obviously, the first and the second solutions correspond to the below-threshold and above-threshold conditions, respectively. P_{in} is the input pump power, P_{th} is the threshold pump power, and η_s is the slope efficiency. P_{th} and η_s are expressed as:

$$P_{th} = \frac{P_{sat}^p}{\eta_{in}} \frac{N_{th}}{N_T - N_{th}} \quad (2.55)$$

$$\eta_s = \frac{P_{sat}^s}{2P_{th}} (1 - R_2^s) \quad (2.56)$$

where P_{sat}^p and P_{sat}^s are the pump saturation power and the signal saturation power expressed as:

$$P_{sat}^p = \frac{hcA_{core}}{\sigma_a \tau_f \lambda_p} \quad (2.57)$$

$$P_{sat}^s = \frac{hcA_{core}}{\sigma_e \tau_f \lambda_s} \quad (2.58)$$

and N_{th} is the population inversion at the laser threshold:

$$N_{th} = -\frac{\ln[R_1 R_2 \exp(-2\alpha_{pl}^s L)]}{2L(\sigma_e - \sigma_{esa}^s)} \quad (2.59)$$

As we can see, σ_{esa}^p does not appear in this lumped model, so the pump ESA effect is neglected. This will limit the accuracy of this model, especially for cases where N_2 is high.

In the case with minor pump absorption and small cavity loss, the absorbed pump power can be approximated as:

$$P_{abs} = P_{in} [1 - \exp(-N_0 \sigma_a L)] \quad (2.60)$$

So we can deduce the slope efficiency η_s^{abs} with respect to the absorbed pump power:

$$\eta_s^{abs} = \frac{\lambda_p}{\lambda_s} (1 - f_L) \frac{T}{T + \ell} \quad (2.61)$$

where T is the output coupler transmittance and ℓ is the cavity loss other than T . This equation is same to the one used in [16].

Although the assumptions that lead to Eq. (2.61) may be too simplified for the crystal fibers, the equation is simple and intuitive, and provides an insight into how parameters could affect the laser performance. It is clear from this equation that the parameter f_L ($\sigma_{esa}^s / \sigma_e$) essentially limits the highest achievable laser slope efficiency. The existence of large σ_{esa}^s is the reason why η_s of $\text{Cr}^{4+}:\text{YAG}$ lasers cannot approach the quantum efficiency limit.

2.5.2 The Distributed Model for $\text{Cr}^{4+}:\text{YAG}$ Crystal Fiber Laser

Our distributed model is based on the “relaxation method” which was extensively used in fiber lasers [51]. The basic equations of the distributed model are the power evolution equations introduced in 2.3.2. To solve the laser performance, boundary conditions must be met at both ends of the cavity. A general set of boundary conditions can be written as:



$$\begin{aligned}
P_p^+(0) &= P_{p_in}^+ (1 - R_1^p) T_{c1}^p + P_p^-(0) R_1^p T_{c1}^{p2} \\
P_s^+(\lambda_i, 0) &= P_s^-(\lambda_i, 0) R_1^s(\lambda_i) T_{c1}^{s2}(\lambda_i) \\
P_p^-(L) &= P_{p_in}^- (1 - R_2^p) T_{c2}^p + P_p^+(L) R_2^p T_{c2}^{p2} \\
P_s^-(\lambda_i, L) &= P_s^+(\lambda_i, L) R_2^s(\lambda_i) T_{c2}^{s2}(\lambda_i)
\end{aligned} \tag{2.62}$$

Where $P_{p_in}^+$ and $P_{p_in}^-$ are the input pump powers at the input and output faces, respectively. R is the cavity mirror reflectance and T_c is the transmittance between the crystal fiber and the cavity mirrors. The number in the subscripts denote the end of the crystal fiber, 1 for the input end and 2 for the output end. An “s” in the superscript means the parameter is for signal light, and “p” is for the pump light. Because the signal is broadband, the reflectance and the transmittance are defined as functions of wavelength of the signal light. A schematic illustrating these parameters is shown in Fig. 2.18.

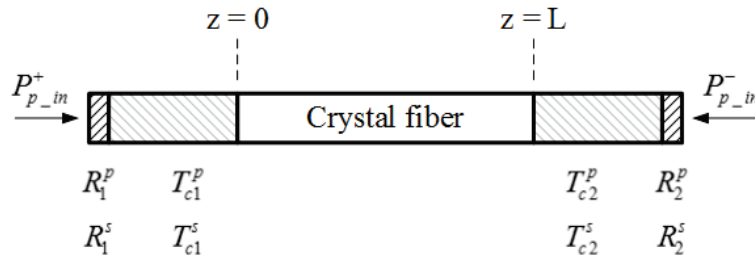


Fig. 2.18. Schematic of boundary conditions in crystal fiber laser modeling

In the relaxation method for laser modeling, the power revolution equations are numerically integrated back and forth iteratively, until a stable solution is reached. At first, we assume pump distributions $P_p^\pm(z)$ with an exponential or linear decay along the distance. The shape of the pump distribution does not affect the final solution but only has influence on the time required for convergence. With the assumed pump distribution and zero signal power, we can solve $N_2(z)$ with (2.27). After $N_2(z)$ is known, the integrations of the forward powers in (2.36) and (2.37) are worked out from $z = 0$ to $z = L$, with the forward initial conditions determined from (2.62). After that, the backward integration is carried out with updated initial backward conditions and $N_2(z)$. The integration is the repeated back and forth iteratively, and after each integration the initial conditions for the next integration and $N_2(z)$ are updated. If N_2 is over-depleted in the one integration, then the next integration in the opposite direction will lower the signal

power and under-deplete N_2 , similar to the relaxation oscillation in real lasers. During the iterations, the laser output spectrum gradually converges to a final solution. When the largest error between two successive spectra is less than a given tolerance of 10^{-6} , the iteration is stopped.

Although this model is both spatially-resolved and spectrally-resolved, we found that the multi-wavelength simulation of the crystal fiber laser is very time-consuming. This is due to the huge amount of calculations for the multi-wavelength simulation, especially when the simulated condition is close the laser threshold. Since $\text{Cr}^{4+}:\text{YAG}$ is a 4-level system, the laser spectrum should be independent of the population distribution, unlike the 3-level Er^{3+} -doped fiber laser in [51]. Thus there is no need to do the multiple wavelength simulation for a $\text{Cr}^{4+}:\text{YAG}$ crystal fiber laser. So in this dissertation, all laser simulations are carried out with single signal wavelength.

Comparisons between the lumped model and the distributed model were made with a ideal cavity with single-directional pumping and crystal fibers with different lengths. The material parameters are based on Table 2.2, except for a τ_f of 2.7 μs . The crystal fiber has a core diameter of 17 μm and a propagation loss of 0.04 dB/cm for both pump and signal. The transmittance of output coupler is 0.5% for the laser and 100% for pump. Otherwise the cavity is lossless for both pump and signal. The laser wavelength is 1431 nm. The simulation results are shown in Fig. 2.19.

For the case with $L = 2$ mm, the outcome of the two models matches very well. But when the L is increased to 50 mm, the distributed model predicts a significantly lower η_s and a higher P_{th} than the lumped model. The reason of this large difference can be explained by the intra-cavity pump distribution appeared in Fig. 2.20. The lumped model assumed that the pump power is constant along the crystal fiber, which is obviously not correct. This will exaggerate the laser performance, especially for long crystal fibers which absorbs most of the pump. Thus the distributed model must be used for fitting or predicting the performance of the crystal fiber lasers.

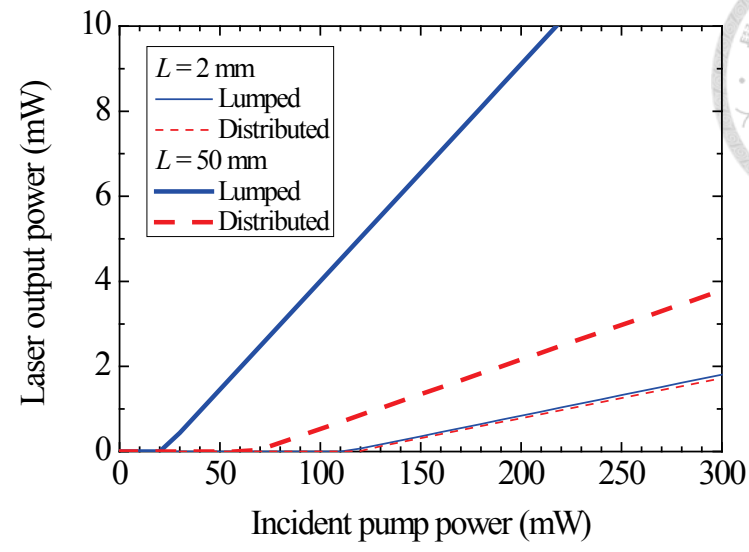
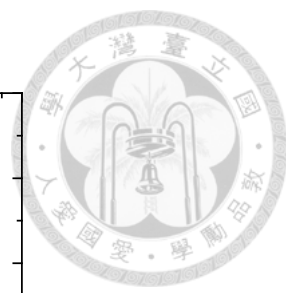


Fig. 2.19. Comparison between the lumped model and the distributed model. The thin lines are for $L = 2$ mm and the thick lines are for $L = 50$ mm. Solid lines: lumped model. Dashed lines: distributed model.

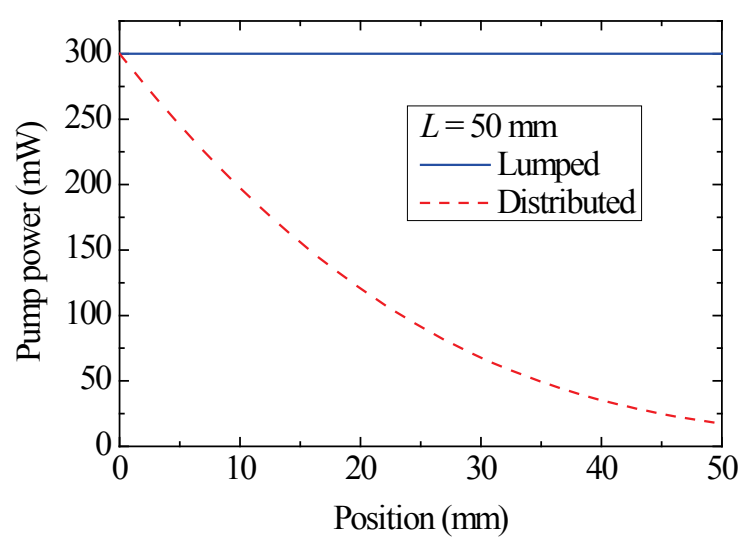


Fig. 2.20. The intra-cavity pump power distribution along the crystal fiber. Solid line: lumped model. Dashed line: distributed model.

Chapter 3

High-Brightness Broadband Light Sources by Ce^{3+} :YAG Crystal Fibers



As discussed in section 2.1, the conversion efficiency of Ce^{3+} :YAG is high due to the near-unity quantum yield. Ce^{3+} :YAG is often used as the phosphor in the white light emitting diodes (LEDs). The high-power LEDs today can generate output powers up to several watts. However, the brightness is limited by the large emitting size, which is typically $1 \text{ mm} \times 1 \text{ mm}$ or larger. A light source with lower brightness is harder to be collimated or focused into a small spot. Increasing the current or reducing the dimension of the LED chip both increase the current density and lead to the well-known “efficiency droop” [52]. Therefore, it is not easy to have huge improvements in the brightness of the LEDs.

The Ce^{3+} :YAG crystal fiber preserves the high efficiency of the Ce^{3+} :YAG crystal, and the emission size is shrunk to only tens of microns. The waveguide structure provides confinement to both the pump and the fluorescence light. By using the GaN laser diode as the pump source, tens of milliwatts output power can be generated in the small core area. As a result, the Ce^{3+} :YAG crystal can provide a brightness much higher than the high power LEDs. In this chapter, we present the demonstration of high-brightness Ce^{3+} :YAG crystal fiber broadband light sources.

3.1 Fabrication of Ce^{3+} :YAG Crystal Fibers

3.1.1 Laser-Heated Pedestal Growth System

The laser-heated pedestal growth (LHPG) method was first developed by Fejer *et al.* in 1984 [19]. This method allows the growth of single crystals with diameters as small as a few microns. The floating molten zone is supported by the source material itself and thus contamination can be minimized.

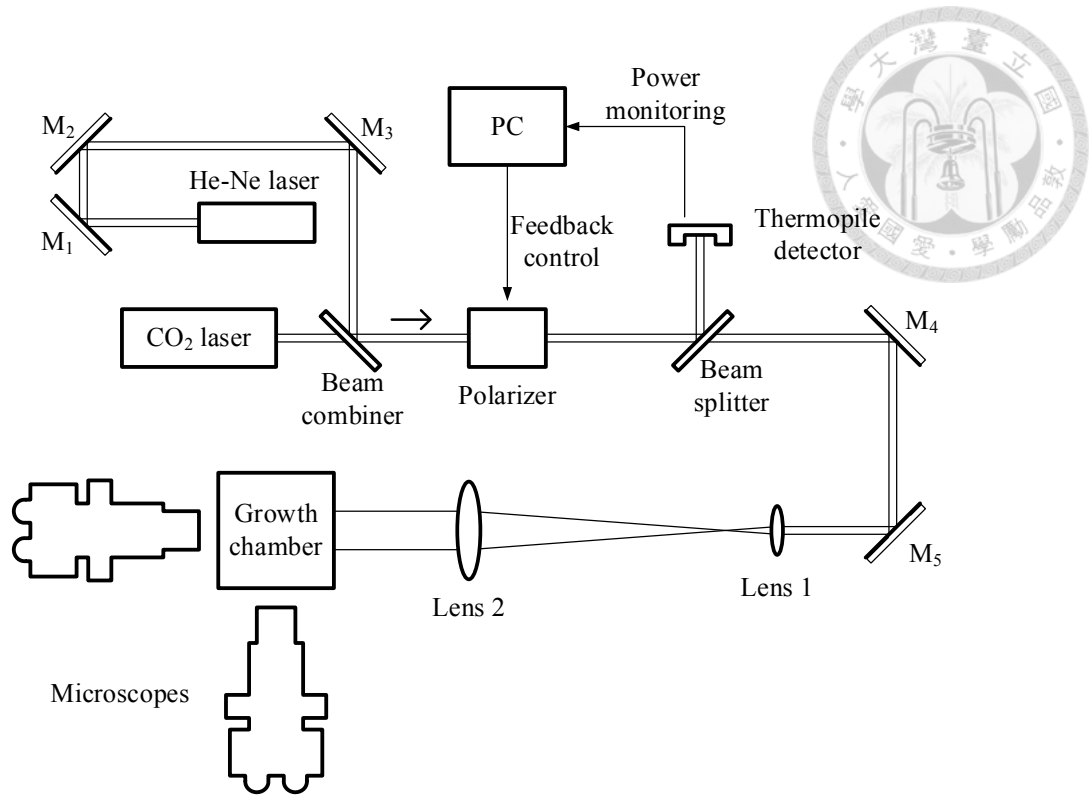


Fig. 3.1. Schematic of the LHPG system. $M_1 \sim M_5$: mirrors. PC: personal computer.

A schematic diagram of the LHPG system is shown in Fig. 3.1. A 50-W CO_2 laser (GEM-50L, Coherent) was used as the heat source for melting the source crystal. A He-Ne laser was combined with the CO_2 laser to visualize the optical path. The laser power can be adjusted by varying the duty cycle of a 24-kHz RF driving signal sent into the CO_2 laser driver. In the experiment, the laser stability was found to be dependent on the RF duty cycle. In order to reduce the laser instability, the duty cycle was fixed at the level with the highest power stability. The power went into the growth chamber was adjusted by rotating a polarizer, since the CO_2 laser was linearly polarized with a polarization extinction ratio $> 100:1$. A polarization-insensitive beam splitter after the polarizer split part of the power for monitoring. The CO_2 laser power went into the growth chamber was further stabilized with a feedback system. The polarizer angle was automatically adjusted based on the monitored laser power. Before going into the growth chamber, the CO_2 laser beam diameter was expanded from 1.8 mm to 30 mm with a pair of convex ZnSe lenses. Two stereo microscopes with long-working distance parfocal objective lenses were placed aside the growth chamber for observation of the molten zone. A laser micrometer (LS-7010, Keyence) was mounted on the top of the growth chamber for monitoring the

diameter of the grown crystal fiber. A LabVIEW program was developed to control the entire LHPG system.

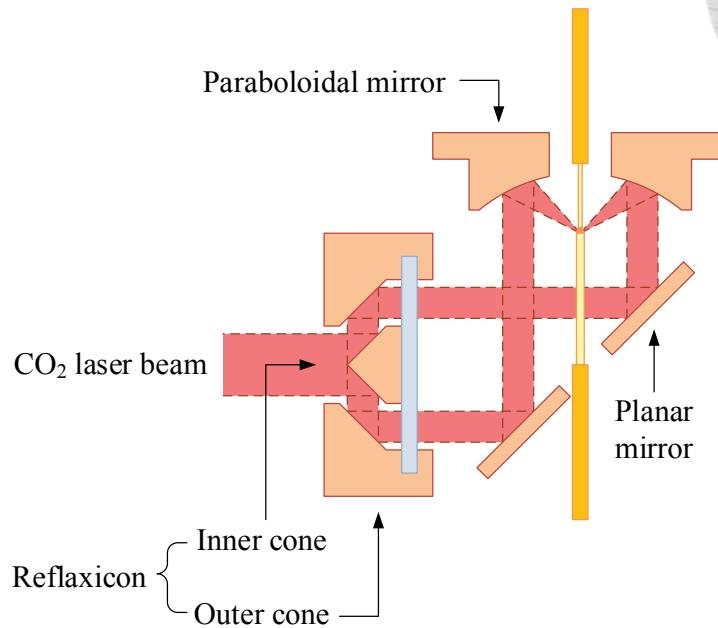


Fig. 3.2. A schematic illustration of the growth chamber. The CO₂ laser beam after the reflexicon is a doughnut-shaped beam instead of two split beams.

A schematic diagram of the growth chamber is shown in Fig. 3.2. The CO₂ laser beam was transformed into a doughnut-shaped beam with a reflexicon [53]. The inner cone of the reflexicon was mounted on a ZnSe plate which has high transmission for the CO₂ laser beam. Comparing to the conventional LHPG system which used four rods to support the inner cone, this design maintains the cylindrical symmetry of the laser beam. The ring was then reflected upward by a planar mirror and then focused by a paraboloidal mirror with a focal length of 25 mm. The estimated focal spot size of the CO₂ laser was 25 μm. There are clearance at the center of the planar mirror and the paraboloidal mirror to let the source material and the seed crystal to go through. The source crystal and the seed crystal was hold with fixtures modified from brass rods with a diameter of 6.35 mm. The holders were mounted 5-axis manual fiber positioners, which were mounted on motorized linear stages for feeding the source material upward and drawing the crystal fibers.

3.1.2 Single Crystal Fiber Growth

The source rod was mounted onto the lower motorized stage in the LHPG system.

The top of the source rod was placed at the laser focal spot in the growth chamber. A schematic illustration of single crystal fiber growth is shown in Fig. 3.3. The power of the CO₂ laser was then adjusted to melt the top of the source rod. The seed crystal, which was mounted on the upper motorized stage, was then pushed toward the molten zone, as shown in the left part in Fig. 3.3. After touching the molten zone, the seed crystal is pulled upward for crystal fiber growth, and the source crystal is fed upward for supplying the materials into the molten zone.

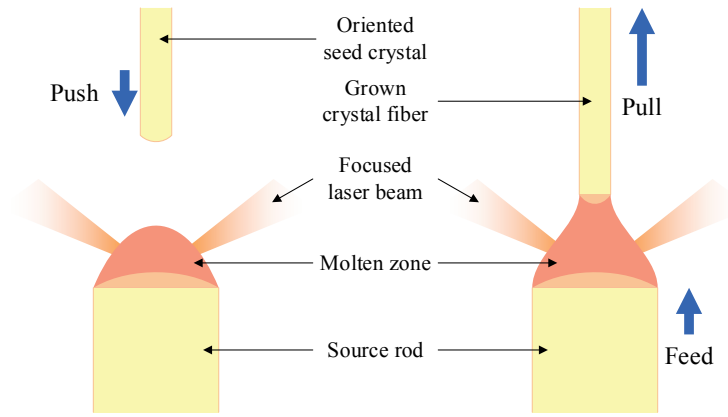


Fig. 3.3. Illustrations of the single crystal fiber growth. Left: Before the crystal fiber growth. Right: During the crystal fiber growth.

The growth of single crystal fibers obeys the mass conservation. The mass of the source materials sent into the molten zone equals to that brought away by the growing crystal fiber. In the steady state, the ratio between the cross sectional area of the crystal fiber, A_f , and that of the source rod, A_s , can then be determined by the following equation:

$$\frac{A_f}{A_s} = \frac{\rho_s v_s}{\rho_f v_f} \quad (3.1)$$

Where ρ_s and ρ_f are the volumetric mass densities of the source material and the grown crystal, respectively. v_s and v_f are the moving speeds of the source rod and the grown crystal fiber, respectively. Because we use the bulk crystal as the source material, ρ_s and ρ_f are the same. If both the source rod and the crystal fiber have circular cross sectional areas, the ratio between their diameters will be:

$$\frac{D_f}{D_s} = \sqrt{\frac{v_s}{v_f}} \quad (3.2)$$

where D_s and D_f are the diameters of the source rod and the grown crystal fiber, respectively. The shape of the molten zone will become unstable if the diameter D_s and D_f differs too much. In practice, the lowest limit of D_f/D_s is about 1/4. If the goal diameter is smaller than 1/4 of that of the source rod, the growth process was then separated into multiple steps, each of which has a diameter ratio above 1/4.

The target diameter of the Ce^{3+} :YAG single crystal fiber is 25 μm . A bulk Ce^{3+} :YAG crystal was cut in to rectangular rods with a 500 $\mu\text{m} \times 500 \mu\text{m}$ cross section to serve as the source material. The rectangular rod was first grown into a crystal fiber with a 290- μm diameter. The 290- μm crystal fiber was then used as the source rod to grow a 100- μm crystal fiber. Finally the 100- μm crystal fiber was grown in to the 25- μm crystal fiber.

3.1.3 Thermal Annealing

Annealing the Ce^{3+} :YAG single crystal in either oxidizing or reducing atmosphere was found to be helpful for reducing the impurity color centers [54], [55]. Since the temperature is much higher than the softening temperature of Pyrex glass, the annealing process must be done before the cladding process.

The grown 25- μm crystal fiber was placed on an Al_2O_3 plate, and the plate was placed into the furnace chamber. A high-temperature furnace (Model L9/12/P320, Nabertherm) with a maximum working temperature of 1200 $^\circ\text{C}$ was used. The annealing environment is ambient atmosphere (air). An example of the temperature profile is shown in Fig. 3.4. The furnace was heated from the room temperature to 1000 $^\circ\text{C}$ with a rate of 1 $^\circ\text{C}$ per minute. The sample was then soaked under 1000 $^\circ\text{C}$ for a certain time. Different soaking times of 1 hour, 4 hours and 16 hours were tried. After soaking, the furnace was cooled to room temperature again with a rate of 1 $^\circ\text{C}$ per minute. The furnace also recorded the actual temperature in the furnace. When the temperature approaches the room temperature, it deviates away from the designed profile since the furnace has no active cooling. When the temperature drops to less than 100 $^\circ\text{C}$, the sample was taken out from the furnace. The crystal fiber was then inserted into a Pyrex capillary for the cladding process.

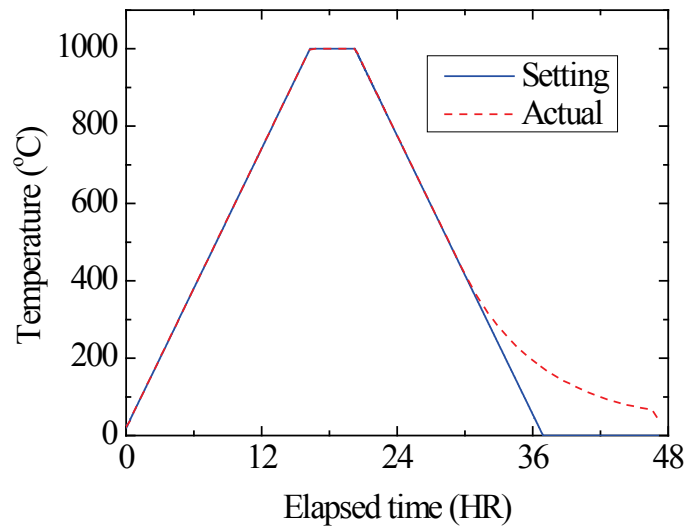


Fig. 3.4. Annealing temperature profiles with a soaking time of 4 hours. Solid line: programed profile. Dashed line: Actual profile.

3.1.4 Glass Cladding Process

Comparing to the single crystal fiber, the glass-clad crystal fiber provides a more robust waveguide. The guiding properties of the crystal core are not affected by the environmental variation, such as the application of the thermal grease or metal packaging. The glass cladding also reduces the propagation loss of the crystal fiber.

The cladding process was done by inserting the single crystal fiber into a glass capillary, and then the glass capillary was fused onto the crystal fiber. The material of the capillary is Corning 7740, which is widely known as the Pyrex glass. The refractive index of Pyrex is 1.474 at the wavelength of 589.3 nm. Since the YAG crystal has a refractive index of 1.8326 at the same wavelength, the fluorescence emission within the cone angle of 36.5° can be captured by the waveguide.

The fusing process was also done by the LHPG system, as illustrated in the left part of Fig. 3.5. The capillary with the crystal fiber was placed into the growth chamber, and the upper side of the capillary was connected to a vacuum pump. After sealing the capillary tip by the CO₂ laser, the capillary was vacuumed to minimize the residual air between the crystal fiber and the capillary. The capillary was then pushed downward. The part of the glass wall which passed through the CO₂ laser focus would melt and collapse onto the crystal fiber. The right side of Fig. 3.5 shows the photo of the crystal fiber during the cladding process.

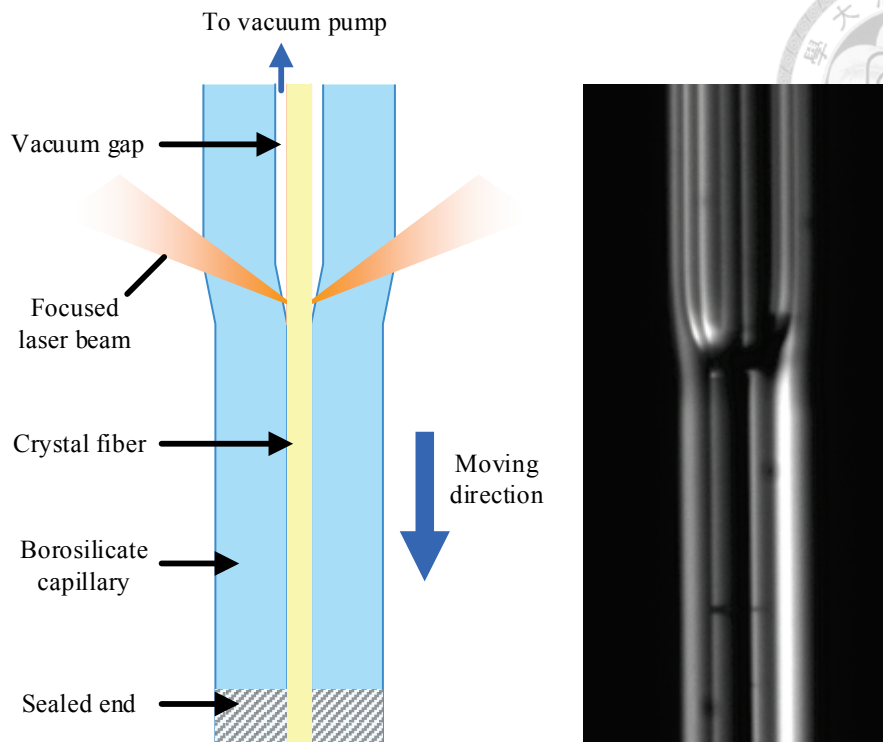


Fig. 3.5. Left: Illustration of the glass cladding process. Right: Photo of the crystal fiber during the cladding process.

After the cladding process, the crystal fiber was placed in an aluminum holder, and molten tin was poured into the holder to fix the crystal fiber. This tin packaging method improves the thermal dissipation of the crystal fiber. The packaged fibers were then cut into pieces with desired lengths. Both ends of each section of crystal fiber were ground and polished for later optical measurement.

3.2 Conversion Efficiency Optimization of Ce^{3+} :YAG Crystal Fibers

In order to verify the effectiveness of the annealing, two crystal fibers were prepared for measuring the optical conversion efficiency. One of the samples was as-grown and the other was annealed with the soaking time of 1 hour. The lengths are 8.3 and 8.5 mm for the as-grown sample and the annealed sample, respectively. The core diameters of both samples are 18 μm .

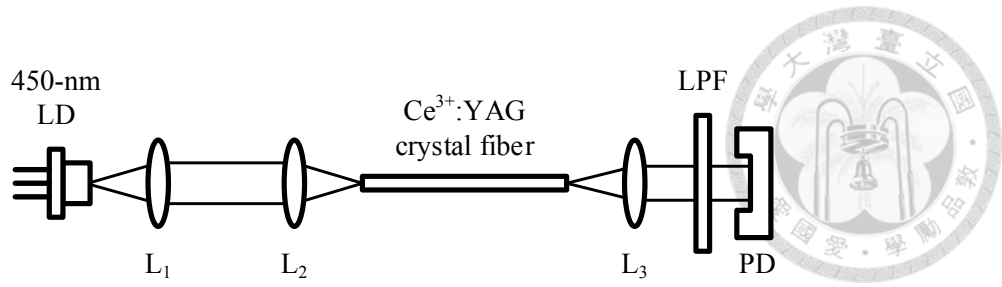


Fig. 3.6. Setup for measuring the forward fluorescence. LD: laser diode. L₁–L₃: aspheric lenses. LPF: long-wavelength-pass filter. PD: photo diode.

The measurement setup is shown in Fig. 3.6. A 1.4-W 450-nm laser diode (PL-TB450, Osram) was used as the pump light source. The pump light was collimated by an aspheric lens (L₁) with $f=4.5$ mm and $NA=0.5$ (5722-H-A, New Focus) and then coupled into the crystal fiber by another aspheric lens (L₂) with $f=2.8$ mm and $NA = 0.65$ (5721-H-A, New Focus). The forward fluorescence output from the other end of the crystal fiber was collimated with another aspheric lens, L₃, which was identical to L₂. A long-wavelength-pass filter (LPF) (BLP01-488R-25, Semrock) was used to block out the residual pump light. For measuring the residual pump power, the LPF was changed to a short-wavelength-pass filter to block out the fluorescence. The conversion efficiency (CE) was determined by the ratio of the fluorescence power and the absorbed pump power, which was defined as difference between the incident pump power and the residual pump power.

The measured performance is shown in Fig. 3.7. The fluorescence of the annealed crystal fiber was apparently higher than the as-grown sample. The conversion efficiency under 100-mW incident pump power was enhanced from 0.79% of the as-grown sample to 1.24% of the annealed sample. The theoretical conversion efficiency is 2.05%, which was calculated based on the method described in section 2.4 with 98% transmittances for both L₂ and L₃. There are two possible reasons for the large difference between the measurement and the theory, one is the annealing condition which had not been optimized, and the other is the low pump coupling efficiency.

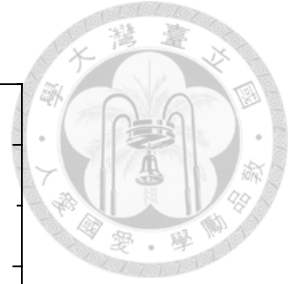
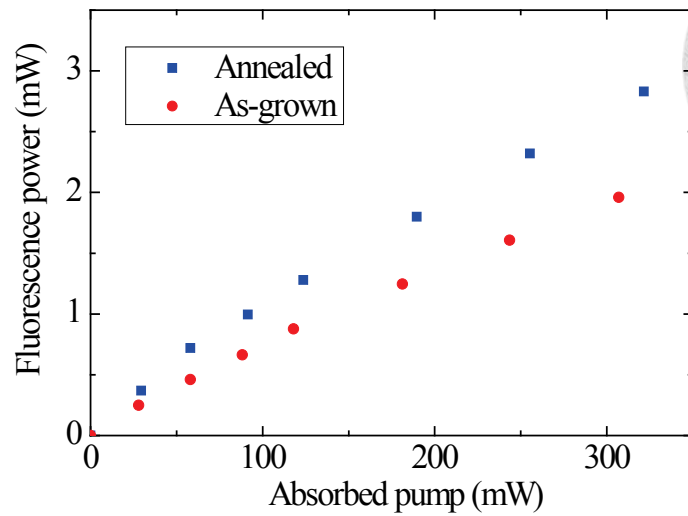


Fig. 3.7. Fluorescence power versus absorbed pump power for an as-grown crystal fiber and a crystal fiber annealed with 1-hr soaking time.

A batch of 12 crystal fibers were fabricated and divided into 3 groups with different soaking times of 1 hour, 4 hours and 16 hours. The lengths of these fibers were all about 2 cm long, and the core diameters were increased to 25 μm for better coupling efficiency. The conversion efficiencies of these samples under 100-mW pump were measured with the same setup. The results are shown in Fig. 3.8. It is obvious that the group with the 4-hr soaking time has the best efficiency. The highest efficiency among all samples is 1.95%, which was very close to the theoretical limit. The estimated quantum yield is 95%. This indicates that both the pump coupling and the crystal quality were nearly optimized. The residual pump of the sample was about 30% of the incident pump power.

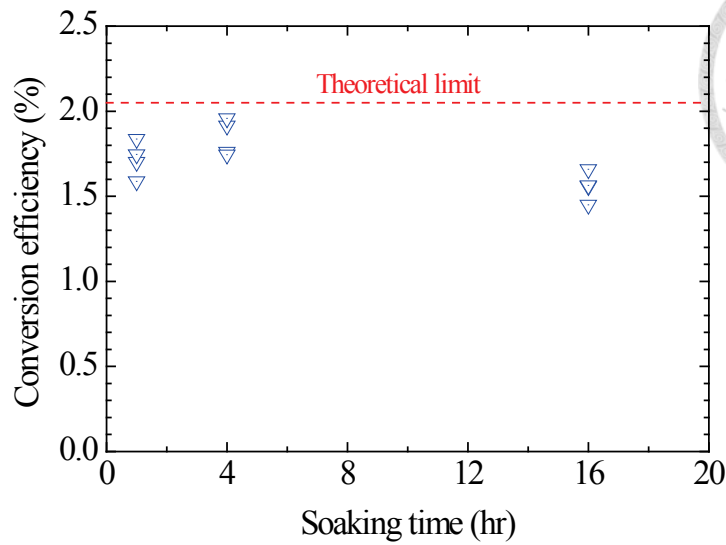


Fig. 3.8. Conversion efficiency versus the 1000 °C soaking time.

3.3 High-Brightness Ce³⁺:YAG Crystal Fiber Light Source

In Fig. 3.6, only the forward fluorescence was collected by L₃. In order to fully utilize the fluorescence power and the pump power, the optical setup was changed to Fig. 3.9. The pump light was reflected by a dichroic beam splitter (LM01-466, Semrock), DBS, and focused into the crystal fiber. The collimation lens and the focusing lens are identical to the ones used in the previous section. A broadband dielectric mirror (CVI BBD1-PM-1037-C), BBM, was attached on the opposite end of the crystal fiber to reflect both the pump light and the forward fluorescence light. The reflectance of the broadband mirror is >99% from 488 to 694 nm and about 95% at 450 nm. Dielectric coated mirror was chosen instead of metal mirror due to the higher damage threshold. The reflected forward fluorescence, together with the backward fluorescence, was collimated by L₂ and transmitted through the dichroic beam splitter. Ideally, assuming perfect alignment and no propagation loss, attaching the BBM can increase 20% pump absorption and increase 100% fluorescence by reflecting the forward fluorescence. The expected overall increase would be $(1+20\%) \times (1+100\%) - 100\% = 140\%$. For comparison between the forward and the backward fluorescence power, the forward fluorescence was also measured by removing the BBM and used the same measurement setup after the crystal fiber in Fig. 3.6. The crystal fiber used in this experiment was the one measured to have the highest conversion efficiency in the previous experiment. The fiber was 2-cm long and had a core diameter of 25 μm.

The measured fluorescence powers are shown in Fig. 3.10. The powers under 1.4-W incident pump power are 14.2 mW and 13 mW for the backward fluorescence without BBM and the forward fluorescence, respectively. The difference can be explained by smaller propagation loss experienced by the backward fluorescence than the forward one. Because the most of the fluorescence was emitted near the pumping end where the pump intensity is higher than the opposite end, the averaged propagation distance before exiting the crystal fiber would be shorter for the backward fluorescence. The conversion efficiency drops with the increasing pump power, from about 2% under 100-mW pump to 1.45% under 1.4-W pump. The reason of this efficiency decay is likely to be the thermal quenching [29].

After attaching the BBM, the highest output power under 1.4-W incident pump power came to 19.9 mW. The enhancement with respect to the backward case without the BBM is 40%, much lower than the ideal value of 140%. The results indicates that the contact between the BBM and the crystal fiber endface was not good. Inspection of the crystal fiber end face under the optical microscope revealed that, although the packaged crystal fiber had been polished to optical quality, the surrounding tin surface is still not flat within the 1 cm × 1 cm area. This problem can be overcome by using a bare crystal fiber, but the thermal dissipation may not be as good as the tin package even if thermal grease were used.

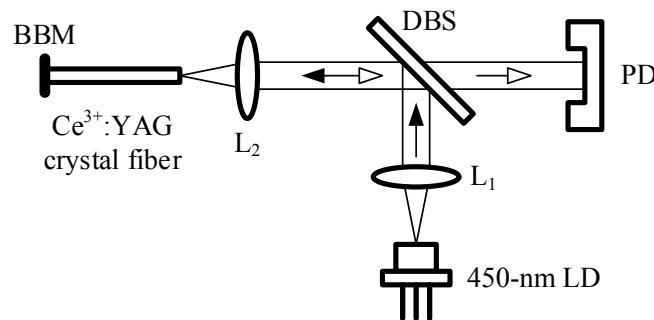


Fig. 3.9. The backward fluorescence measurement setup. BBM: broadband mirror. L₁ and L₂: aspheric lenses. DBS: dichroic beam splitter. LD: laser diode. PD: photo diode. Solid arrow: pump propagation direction. Hollow arrow: fluorescence propagation direction.

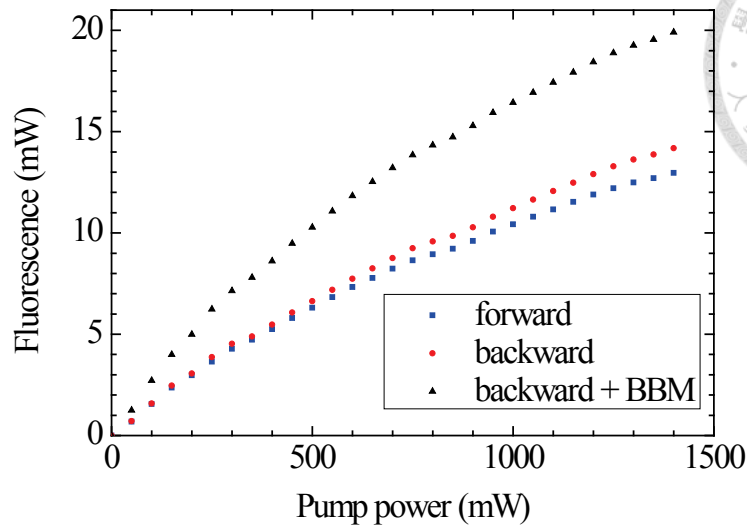


Fig. 3.10. The output fluorescence power versus the incident pump power.

The backward fluorescence spectra with and without the BBM are measured with a miniature spectrometer (USB4000-UV-VIS, Ocean Optics), as shown in Fig. 3.11. The normalized spectra are very similar because of the flat reflectance spectrum of the BBM in the fluorescence wavelength range. The 3-dB bandwidth of both spectra are 105 nm.

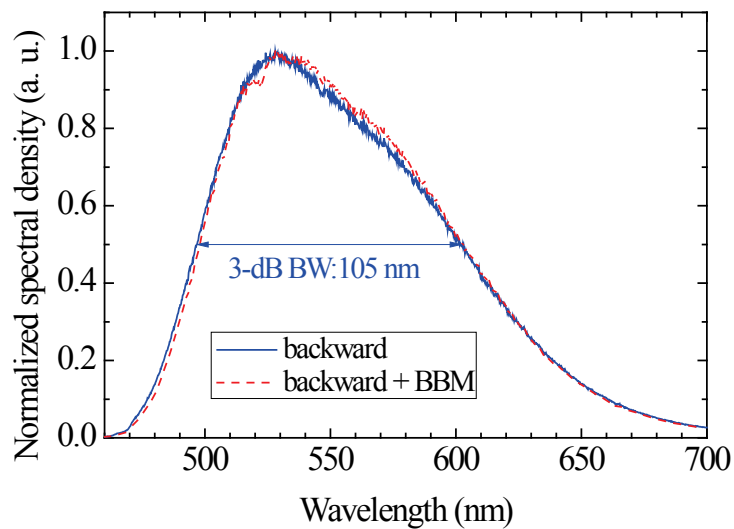


Fig. 3.11. Normalized fluorescence spectra of the Ce^{3+} :YAG backward fluorescence with and without BBM.

During the experiment it was found that the collimation lens, L_2 , has severe dispersion, thus the collimation of the output fluorescence was not good. Using an objective lens can correct this problem, at the expense of higher cost and lower

transmittance.

By assuming 98% transmittances for the collimation lens L_2 , the radiance at the crystal fiber output was calculated to be 21.57 mW sr^{-1} . The calculated brightness (radiance) distribution is shown in Fig. 3.12. The maximum radiance is $32.6 \text{ W mm}^{-2} \text{ sr}^{-1}$ at 53.3 degree away from the axial direction, and $30.3 \text{ W mm}^{-2} \text{ sr}^{-1}$ in the axial direction.

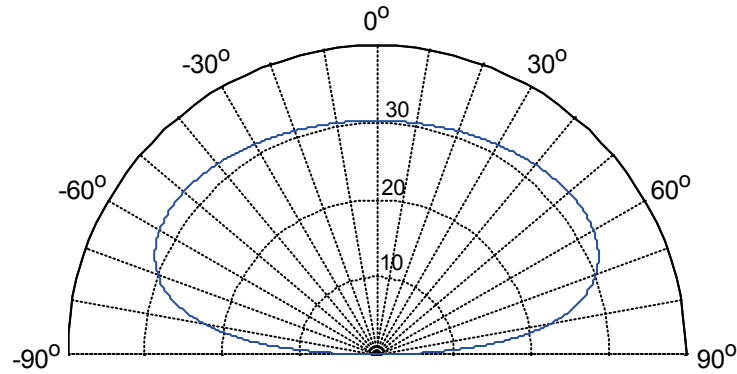


Fig. 3.12. Radiance distribution of the high-brightness crystal fiber light source. The unit of the radial scale is $\text{W mm}^{-2} \text{ sr}^{-1}$.

The output powers and radiances of the Ce^{3+} :YAG crystal fiber light source and several high-power LED light sources from Thorlabs are listed in Table 3.1. The viewing angle was defined as the full-width-half-maximum of the radiance intensity distribution. Although the power of the LEDs are high, the crystal fiber light source is still 53 times brighter than the brightest LED due to the much smaller emitting size of the crystal fiber.

Table 3.1. Characteristics of Ce:YAG crystal fiber light source and Thorlabs high-power LED light sources. [56]

Light source	λ_p (nm)	Power (mW)	Emitting area (mm^2)	Viewing angle (degree)	Radiance ($\text{W mm}^{-2} \text{ sr}^{-1}$)
Ce^{3+} :YAG	530	19.9 ^a	4.9×10^{-4}	124	30.3
MWWHL3	635	550 ^b	1	120	0.175
MCWHL5	450	840 ^b	1	80	0.571
MBB1L3	560	80 ^b	1	120	0.025
M565L3	565	979 ^b	1	125	0.289

^a Collimated output power measured with a 0.65-NA collimation lens

^b Total output power measured with an integrating sphere

The high brightness light source would be very useful if it can be coupled into communicational glass fibers, taking advantages of the wide variety of glass fiber technologies. An experiment was conducted to couple the light source into a corning SMF28e fiber. The setup is illustrated in Fig. 3.13. An aspheric lens, L_3 , with $f = 2.8$ mm and $NA = 0.65$ (5721-A-H, New Focus) was used for coupling into SMF28e.

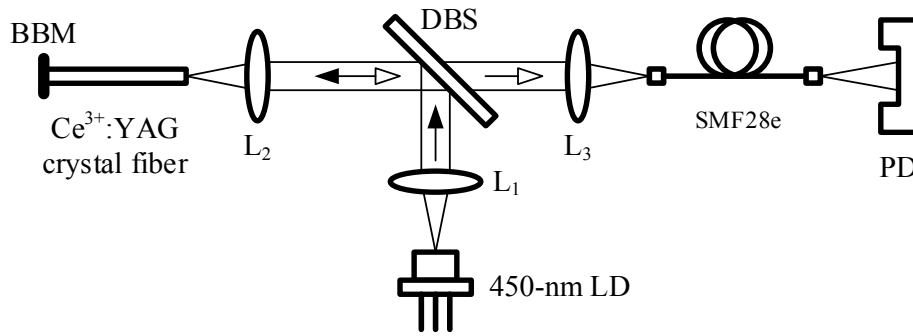


Fig. 3.13. Setup of SMF28e-pigtailed Ce^{3+} :YAG light source.

The fluorescence power output from SMF28e is shown in Fig. 3.14. The maximum output power is $47.1 \mu W$. The fluorescence spectrum is shown in Fig. 3.15. The 3-dB bandwidth is 96 nm, slightly narrower than the input spectrum. The dispersion of the aspheric lenses L_2 and L_3 is likely to be the cause of the spectral narrowing.

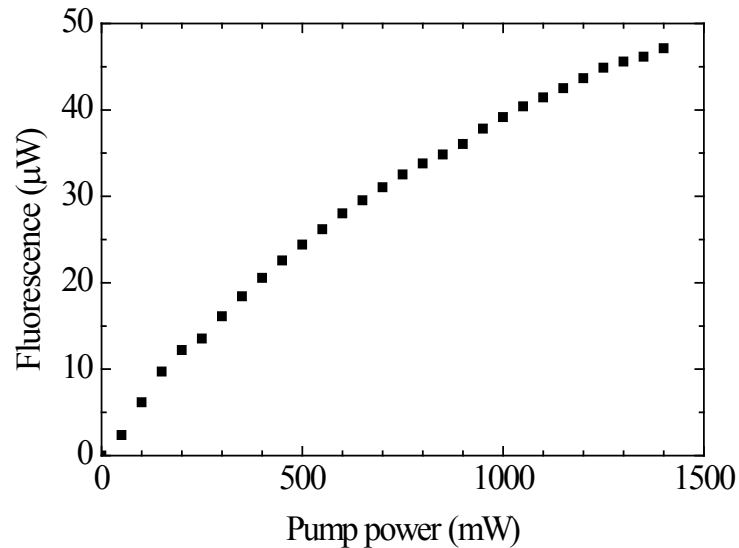


Fig. 3.14. Fluorescence power output from SMF28e fiber.

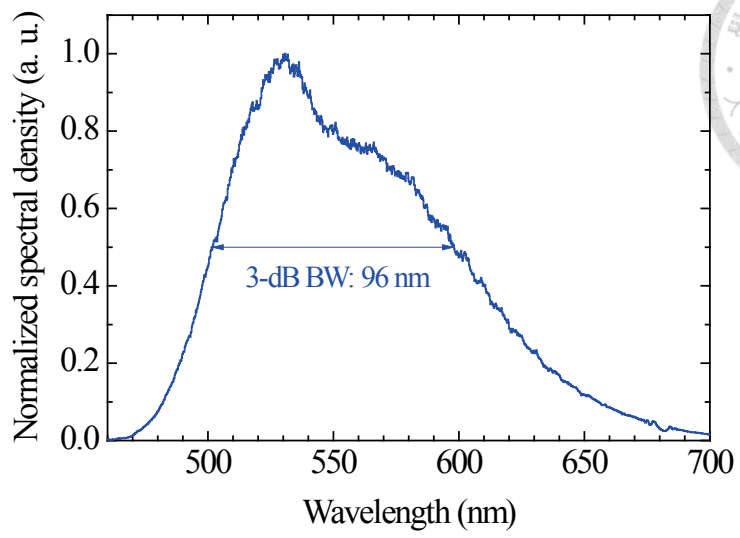


Fig. 3.15. Fluorescence spectrum output from SMF28e fiber.

Chapter 4

Broadly Tunable and Low-Threshold Cr⁴⁺:YAG

Double-Clad Crystal Fiber Lasers



In the previous work of [23], efficient Cr⁴⁺:YAG crystal fiber laser has been demonstrated with an 78.2-mW threshold pump power with only passive cooling . The laser cavity was formed by multilayer coatings deposited on both ends of the crystal fiber and the output wavelength was free-running at 1420 nm. For developing a tunable laser, the cavity must be extended to outside of the crystal fiber, so a wavelength selective element can be incorporated.

In this chapter, we present the first demonstration of external-cavity double-clad crystal fiber lasers with low pump thresholds and high slope efficiencies. The experimental results of broadly tunable crystal fiber lasers were also presented. In the last section, the performance of an optical amplifier based on the Cr⁴⁺:YAG double-clad crystal fiber was simulated.

4.1 Fabrication of Cr⁴⁺:YAG Double-Clad Crystal Fibers for Laser Applications

4.1.1 Double-Clad Crystal Fiber Growth

The single-crystal fibers were fabricated by the LHPG method with steps similar to those introduced in 3.1.2. A Cr⁴⁺:YAG single-crystalline rod with 500 μm \times 500 μm cross section was grown to a single crystal fiber with 68- μm diameter in a two-step diameter-reduction process by the LHPG system. The 68- μm single crystal fiber was inserted into a fused-silica capillary with a 76- μm inner diameter and a 323- μm outer diameter. The fiber-filled capillary was sealed by the CO₂ laser of the LHPG system at one of its ends, and vacuumed through the other end for 30 min. Since the gap between the crystal fiber and the inner wall of the capillary is as small as several micrometers, to facilitate the removal of the air in the gap, the fiber-filled capillary was pre-heated by using a CO₂ laser at a mild power to scan along the capillary. The residual air in the gap was heated and escaped out of the capillary. With the pre-heat process, the yield of the double-clad fiber growth process was significantly improved since the bubbles in the fiber caused by the

residual air were avoided.

The filled capillary was then fused by the sapphire-tube-assisted co-drawing LHPG (CD-LHPG) process [21]. Before we introduce the sapphire-tube assisted CD-LHPG process, it is worth to describe first the CD-LHPG process without sapphire tube. In this process, the pre-heated capillary was heated by the CO₂ laser and attached to the crystal core for cladding formation. Since the 1600 °C softening point of the fused silica is close to the 1960 °C melting point of the Cr⁴⁺:YAG crystal, both central part of the fused silica capillary and the outer part of Cr⁴⁺:YAG crystal fiber melted during the growth process. The molten fused silica mixed with the molten crystal and formed an additional inner cladding layer in between the crystal core and the cladding, as shown in Fig. 4.1. Because part of the crystal core was consumed by the formation of the inner cladding layer, the core diameter was reduced.

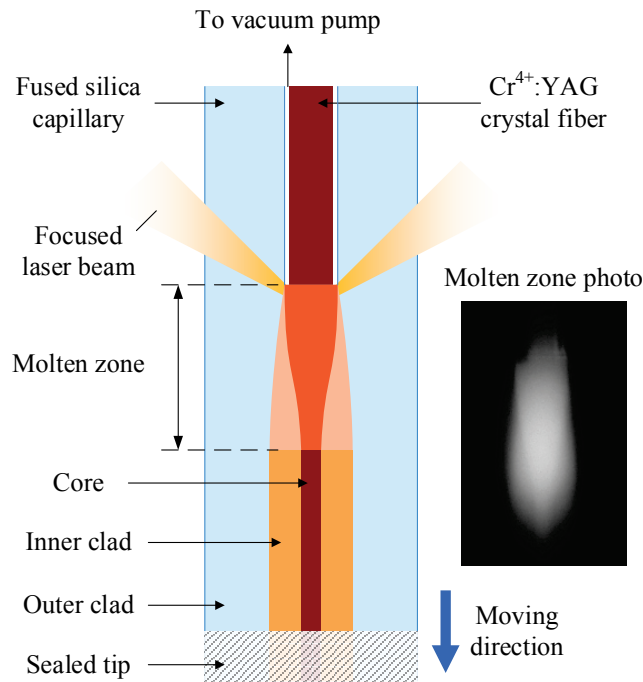


Fig. 4.1. An illustration of the CD-LHPG growth of the Cr⁴⁺:YAG double-clad crystal fiber. The inset photo showing the funnel-shaped molten zone was captured during the fiber growth.

The sapphire-tube-assisted CD-LHPG technique was developed for enhancing the core diameter uniformity and reducing the propagation loss. In the CD-LHPG process, the uniformity of the core diameter was sensitive to the power stability of the CO₂ laser. To reduce this sensitivity, a sapphire tube with a 500- μ m inner diameter and a 1200-

μm outer diameter was used to serve as a heat capacitor. The sapphire tube was placed at the focal spot of the CO_2 laser, and the fused silica capillary filled with a single crystal fiber went through the center of the sapphire tube. The sapphire tube was heated by the CO_2 laser and generated strong thermal radiation to melt the filled capillary. The stability of the thermal radiation from the sapphire tube is better than that of the CO_2 laser, due to the thermal capacity provided by the sapphire tube. Therefore, this indirectly heating approach can produce crystal fibers with better core uniformity and lower propagation loss. Besides, compared with the focal spot of the CO_2 laser, the heated sapphire tube provides longer heating time, which could benefit the crystal quality due to the annealing effect. The smallest core diameter that can be stably produced with the sapphire-tube-assisted CD-LHPG process is $10\ \mu\text{m}$, half of the smallest single-crystal fiber diameter can be achieved with the conventional LHPG process. The measured propagation loss of the double-clad crystal fiber with $10\text{-}\mu\text{m}$ core was $0.02\ \text{dB/cm}$ [21].

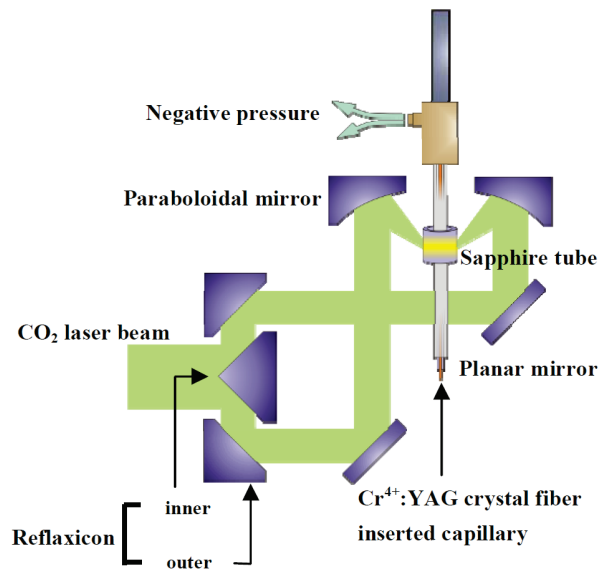


Fig. 4.2. An illustration of sapphire-tube-assisted LHPG system.

A typical index profile of the Cr^{4+} :YAG double-clad crystal fiber is shown in Fig. 4.3. The index profile was measured by a laser scanning microscope with a 635-nm laser source [57]. The refractive indices of the core and the outer clad are 1.82 and 1.46 , respectively. The refractive index of the inner clad changes gradually from 1.60 near the outer clad to 1.66 near the core.

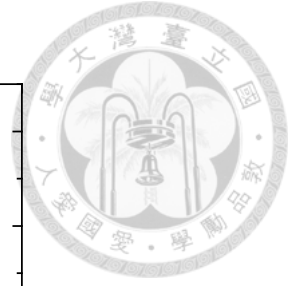
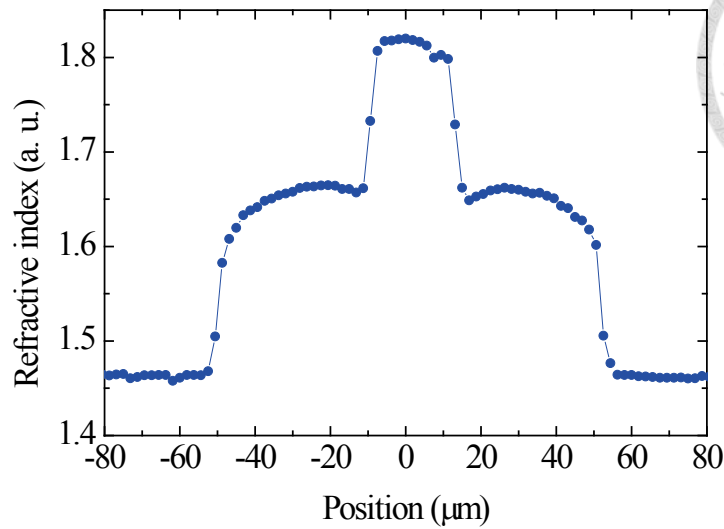


Fig. 4.3. Refractive index profile of a Cr^{4+} :YAG double-clad crystal fiber.

The optimal core diameter for minimizing the residual strain inside the double-clad crystal fiber is about $20\ \mu\text{m}$ [58]. Although a smaller core diameter can effectively reduce the pump threshold, a large deviation from the $20\text{-}\mu\text{m}$ core diameter can significantly reduce the laser efficiency due to the large residual strain. In this dissertation, double-clad crystal fibers with core diameters from 17 to $19\ \mu\text{m}$ were used for laser experiments.

4.1.2 Dielectric Coating Deposition

The as-grown double-clad crystal fiber was examined under the optical microscope. Regions with defects or core diameters which did not meet the requirements were marked with the marker pen. A section of crystal fiber with desired length was then cut out with a diamond-tip scribe, and the marked regions were avoided. In the next step, the crystal fiber was fixed in a specially designed aluminum holder with a thermoplastic adhesive (Crystalbond 509). Finally, both surfaces of the packaged sample were ground and polished for dielectric coating deposition.

In order to build up an external-cavity crystal fiber laser, one end of the crystal fiber was deposited with highly reflective (HR) coating and the other end with anti-reflective (AR) coating. The HR coating serves as the cavity mirror, and the AR coating reduces the intra-cavity loss and suppresses the sub-cavity formation. The coatings are $\text{SiO}_2/\text{TiO}_2$ stacks deposited by an E-gun deposition system at a substrate temperature of $280\ ^\circ\text{C}$. The spectra of the coating on the crystal fiber endface was derived from the measured transmission spectra of the test glass plates, as shown in Fig. 4.4. The transmission of the

HR coating at the 1064 nm pump wavelength was as high as 94.8%, and the transmission in the 1350 to 1500 nm laser operation window was below 0.6%. The AR coating has a transmittance of 97.4% at 1064 nm and above 99.3% in the 1350 to 1500 nm wavelength range. The microscope photo of the coated fiber endface is shown in Fig. 4.5. The core and inner cladding regions were free from defects.

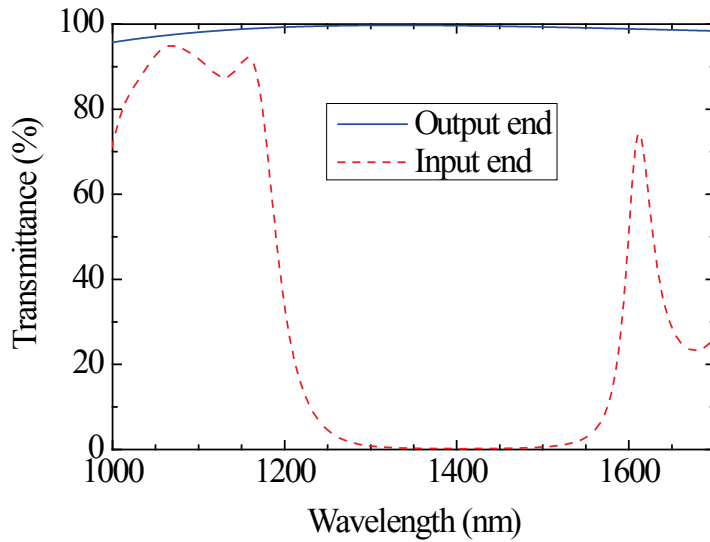


Fig. 4.4. Transmission spectra of the coatings on both ends of the crystal fiber.

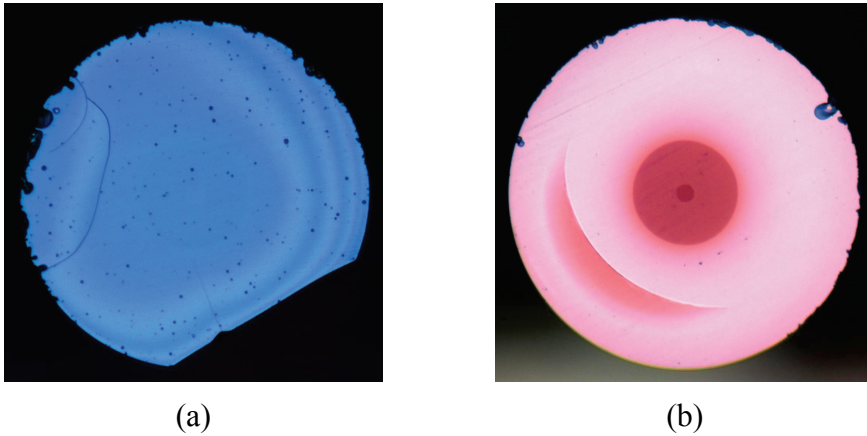
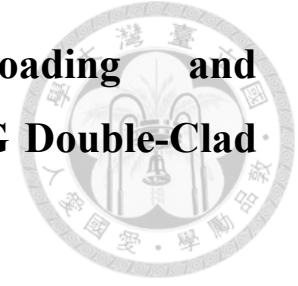


Fig. 4.5. End photo of coated crystal fiber.
(a) Input end (HR), (b) Output end (AR).

4.2 Fluorescence Lifetime Thermal Loading and Polarization-Dependent Gain of Cr⁴⁺:YAG Double-Clad Crystal Fiber



4.2.1 Fluorescence Lifetime Thermal Loading

As previously discussed in section 2.2.1, The fluorescence lifetime of Cr⁴⁺:YAG decreases with the rising crystal temperature due to the increased non-radiative relaxation rate. With smaller fluorescence lifetime, higher pump power is required for achieving the same population inversion level and thus the laser efficiency reduces. The relation between the fluorescence lifetime, τ_f , is linearly dependent on the temperature in a limited temperature range between 0 to 100 °C, as shown in Eq. (2.17).

To investigate the thermal dissipation ability of the crystal fiber, the fluorescence lifetimes of the crystal fiber and the bulk crystal were measured. A mechanical chopper (MC1000A, Thorlabs) was used to modulate the pump beam at a 1-kHz rate. The 10-slot blade (MC1F10, Thorlabs) was placed at the focal spot to achieve a fall time of 375 ns. Nine of the ten slots were blocked with aluminum foil to avoid chopping the pump beam at different axial position due to the blade deformation. The duty cycle of the chopped pump beam was 5%. The residual pump light was blocked by an edge filter. The fluorescence was detected by a 150-MHz InGaAs photodiode (PDA10CF, Thorlabs) and recorded by a digital oscilloscope (TDS320, Tektronix) with a sampling rate of 500 million samples per second.

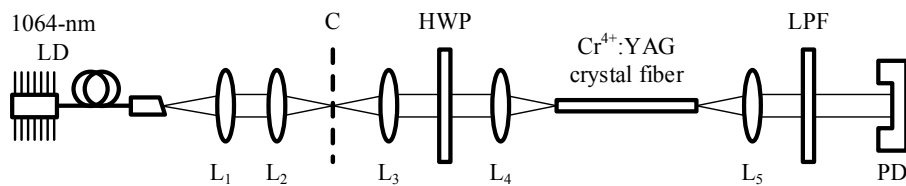


Fig. 4.6. Fluorescence lifetime measurement setup. LD: laser diode; L₁~L₅: aspheric lenses; C: chopper; HWP: half-wave plate; LWP: long-wavelength-pass filter; PD: photo diode.

A 4.4-cm long $\langle 0\ 0\ 1 \rangle$ crystal fiber with a 19- μm core diameter was used in the experiment. The sample was mounted on a copper heat sink with silver gel for passive cooling. The measured fluorescence decay curve under the 400-mW incident pump power

is shown in Fig. 4.7. The fitted fluorescence lifetime was $4.17 \mu\text{s}$. The fluorescence lifetime of a bulk $\text{Cr}^{4+}:\text{YAG}$ crystal with a size of $0.5 \text{ mm} \times 0.5 \text{ mm} \times 2 \text{ mm}$ was also measured with the same setup. The dependence of the fluorescence lifetime on the absorbed pump power of both crystal fiber and the bulk crystal was shown in Fig. 4.8. The data were measured with the incident pump powers of 10, 100, 200, and 400 mW. It is obvious that the fluorescence lifetime decreases slower with increasing pump power for the crystal fiber. The relative lifetime decreases from 10-mW to 400-mW incident pump were 1.8% and 9.8% for the crystal fiber and the bulk crystal, respectively. Substituting these values into Eq. (2.17) and use a τ_f^T of $0.0416 \mu\text{s}/^\circ\text{C}$ [40], the corresponding temperature rise was found to be 1.7°C and 9.1°C for the crystal fiber and the bulk crystal, respectively. This is a clear evidence of better thermal dissipation for the crystal fiber.

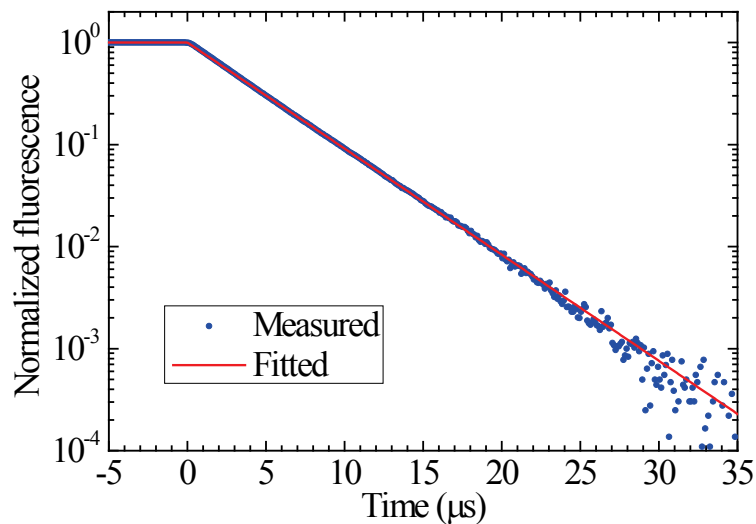


Fig. 4.7. Decay of the fluorescence intensity after blocking-off the pump. Blue dots: measured data. Red line: the exponential fit with a time constant of $4.17 \mu\text{s}$.

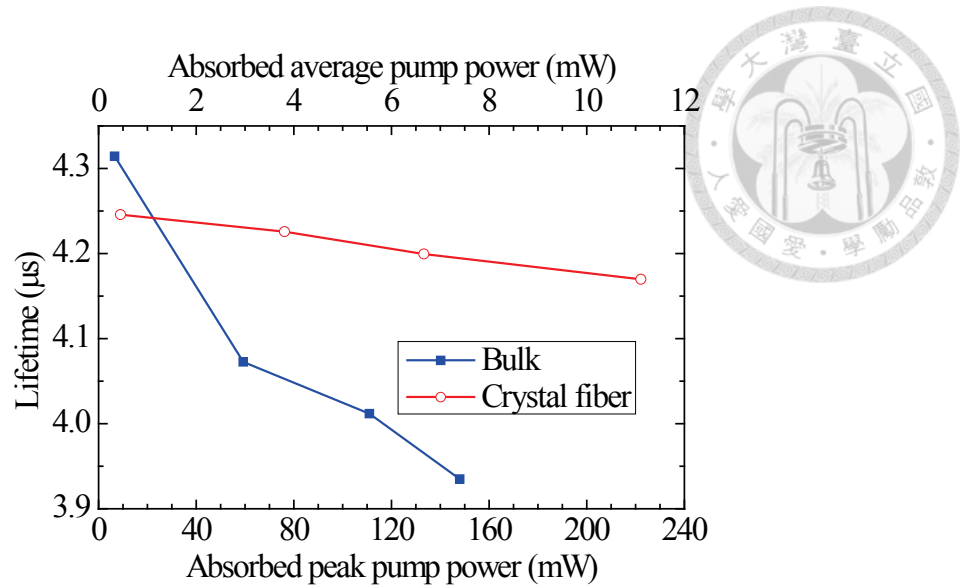


Fig. 4.8. Fluorescence lifetime vs. absorbed pump power for bulk and crystal fiber.

4.2.2 Polarization-Dependent Gain

The polarization properties of the Cr^{4+} :YAG crystal has been discussed in section 2.2.1. If the pump is polarized along one of the crystallographic axes, one of the three types of Cr^{4+} ions will be selectively excited, and the gain will be maximum for the signal light polarized along the same crystallographic axis. However, in the crystal fiber, the pump and the signal might be depolarized due to the fiber birefringence, and the gain would decrease consequently. In order to investigate the polarization properties of our crystal fiber, the following experiment was conducted for measuring the polarization dependent gain.

The setup for measuring the polarization dependent double-pass gross gain is depicted in Fig. 4.9. The pump source was a PM980-pigttailed 1064-nm diode laser (LD-1064-BF-600, Innolume). A 1410-nm SMF28e-pigttailed DFB laser was used as signal light source. A 4.8-cm long $\langle 001 \rangle$ crystal fiber with a 19- μm core diameter is prepared for this measurement. One end of the crystal fiber was coated with a multilayer dielectric coating with anti-reflection for pump light and high-reflection for the signal light. The other end was coated with broadband AR coating for both signal and pump. The polarized pump was coupled into the crystal fiber from the dichroic-coated end with a 400-mW power. The attenuated signal was polarized and then coupled into the crystal fiber at the opposite end. The power of the small signal coupled to the crystal fiber is -29.6 dBm. The

polarization of the pump and the signal can be independently rotated by the half-wave plates. After one round trip in the crystal fiber, the returned signal is split by a polarization-insensitive beam splitter and collected into an optical spectrum analyzer (70950B, Hewlett-Packard). The gross gain is defined as the ratio of the signal power with pumping and that without pumping. By examining with an infrared card we found that both the pump and the signal exhibited smooth few-mode patterns after output from the crystal fiber.

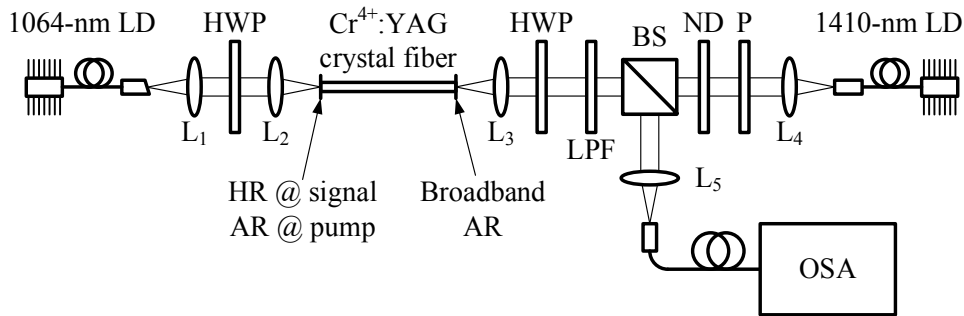


Fig. 4.9. The polarization-dependent gain measurement setup. LD: laser diode; L_1 – L_5 : lenses; HWP: half-wave plate; BS: beam splitter; ND: neutral density filter; P: polarizer; LPF: long-wavelength pass filter; OSA: optical spectrum analyzer

The measured gross gain curves are shown in Fig. 4.10 and Fig. 4.11. The gain was maximum when the polarizations of both pump and signal are aligned to the same $\langle 0\ 0\ 1 \rangle$ crystal axis. When the polarizations of the pump and signal were aligned to different $\langle 0\ 0\ 1 \rangle$ crystal axes, the gain was nearly zero. There was some difference between the peak gain values of the two orthogonal $\langle 0\ 0\ 1 \rangle$ crystallographic axes, which should be identical theoretically. This can be explained by the stress inside the crystal fiber which originated during the cooling stage of the co-drawing LHPG process. The emission cross section of Cr^{4+} :YAG is dependent on the strain [58]. If the stress inside the crystal fiber is not cylindrically symmetric, the gain on the two $\langle 0\ 0\ 1 \rangle$ crystallographic axes can become different. The stress also induces birefringence in the crystal fiber and create the depolarization loss in the laser cavity. Nevertheless, the good agreement between the measurement result and the distorted tetrahedron model indicates that the depolarization effect in the crystal fiber was minor.

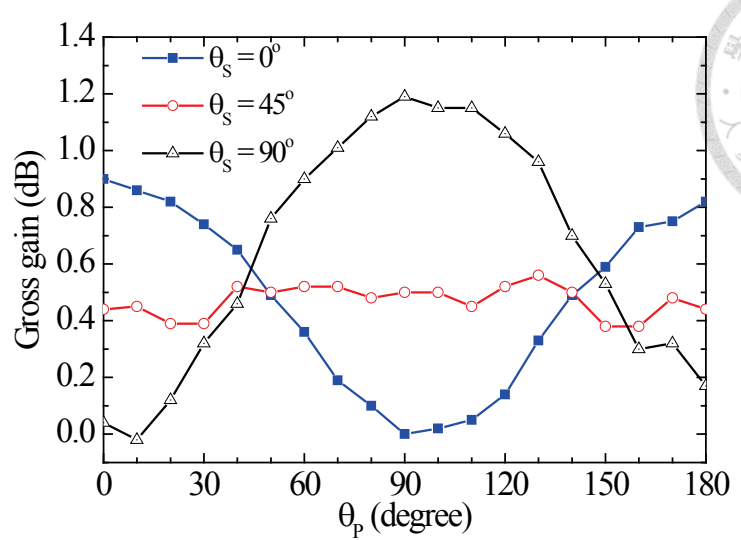
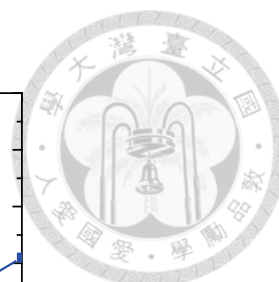


Fig. 4.10. The double-pass gross gain vs. the pump polarization angle. θ_p and θ_s : polarization angles of pump and signal with respect to the same $\langle 0\ 0\ 1 \rangle$ crystal axis, respectively. The $\langle 0\ 0\ 1 \rangle$ crystal axes are at 0° and 90° .

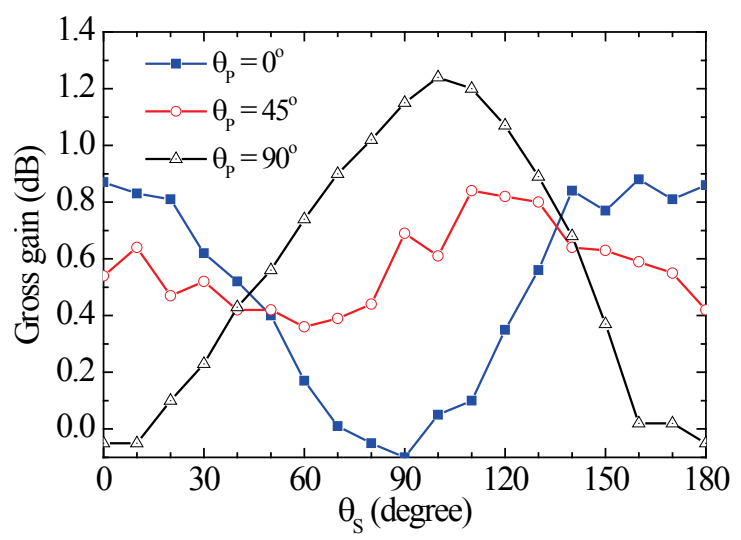


Fig. 4.11. The double-pass gross gain vs. the signal polarization angle.

4.3 Efficient and Low-Threshold External-Cavity Crystal Fiber Lasers

Two types of ECCFLs were set up for demonstrating the tunable lasers: the hemispherical cavity and the collimated cavity. The hemispherical cavity has the lowest loss since it is free of dispersion, and the spherical aberration is small because the output end of the crystal fiber is placed at the aplanatic point. However, the intra-cavity divergent

beam reduces the resolution of the wavelength tuning element based on the angular dispersion, e.g., a grating or a prism. Furthermore, it also introduces higher insertion loss when used with a BRF oriented at the Brewster's angle. The collimated external-cavity laser is thus more suitable for the tunable laser application. But the choice of the intra-cavity collimator is crucial for the laser performance.

The crystal fiber used for the following laser experiments has a length of 62 mm and a core diameter of 17 μm . One end of the crystal fiber was deposited with a dielectric coating with AR for the pump and HR for the signal. The other end was coated with broadband AR coating for both signal and pump. The transmittance of both coated end faces is shown previously in Fig. 4.4. The crystal fiber was fixed on a copper heat sink and applied with silver gel to help the heat dissipation. All data were taken with only passive cooling under room temperature.

4.3.1 Hemispherical External-Cavity Crystal Fiber Lasers

The experimental setup of the hemispherical ECCFL is shown in Fig. 4.12. A half-wave plate was used to rotate the pump polarization to match the $\langle 0\ 0\ 1 \rangle$ crystal axis of the crystal fiber. Two output couplers with 4.4% and 1.4% transmittance at the wavelength of 1452 nm were used, and the measured transmission spectra are shown in Fig. 4.13. The radius of curvature was 25 mm for both output couplers. A long-wavelength pass edge filter (LP02-1064RS-25, Semrock) was used to block the residual pump light.

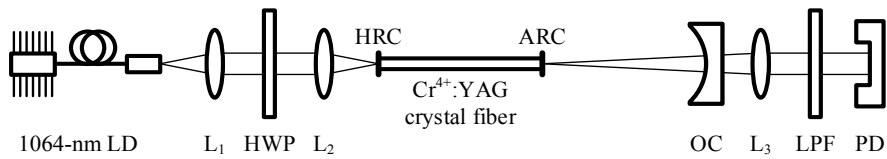


Fig. 4.12. Setup of the hemispherical ECCFL.

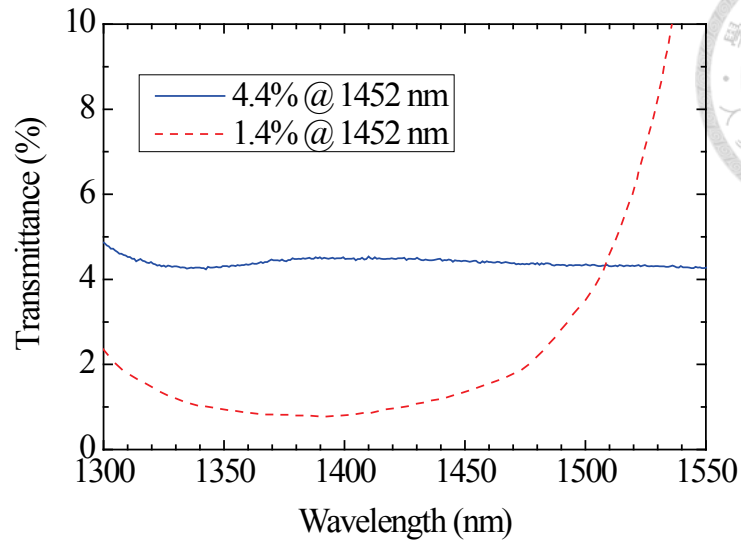


Fig. 4.13. Transmission spectra of the output couplers.

The doping concentration of the sample was determined by fitting the residual pump power. The residual pump power was measured without the output coupler, and the result is shown in Fig. 4.14. Numerical fitting gives an f_p of 0.15 and a small-signal pump absorption of 0.75 cm^{-1} . Since the small-signal pump absorption coefficient equals to $N_T \times \sigma_a$, by assuming a σ_a of $22 \times 10^{-19} \text{ cm}^2$ [59], we can get a N_T of $3.409 \times 10^{-23} \text{ m}^{-3}$.

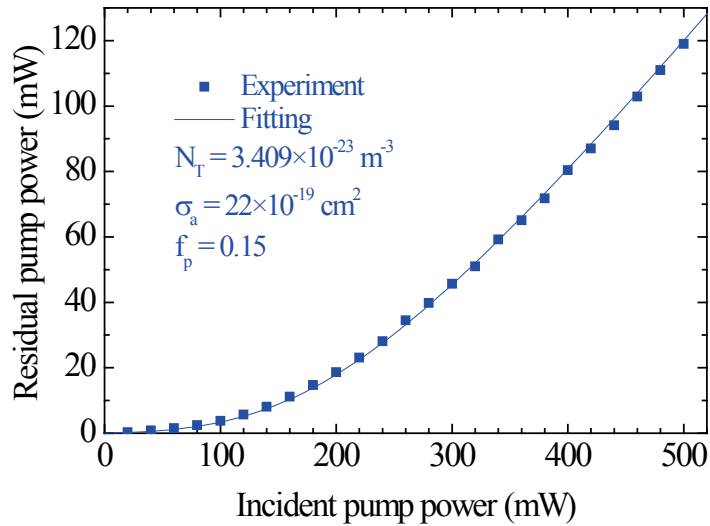


Fig. 4.14. Residual pump power of Cr^{4+} :YAG crystal fiber.

The laser output powers with different output coupler transmittance are shown in Fig. 4.15. For $T_{OC} = 4.4\%$, the threshold pump power was 56 mW and the slope

efficiency was 17.3%. Although multi-peak lasing was observed during cavity alignment, after optimization there was only a single peak centered at 1452.8 nm in the laser output spectrum, as shown in Fig. 4.16. The laser linewidth was 0.2 nm when measured by an OSA with a resolution bandwidth of 0.03 nm. The polarization extinction ratio was measured to be 30:1. A higher threshold of 61.2 mW and a lower slope efficiency of 9.6% was measured for $T_{oc} = 1.4\%$. The peak wavelength is also at 1452 nm.

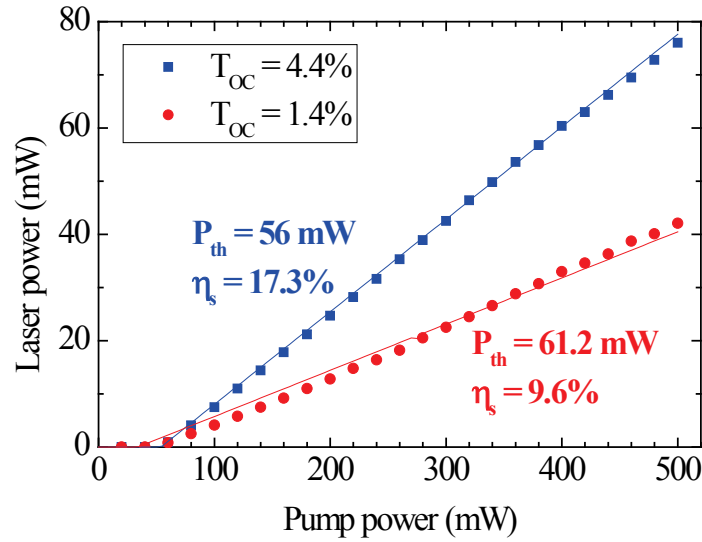


Fig. 4.15. The performance of the hemispherical ECCFL with different output coupler transmittance. Markers: measured data. Solid lines: numerical simulation.

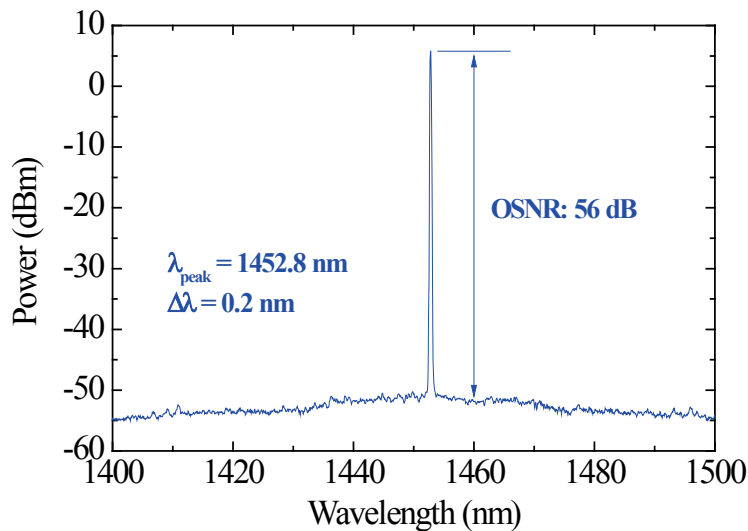


Fig. 4.16. Laser output spectrum under 400-mW pump power. The resolution of the OSA is 0.08 nm. OSNR: optical signal-to-noise ratio.

Numerical simulation was carried out for both lasers. The fitting parameters are summarized in Table 4.1, and the material parameters used are listed in Table 2.2. The transmittance of each interface in the laser cavity are determined from the coating transmission spectra in Fig. 4.4 and the output coupler transmission spectra in Fig. 4.13. Only the fluorescence lifetime and the propagation losses are adjusted for fitting the experimental results. The fitting results are also plotted in Fig. 4.15. The fitted fluorescence lifetime is 2.8 μ s, which corresponds to a temperature of 60 $^{\circ}$ C inside the crystal fiber core based on Eq. (2.17). The fitted propagation loss is 0.011 dB/cm.

Table 4.1. Cavity parameters used in the simulation. The values of R_2^p and R_2^s vary with the output couplers.

Symbol	Value	Symbol	Value
α_{pl}^p	0.01 dB/cm	α_{pl}^s	0.01 dB/cm
R_1^p	5.2%	R_1^s	99.85%
R_2^p	96.2% / 75%	R_2^s	95.6% / 98.6%
T_{c1}^p	100%	T_{c1}^s	100%
T_{c2}^p	97.4%	T_{c2}^s	99.5%

4.3.2 Collimated External-Cavity Crystal Fiber Lasers

Due to the moderate gain of the Cr⁴⁺:YAG crystal, the choice of the intra-cavity lens is crucial to the performance of the laser. An experiment was conducted in order to find out the lens with the lowest loss, and the setup is shown in Fig. 4.17. A 1410-nm DFB laser was connected to a single-mode fiber coupler at port 1. The external cavity to be measured was set up after port 2. The parameters of the lenses used in this experiment are listed in Table 4.2. All the lenses are coated with broadband AR coating at 1–1.6 μ m wavelength region. The numerical aperture (NA) of the lenses were all larger than the single-mode fiber's, which is 0.14. The collimated beam was reflected by an HR mirror placed at about 20 cm away from the collimator. The position of the lens was adjusted to either collimate or focus the beam on the mirror. Two photodiodes were placed at ports 3

and 4 for measuring the power reflected from the external cavity and monitoring the source power.



Table 4.2. Lenses used in the measurement of round-trip loss of the collimated external cavity

No.	Lens type	f (mm)	NA	Design λ (nm)
1	spherical	10	0.44	546.1
2	achromatic	10	0.37	1016, 1330, 1550
3	aspheric	2.8	0.65	830
4	aspheric	4.5	0.55	780
5	aspheric	6.2	0.4	780
6	aspheric	8	0.5	780
7	aspheric	15.4	0.16	780

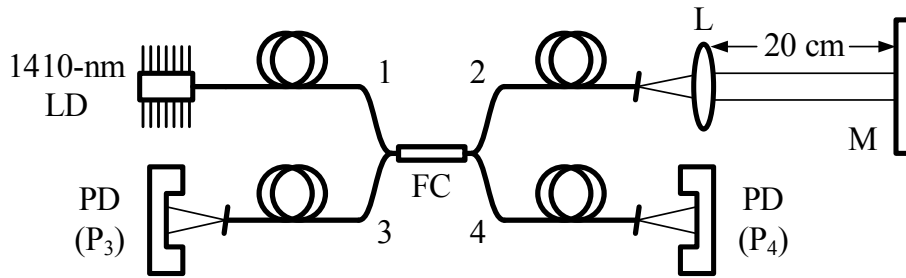
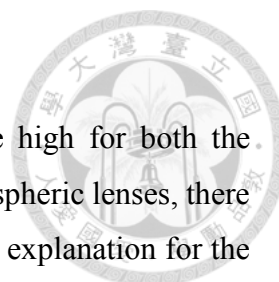


Fig. 4.17. The experiment setup for measuring the loss of the collimated external cavity. M: HR mirror; FC: fiber coupler; Numbers: number of ports of FC. The slashes indicate the FC/APC connectors.

The loss of the external cavity include the coupling loss can be calculated as:

$$L = 10 \log \frac{P_4 T_{12} (1 - R)^2}{P_3} \quad (4.1)$$

where P_3 and P_4 are the power measured at port 3 and port 4 of the coupler, respectively. T_{12} is the transmission from port 1 to port 2 and R is the reflectance of the interface between air and the core of the single mode fiber. During the experiment two loss minima were found for each lens, one corresponding to the collimating configuration and the other to the focusing configuration. The collimating configuration always has a



lower loss than the focusing one.

The measured results are shown in Fig. 4.18. The losses are high for both the spherical lens and achromatic lens due to strong aberration. For the aspheric lenses, there is a clear trend that the loss increases with the focal length. A simple explanation for the results is that there is still small aberration for these aspheric lenses because the design wavelengths are not at 1410 nm, as shown in Table 4.2. With longer focal length, the beam illuminated larger area of the lens and thus suffered stronger aberration. This aberration reduced the coupling efficiency due to the small focal size. The focal length of the lens with the lowest loss of this experiment is 2.8 mm. Although the results were obtained with single-mode fibers, using a lens with smaller aberration should also reduce the loss of the external cavity with the multi-mode crystal fibers. For the following collimated ECCFL experiment, we chose a similar lens with a 2.97-mm focal length but designed at 1550 nm, much closer to the center wavelength of the Cr⁴⁺:YAG laser. Both lenses were tested in the collimated ECCFL experiment and a slightly better performance was measured for the latter one.

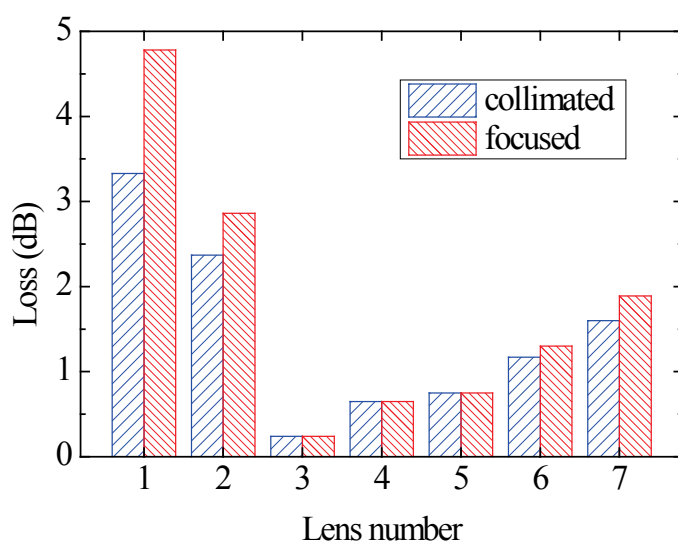


Fig. 4.18. The measured external cavity loss with different intra-cavity collimators. Refer to Table 4.2 for lens details.

The setup of the collimated ECCFL is shown in Fig. 4.19. The same 6.2-cm crystal fiber was used in this experiment. The planar output coupler has the same coating with the 4.4% spherical output coupler used in the previous section. The length of the collimated intra-cavity beam was chosen to be 3.8 cm, which is the minimum length

required for the insertion of the wavelength tuning elements.

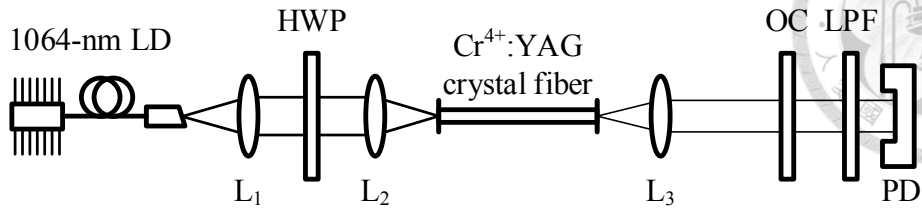


Fig. 4.19. Collimated ECCFL setup.

The laser slope efficiency was 13% and the pump threshold was 104 mW, as shown in Fig. 4.20. The laser output spectrum are shown in Fig. 4.21. The laser was free-running at 1452.1 nm and the laser linewidth was 0.4 nm. A numerical fitting of the experiment results gives an additional round-trip loss of 0.158 dB, compared with the hemispherical structure. Nevertheless, the collimated intra-cavity beam is still preferred for the tunable crystal fiber laser using a wavelength tuning element in the cavity.

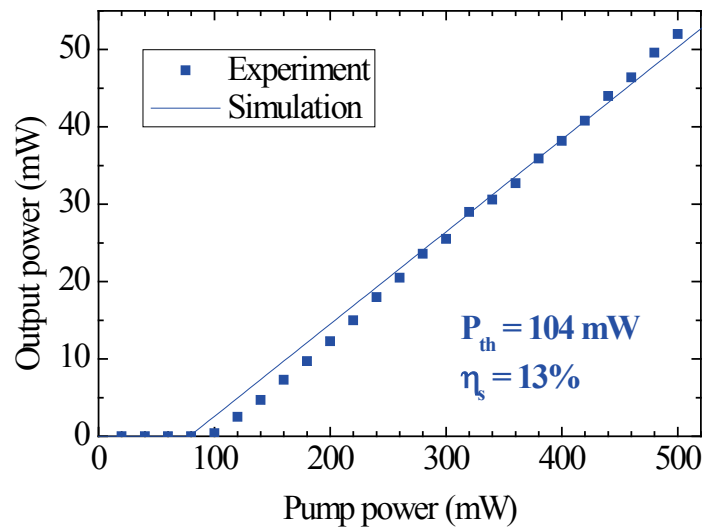


Fig. 4.20. Performance of collimated ECCFL.

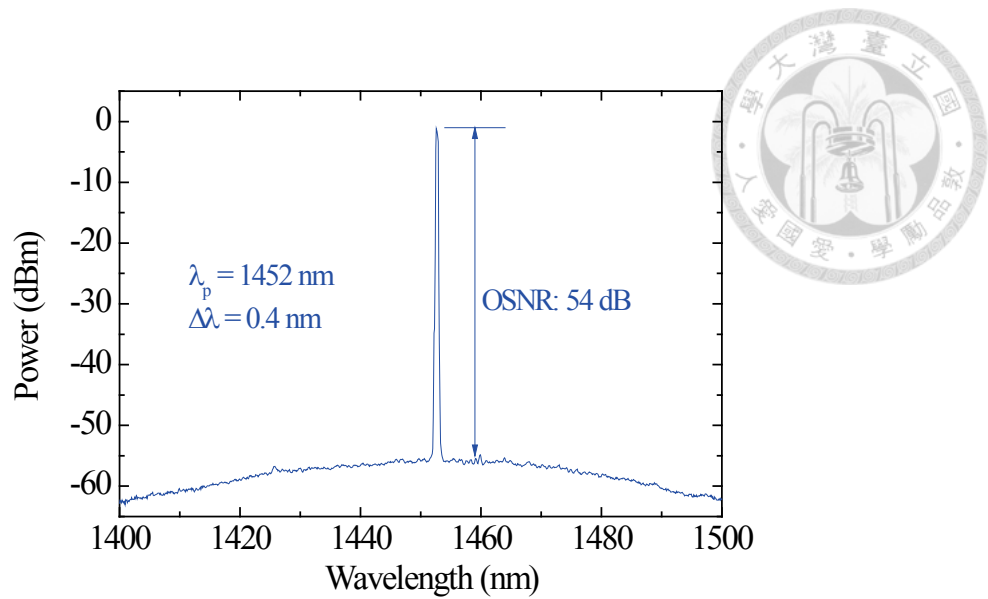


Fig. 4.21. Output spectrum of collimated ECCFL. The resolution bandwidth of the optical spectrum analyzer is 0.07 nm.

4.4 Broadly-Tunable Crystal Fiber Lasers

Broadly-tunable crystal fiber lasers were demonstrated with a pellicle beam splitter, a diffraction grating or a birefringent filter (BRF) as the tuning element. The diffraction grating was mounted in Littrow configuration, thus itself serves as an output coupler. The output coupler for the lasers tunable with a pellicle beam splitter or the BRF were replaced by HR mirrors in order to maximize the tuning range in the tunable laser experiments.

4.4.1 Wavelength Tuning with Uncoated Pellicle Etalon

The uncoated pellicle beam splitter (BP108, Thorlabs) is a nitrocellulose film with a refractive index about 1.50 and a thickness about 2 μm . When used as an etalon at wavelengths around 1.5 μm , the pellicle exhibits a free spectral range larger than 300 nm at normal incidence. However the modulation depth on the loss spectrum is small due to the low reflectance of the air/nitrocellulose interface. The transmission spectrum appeared in Fig. 4.22 was provided by the manufacturer. It is obvious that the s polarization is better than the p polarization for the tunable filter due to higher peak transmittance and larger modulation depth. The laser wavelength can be tuned by adjusting the tilt angle of the pellicle etalon in the laser cavity.

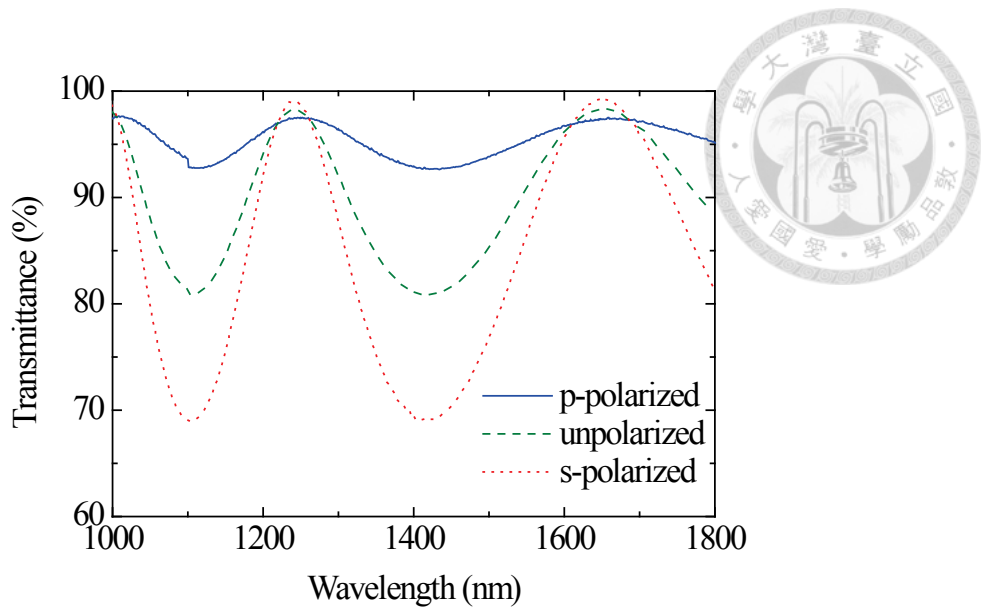


Fig. 4.22. Transmittance of Thorlabs BP108 uncoated pellicle beamsplitter with a 45° angle of incidence [60].

Both the hemispherical and the collimated cavities were used in this experiment. The output coupler used in the hemispherical ECCFL experiment was a broadband HR mirror with a radius of curvature of 50 mm. The experimental setup was shown in Fig. 4.23. The crystal fiber used in this experiment is 4.4 cm long and with a core diameter of $19 \mu\text{m}$. The crystal fiber was rotated so that the laser polarization was s-polarized with respect to the pellicle beam splitter. At some pellicle tilt angles there were multiple lasing peaks in the laser spectra, due to the small loss modulation of the pellicle. Discrete tuning from 1354 to 1476 nm was obtained, corresponding to a tuning range of 122 nm. The tuning was stepwise with respect to the pellicle tilt angle. One possible reason for the discrete tuning is the mismatch between the multimode crystal fiber modes and the free space resonator modes. The multimode interference could lead to periodic modulation in the cavity loss spectrum [61]. Similar discrete tuning curve is obtained by inserting the pellicle into the collimated ECCFL with a tuning range from 1368 to 1490 nm. The tuning curves for both cavities are shown in Fig. 4.24.

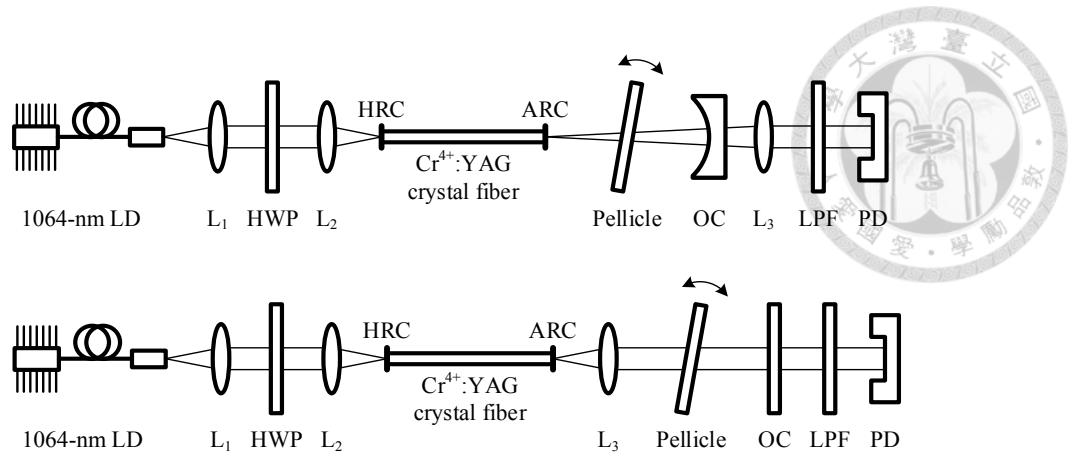


Fig. 4.23. Setups of tunable ECCFLs with uncoated pellicle beamsplitter. Upper: hemispherical cavity. Lower: collimated cavity.

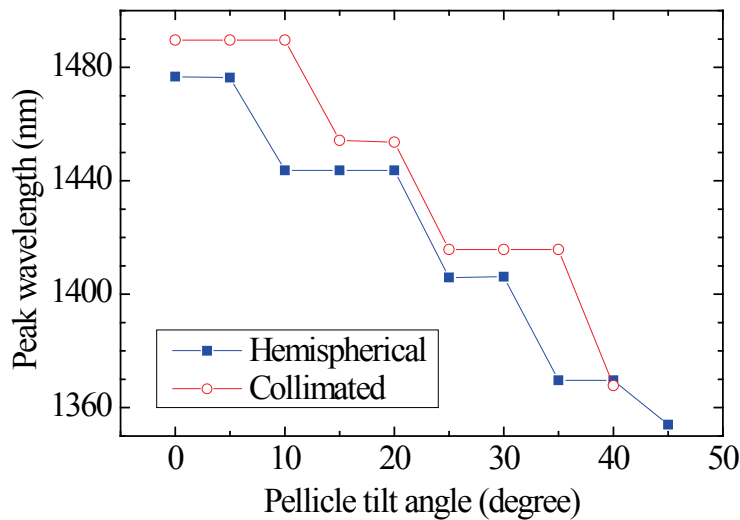


Fig. 4.24. Laser peak wavelengths vs. pellicle tilt angle in the hemispherical and the collimated ECCFLs.

4.4.2 Wavelength Tuning with Diffraction Grating

Contrary to the pellicle beam splitter, the diffraction grating provides excellent ability to reject the unwanted wavelength. The setup of the grating tunable crystal fiber laser is depicted in Fig. 4.25. The diffraction grating (53004BK02-246H, Richardson Gratings) used in this experiment is a planar holographic grating designed for use in the Littrow configuration, which means the -1^{st} order diffraction light goes back in the direction reversed to the incident light. The grating has 1050 grooves per mm and the area is 30×30 mm. The diffraction efficiency provided by the manufacturer is shown in Fig. 4.26. The diffraction efficiency is 96.9% at the wavelength of 1452 nm for TM

polarization.

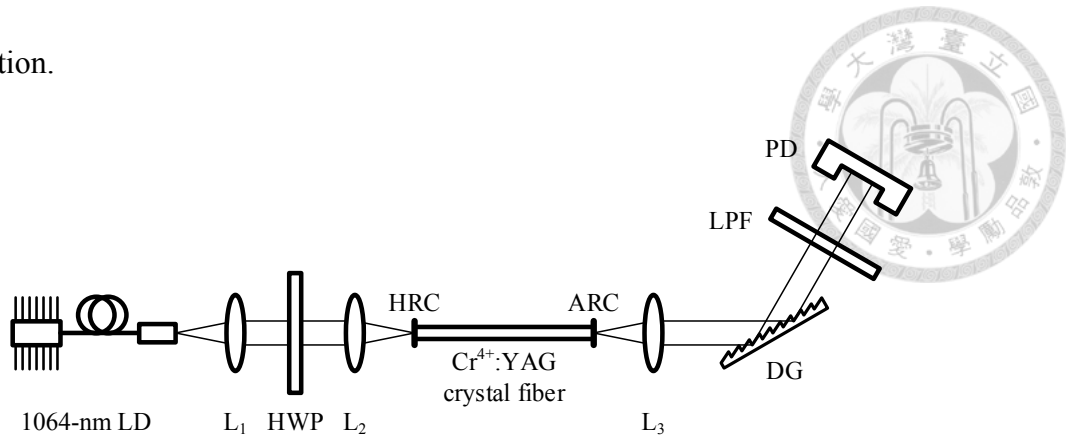


Fig. 4.25. Setup of the tunable ECCFL with a Littrow-mounted diffraction grating. DG: diffraction grating.

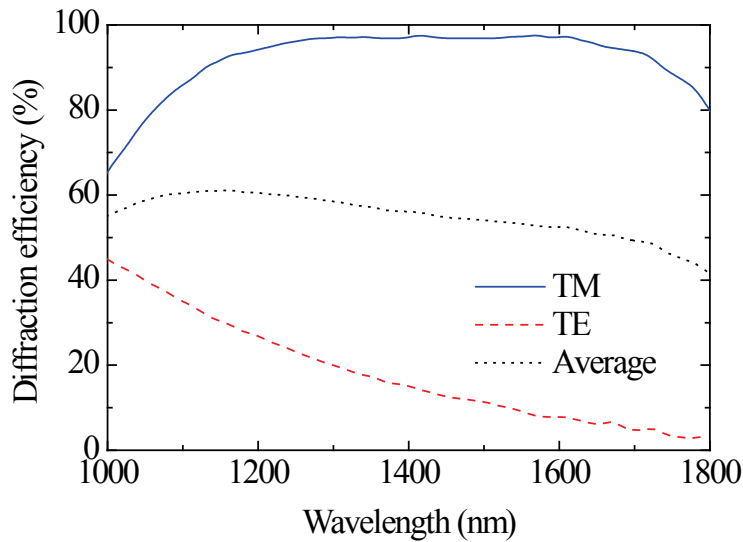


Fig. 4.26. Diffraction efficiency of the grating. Measured near the Littrow configuration.

The crystal fiber used in this experiment is the same 6.2-cm sample used in section 4.3. The crystal fiber was rotated so that the laser polarization was parallel to the optical table. The diffraction grating was mounted with its groove in the vertical direction, so that the intra-cavity laser beam was TM-polarized. The wavelength tuning was accomplished by rotating the grating in the table plane. The zero order diffraction of the grating was taken as the laser output. The direction of the output beam changed when the grating was rotated.

The measured output power at the peak wavelength of 1452 nm is shown in Fig. 4.27. The slope efficiency is 9.9% and the threshold pump power is 187 mW. The

wavelength tuning spectrum recorded with the “maximum hold” function of the optical spectrum analyzer is shown in Fig. 4.28. The laser was discretely tunable from 1399 nm to 1514 nm. The possible cause of the discrete tuning will be discussed in the next section.

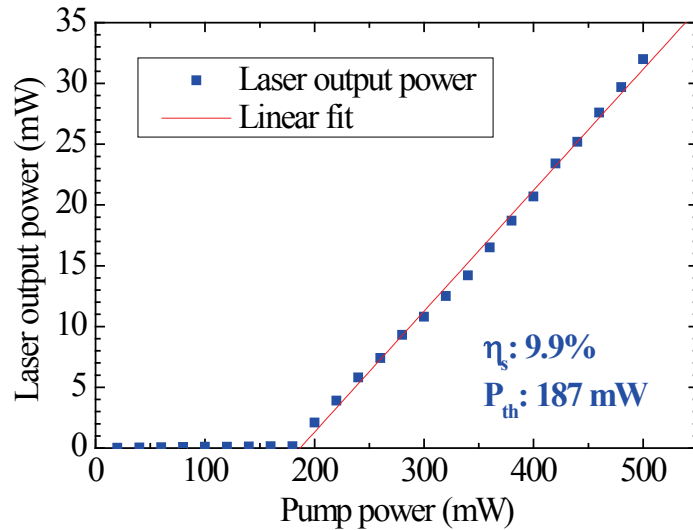
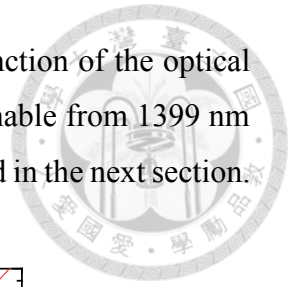


Fig. 4.27. Output power of the tunable ECCFL with a Littrow-mounted grating at the laser peak wavelength of 1452 nm.

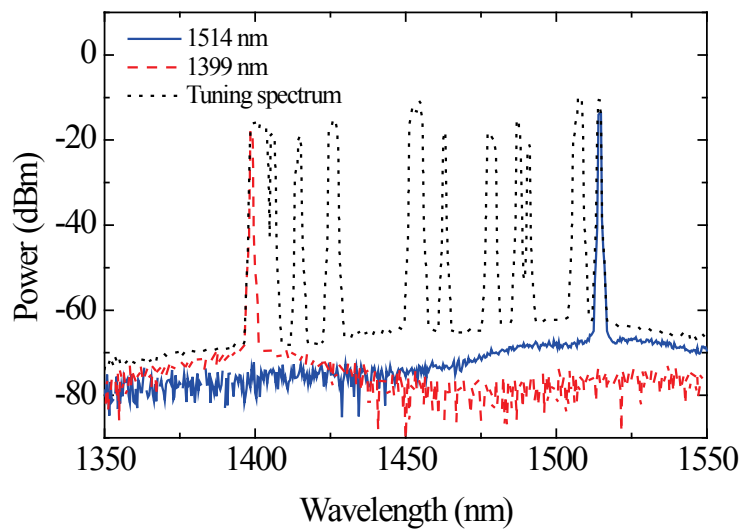


Fig. 4.28. The laser tuning spectrum and the laser output spectra at the two extreme wavelengths. The laser tuning spectrum was recorded using the “maximum hold” function of the optical spectrum analyzer while rotating the diffraction grating.

4.4.3 Wavelength Tuning with Birefringent Filter

BRFs have been extensively used in broadband tunable solid-state and dye lasers due to their broad tuning range and low insertion loss [62]. A BRF made of single-plate quartz was designed for tuning the laser. The BRF has a thickness of 888 μm and the optic axis lies in the plate plane. The calculated single-pass p-polarized transmittance of the BRF is shown in the background of Fig. 4.30. The crystal fiber used in this experiment is 4.4-cm long and with a core diameter of 19 μm . The crystal fiber was rotated so the laser polarization is in the TM direction of the BRF. No laser operation was observed after inserting the BRF into the hemispherical ECCFL, because the Brewster-oriented BRF introduces large aberration loss for the intra-cavity divergent beam.

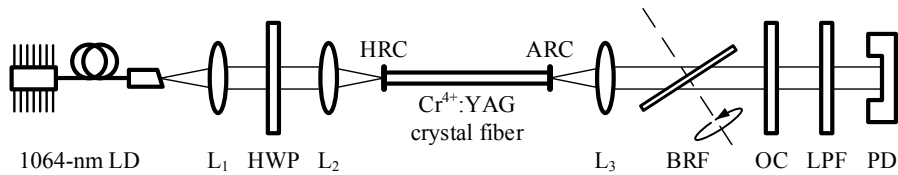


Fig. 4.29. Setup of the tunable ECCFL with a birefringent filter.

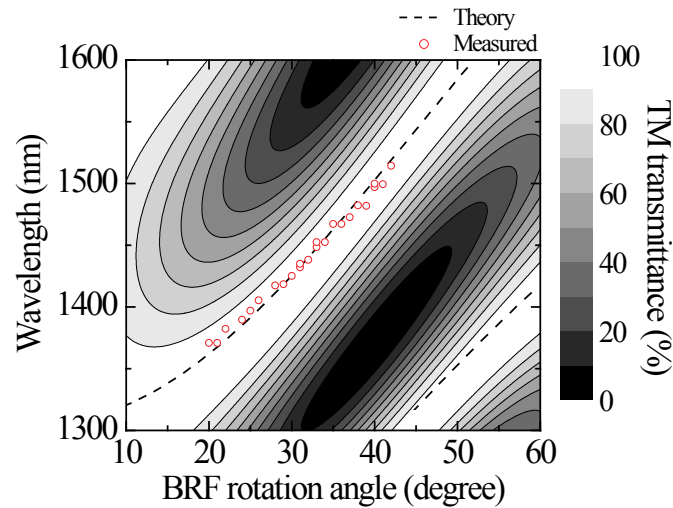


Fig. 4.30. Laser wavelength vs. the rotation angle of the BRF. Dashed line: Theoretical tuning curves of the BRF. Dots: Measured laser wavelengths. Background contours: Single-pass p-polarized transmittance of the BRF.

Tunable laser was successfully demonstrated with the insertion of the BRF into the collimated ECCFL. The laser wavelengths vs. the in-plane rotation angle of the BRF is plotted as the dots in Fig. 4.30 and the tuning spectrum is shown in Fig. 4.31. The length

of the collimated beam is about 3.8 cm. The wavelength tuning was accomplished only by rotating the BRF, without re-aligning the laser cavity. The tuning was from 1353 to 1509 nm, corresponding to a tuning range of 156 nm. The lowest threshold pump power was 70 mW at the peak wavelength of 1452 nm. The tuning was also discrete but with denser lasing peaks in the tuning spectrum, as a consequence of better wavelength selectivity of the BRF than that of the pellicle etalon due to the larger modulation depth in the loss spectrum.

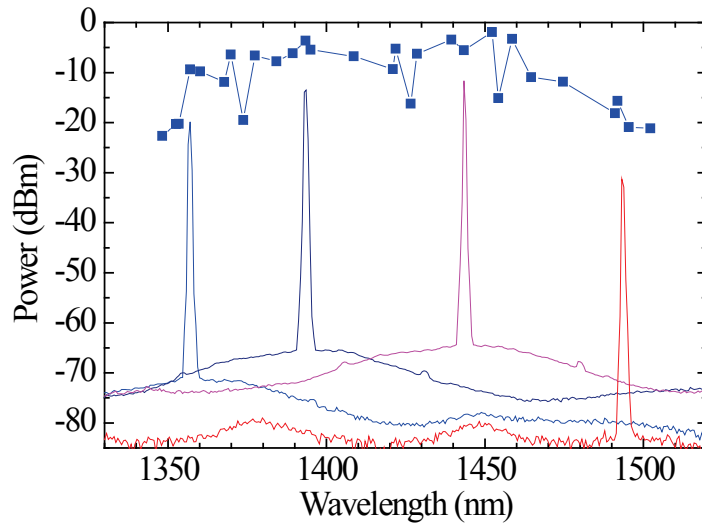


Fig. 4.31. Dots: The laser output power vs. laser output wavelengths under 400-mW pump power. Lines: four example spectra lasing at 1357, 1393, 1443, and 1494 nm. The OSA resolution bandwidth is 1 nm.

To investigate the relations between discrete tuning and the multimode nature of the crystal fiber, we recorded the output beam profile of the tunable collimated ECCFL with an infrared charge-coupled device (CCD) (CamIR¹⁵⁵⁰, Applied Scintillation Technologies). This infrared image sensor is a silicon CCD coated with up-conversion phosphors with the responsive wavelength range from 1460 to 1600 nm. However the distribution of the phosphors is quite nonuniform. To remove this nonuniformity, we recorded multiple images of the laser beam by moving the CCD in the transverse direction using a one-axis linear stage. All images were then re-aligned and averaged. Figure 4.32 shows the recorded beam profile when the wavelength was at 1477 nm, which was an averaged result from 71 images with a 30- μ m interval in the x direction.

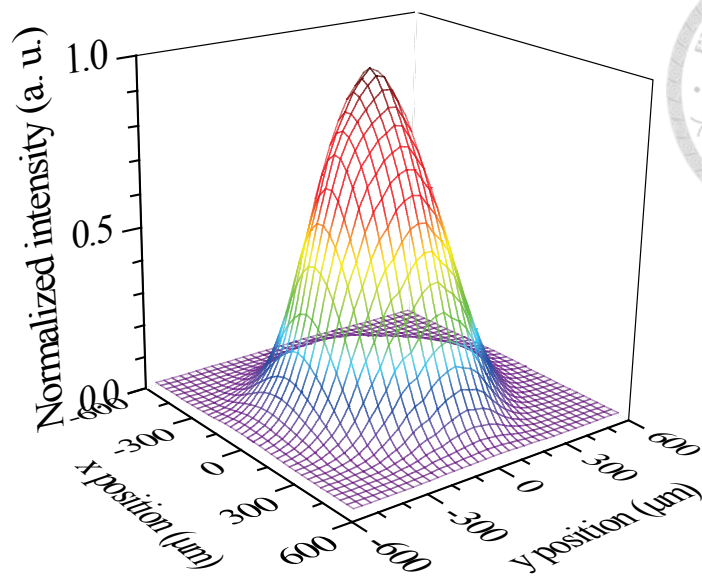


Fig. 4.32. Output beam profile at the laser wavelength of 1477 nm

During the wavelength tuning operation, the intensity pattern of the output beam changed abruptly whenever the laser wavelengths jumped. Adding an iris at the collimated part in the cavity as a spatial filter to select the fundamental mode did not work because the modal size discrimination between the fundamental and the higher order transverse modes may not be large enough. As a result, a combination of multiple transverse modes with the lowest round trip loss were selected by the laser oscillation. This combination could be very sensitive to the wavelength due to different phase velocity of each mode. Thus when the tuning element is adjusted, the laser seeks the next combination of modes with the lowest loss, which corresponds to a specific wavelength. One solution for the discrete tuning problem is to develop a single-mode crystal fiber by using high-index cladding materials, such as high-index glasses or YAG ceramics. We will introduce the design and fabrication of YAG crystal fibers cladded with high-index glasses in chapter 5.

4.5 Design of Cr⁴⁺:YAG Crystal Fiber Amplifiers

In addition to the application in the broadband tunable laser, the Cr⁴⁺:YAG crystal fiber is also an attractive candidate as an optical amplifier providing broadband gain over the entire communication wavelengths. In this section, we evaluate the performance of a Cr⁴⁺:YAG crystal fiber amplifier with numerical simulation. The propagation losses of the crystal fiber are fixed at the fitted values in previous sections. Because the emission

cross sections and the fluorescence lifetimes are known to be dependent on the core diameter, in the following simulations the core diameter is also fixed at $17\ \mu\text{m}$, which is the core size of the sample used in the numerical fitting.

The numerical simulation of the optical amplifier is quite similar to the laser. In ideal cases, we assume all interfaces are lossless. Here we compare three different designs of the crystal fiber amplifier: the single-pump and single-pass (SPSP) scheme, the single-pump and double-pass (SPDP) scheme, and the dual-pump and double-pass (DPDP) scheme. Illustrations of these schemes are shown in Fig. 4.33. In the SPSP scheme, the signal light and the pump light are coupled into the crystal fiber from the same end face, and the output signal is detected at the opposite end. A wavelength-division multiplexer or a dichroic mirror is required for combining the pump light and the signal light. In the SPDP scheme, the signal light is reflected at the opposite end so the signal pass through the gain medium twice. This approach can effectively double the gain at the expense of more complicated structures. An optical circulator is required to separate the input signal and the output signal. The pump light can also be reflected to enhance the pump power utilization. The DPDP scheme is similar to the SPDP scheme, but with the incident pump coupled into the crystal fiber from both ends. The signal reflector in the DPDP scheme must be designed to have high transmittance for pump. The ratio between the forward and backward pump in the DPDP scheme is fixed at 1:1 in the following discussion.

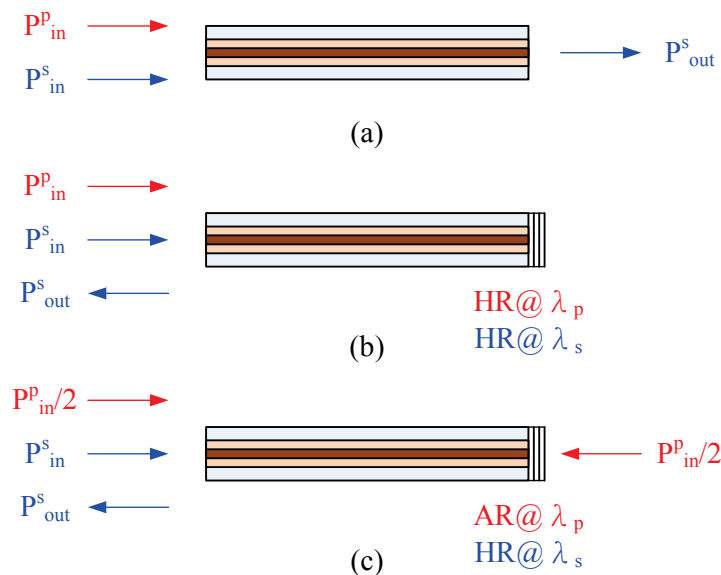


Fig. 4.33. Schematic plots of different $\text{Cr}^{4+}:\text{YAG}$ crystal fiber amplifier schemes. (a) SPSP; (b) SPDP; (c) DPDP.

Simulations were carried out for comparing these three schemes. The wavelengths of pump and signal are 1064 nm and 1431 nm, respectively. The input signal power is -30 dBm and the fiber length is 20 cm. The simulation result is shown in Fig. 4.34. The DPDP scheme provides the highest optical gain. The SPDP scheme can achieve similar performance when crystal fiber is well saturated by the pump power. The DPDP scheme can offer higher gain than the SPDP scheme due to a more uniform population inversion over the entire crystal fiber, as shown in Fig. 4.35, which shows the excited state population under 1-watt pump. For the single-pump schemes, the excited state population decays to < 10% of the total concentration at the tail of the crystal fiber, because the pump is almost fully absorbed. The double-pump scheme has a more uniform population distribution and the lowest excited-state population is 72% of the total concentration.

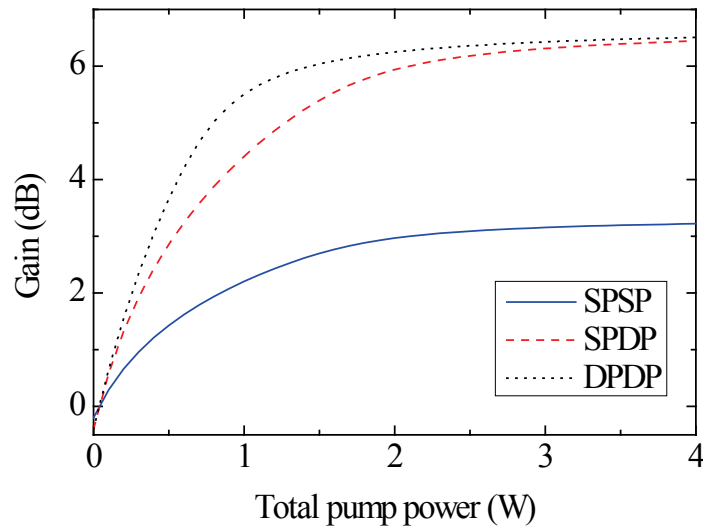


Fig. 4.34. Performance of different schemes of the Cr⁴⁺:YAG crystal fiber amplifier. The input signal power is -30 dBm and the fiber length is 10 cm.

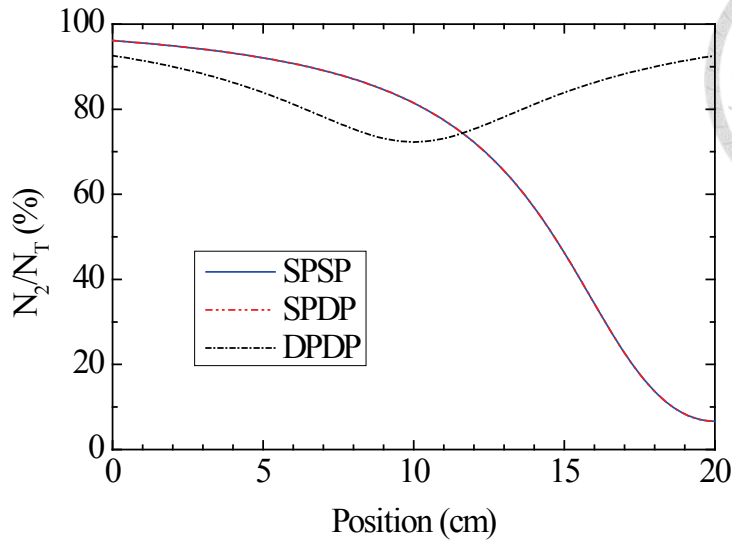


Fig. 4.35. Excited state population of different schemes of Cr^{4+} :YAG crystal fiber amplifiers. The pump power is 1 watt and the crystal fiber length is 20 cm. The lines of the SPSP and the SPDP schemes are very close.

Assuming complete inversion, the small-signal gain constant will be $N_T \times \sigma_e (1 - f_L)$, which is about 0.4 dB/cm. Since the 0.01-dB/cm propagation loss is much lower than the small-signal gain, the optical gain can be enhanced by increasing the fiber length and the pump power without introducing too much loss. However, the fabrication yield rate is higher for shorter crystal fibers. Increasing the doping concentration can effectively reduce the required length for achieving the same optical gain. The Cr^{4+} concentration in the Cr^{4+} :YAG crystal fiber drops after each LHPG growth [57]. The small-signal pump absorption coefficient at 1064 nm, α_{p0} , is 4.5 cm^{-1} for the source crystal and 0.75 cm^{-1} for the double-clad crystal fiber, which means the Cr^{4+} concentration drops to 1/6 of its original value. The Cr^{4+} concentration can be increased by depositing a layer of Cr_2O_3 together with a layer CaO or MgO onto the source rod before the LHPG growth [63]. Here we assume that the Cr^{4+} concentration of the crystal fiber can be recovered to the level of the source crystal with side deposition method without affecting the optical qualities of the crystal fiber. The optical gain of crystal fibers with absorption coefficients of 0.75 cm^{-1} and 4.5 cm^{-1} under a total pump power of 10 W and 1 W are plotted in Fig. 4.36. The maximum gain is 17.1 dB at 60 cm for crystal fibers with $\alpha_{p0} = 0.75 \text{ cm}^{-1}$, and 17.7 dB at 10 cm for crystal fiber with $\alpha_{p0} = 4.5 \text{ cm}^{-1}$. Enhancing the concentration by 6 times results in a 6-fold reduction of the optimized length. The

constant decay after the optimized length is due to the 0.01-dB/cm signal propagation loss.

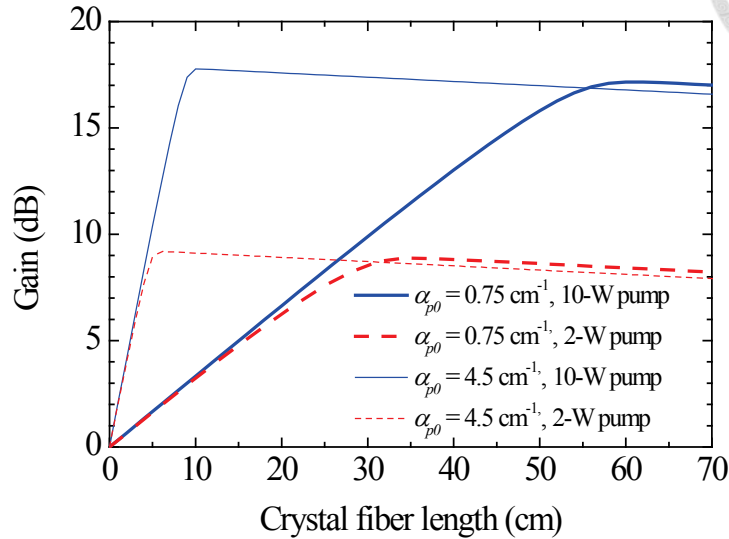


Fig. 4.36. Simulated optical gain versus the length of Cr^{4+} :YAG crystal fibers with different Cr^{4+} concentrations under 10-W and 2-W pumping in the DPDP scheme.

Since enhancing the Cr^{4+} concentration can greatly reduce the required crystal fiber length, we focus on the use of high-concentration crystal fiber with an α_{p0} of 4.5 cm^{-1} with the DPDP scheme in the following analysis. The simulated optical gain of a 10-cm long crystal fiber versus the pump power is shown in Fig. 4.37. The small-signal gains are 22.7 dB and 19.4 dB under the pump powers of 20 W and 10 W, respectively. For the input signal power ranging from -30 dBm to -10 dBm, the gain curves are almost identical.

The optical gain versus the input signal power is plotted in Fig. 4.38. The input signal saturation powers at which the gains drop 3 dB are 12.6 dBm, 9.2 dBm, and 8.6 dBm at the pump power of 5 W, 10 W, and 20 W, respectively. These signal saturation powers are much higher than the rare-earth doped fiber amplifiers, because the fluorescence lifetime of Cr^{4+} :YAG is very short compared to those materials. However, the required pump power for saturating the Cr^{4+} :YAG crystal fiber is also much higher as a trade off.

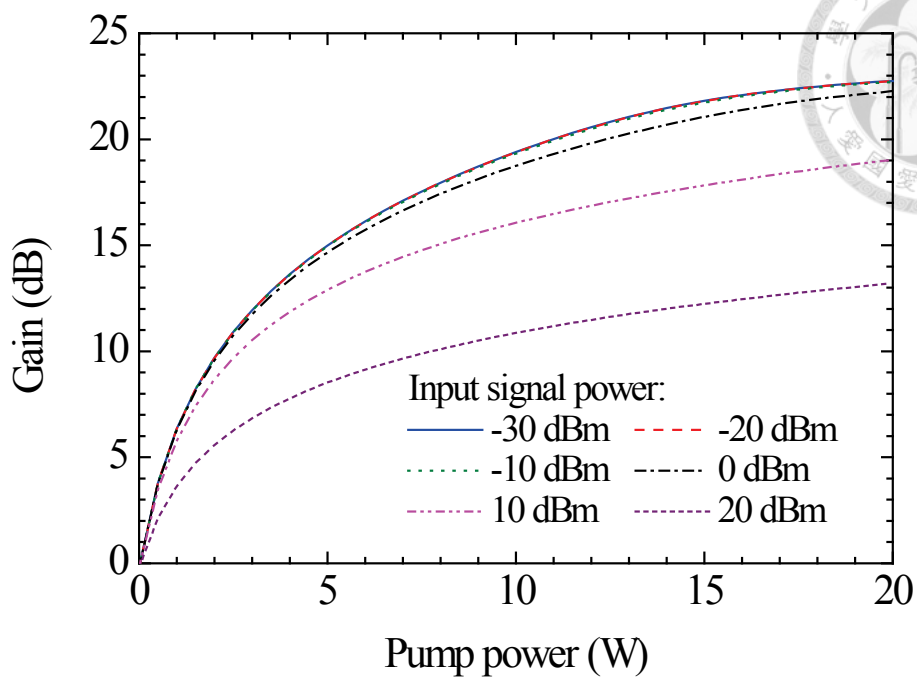


Fig. 4.37. Simulated optical gain versus total pump power under different input signal power. The length of the crystal fiber is 20 cm. The lines with the input signal from -30 dBm to -10 dBm are very close to each other.

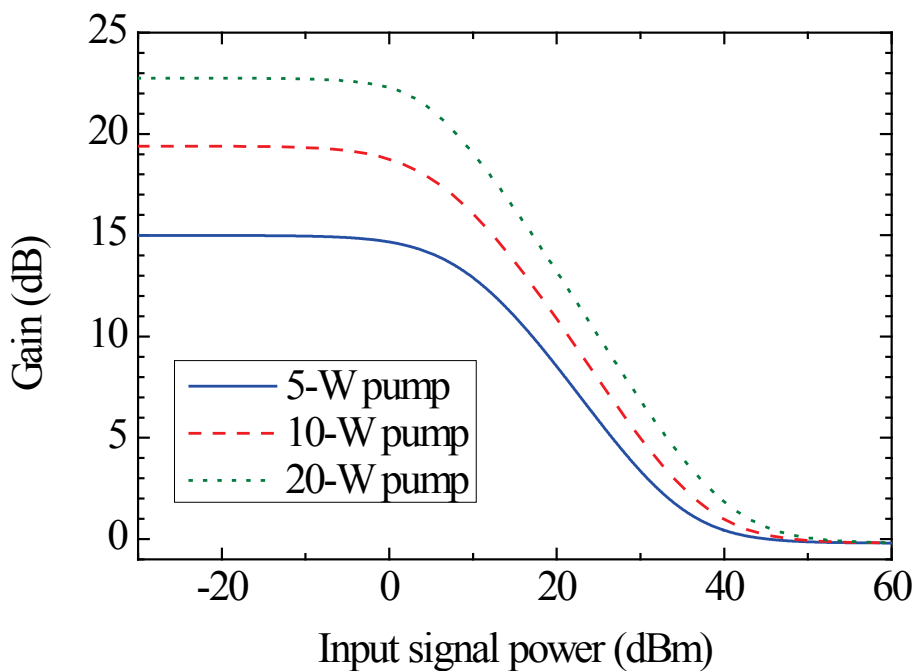


Fig. 4.38. Gain versus the input signal level for a 10-cm long crystal fiber.

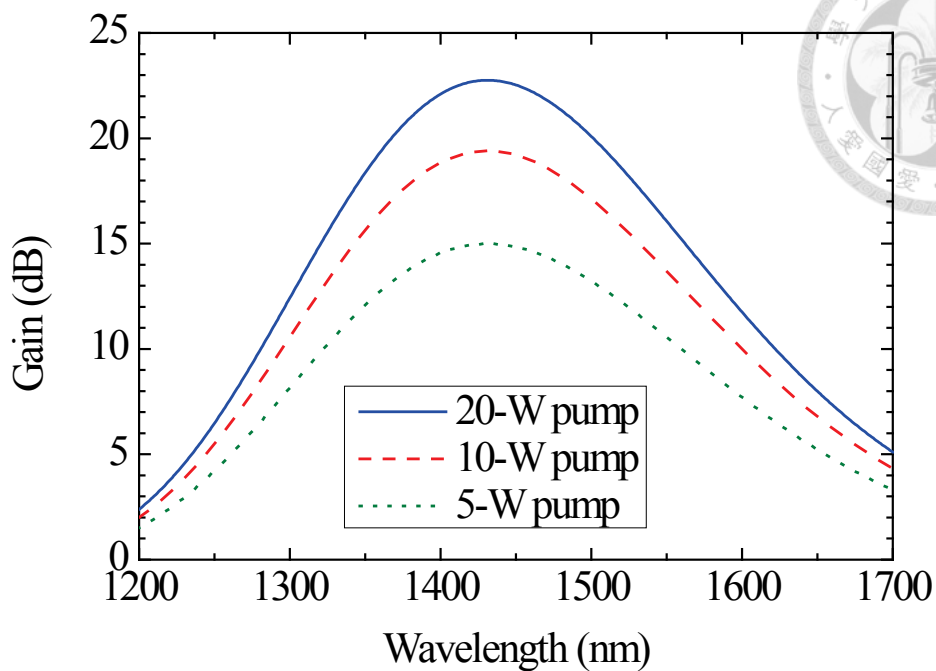
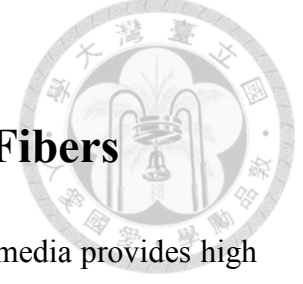


Fig. 4.39. Small-signal gain spectra of a 10-cm long Cr⁴⁺:YAG crystal fiber under different pump powers.

The small-signal gain spectra of a 10-cm long crystal fiber with different pump powers are shown in Fig. 4.39. It was assumed that the f_L and the propagation losses are independent of the wavelength. The 3-dB bandwidths are 175, 152, and 139 nm under the total pump powers of 5 W, 10 W, and 20 W, respectively. This amplifier can provide >10-dB gain from 1281 nm to 1622 nm under a 20-W pumping power. This spectral range matches very well to the O-E-S-C-L band (1260 to 1625 nm). This amplifier has great potential for the future broadband optical communication systems.

Chapter 5

Toward Single-Mode YAG Crystal Fibers



A laser with a single-transverse-mode crystal fiber as the gain media provides high beam quality and good pointing stability. A single-mode crystal fiber can also enhance the tuning characteristics when used in a tunable laser, due to the suppression of the multimode interference effect. To develop a single-mode YAG crystal fiber, the refractive index of the cladding material must be very close to that of YAG. Reduction of the index difference between the core and the cladding also reduces the propagation loss [24]. Options of the cladding materials include the YAG ceramics or the high-refractive-index glasses. In this chapter, we focus on the design and the fabrication of the high-index-glass-clad (HIGC) YAG crystal fibers. N-SF57-clad and N-LaSF9-clad YAG crystal fibers were fabricated and characterized by measuring the near-field mode profile and the far-field intensity distribution. The design of the single-mode HIGC Cr⁴⁺:YAG crystal fiber is also discussed.

5.1 Tuning Glass Refractive Index with Annealing Treatment

From the Scott glass catalogue [64], 4 types of glasses with refractive indices close to YAG in the near infrared were chosen as the candidates of the cladding material, namely N-LaSF9, N-LaSF41, SF57, and N-SF57. The dispersion curves $n(\lambda)$ can be calculated with the Sellmeier equation [65]:

$$n^2(\lambda) - 1 = \frac{B_1\lambda^2}{(\lambda^2 - C_1)} + \frac{B_2\lambda^2}{(\lambda^2 - C_2)} + \frac{B_3\lambda^2}{(\lambda^2 - C_3)} \quad (5.1)$$

where $B_{1,2,3}$ and $C_{1,2,3}$ are the Sellmeier constants, and λ is in unit of μm . The Sellmeier constants of YAG [66] and the high-index glasses [67] are listed in Table 5.1. The dispersion curves in the wavelength range of 400 to 1800 nm are plotted in Fig. 5.1.

Table 5.1. List of Sellmeier constants of YAG and high-index glasses.

	B ₁	B ₂	B ₃	C ₁	C ₂	C ₃
YAG	2.282	3.27644	-	0.01185	282.734	-
N-LaSF9	2.00029547	0.298926886	1.80691843	0.0121426017	0.0538736236	156.530829
N-LaSF41	1.86348331	0.413307255	1.35784815	0.00910368219	0.0339247268	93.3580595
SF57	1.81651371	0.428893641	1.07186278	0.0143704198	0.0592801172	121.419942
N-SF57	1.98550331	0.274057042	1.28945661	0.0141749518	0.0640509927	177.389795

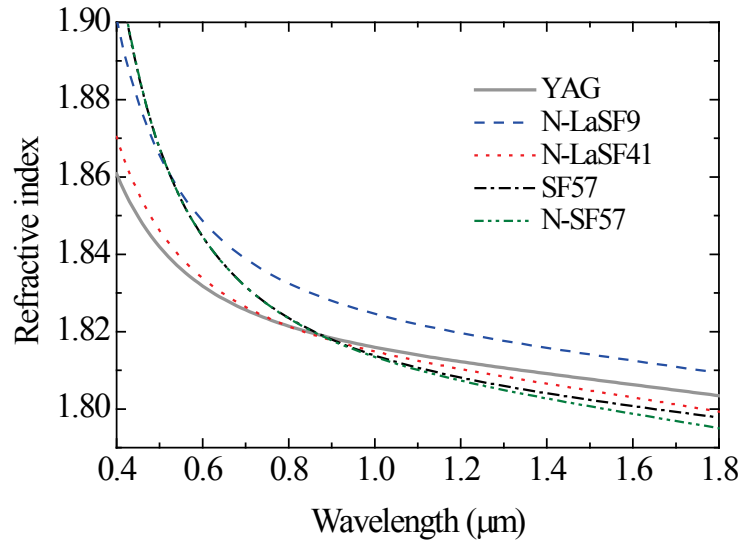


Fig. 5.1. Dispersion curves of YAG and 4 types of high-index glasses from 0.4 to 1.8 μm .

The refractive index of a glass can be tuned by varying the annealing rate from T_g to $T_g - 120^\circ\text{C}$, where T_g is the glass transition temperature. The change of the refractive index at the wavelength of 589.3 nm, Δn_d , is related to the annealing rate as [68]:

$$\Delta n_d = m_{nd} \cdot \log\left(\frac{h_x}{h_0}\right) \quad (5.2)$$

where h_0 is the reference annealing rate, and h_x is the new annealing rate. m_{nd} is the annealing coefficient of the refractive index. The typical reference annealing rate of Schott is 7°C/hr . The glass transition temperatures, glass softening temperatures (T_s), and

the annealing coefficients of the high-index glasses are listed in Table 5.2, and the refractive index variations versus the annealing rates are plotted in Fig. 5.2.

Table 5.2. The transition temperatures, the softening temperatures, and the annealing coefficients of the high-index glasses.

	T_g (°C)	T_s (°C)	m_{nd}
N-LaSF9	683	817	-0.00175
N-LaSF41	651	739	-0.00157
SF57	414	519	-0.00053
N-SF57	629	716	-0.00263

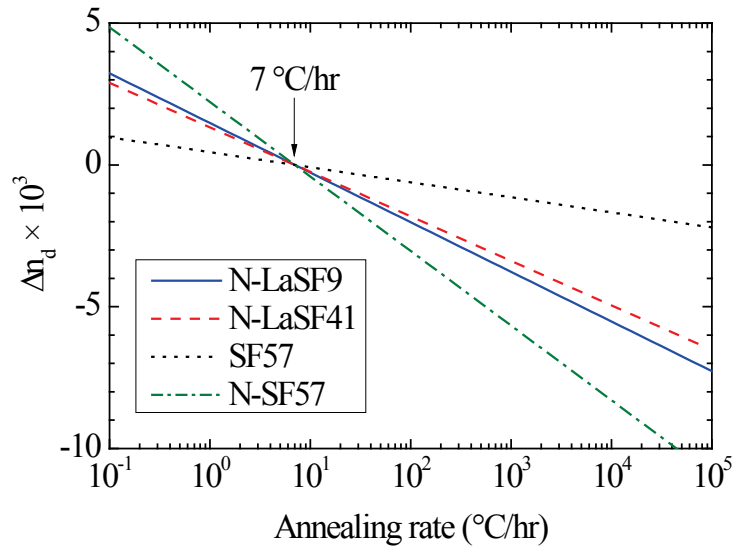


Fig. 5.2. The changes of refractive indices of several glass types as functions of the annealing rate.

5.2 Characteristics of High-Index-Glass-Clad Crystal Fibers

The number of optical modes depends on the normalized frequency, V , of the optical fiber, which is defined as:

$$V = \frac{2\pi a}{\lambda} \sqrt{n_1^2(\lambda) - n_2^2(\lambda)} \quad (5.3)$$

where $n_1(\lambda)$ and $n_2(\lambda)$ are the refractive indices of the core and the cladding at the wavelength of λ , respectively. a is the fiber core radius.

The number of linearly-polarized (LP) modes per one polarization is plotted in Fig. 5.3. For a fiber to be single-mode, V must be less than 2.405. Here we define the few-

mode fiber as the fiber with a mode number less than 10 per one polarization, since we did not find any explicit definition of the few-mode fiber in literature. With this definition, we can find from Fig. 5.3 that V is less than 5.520 for a few-mode fiber.

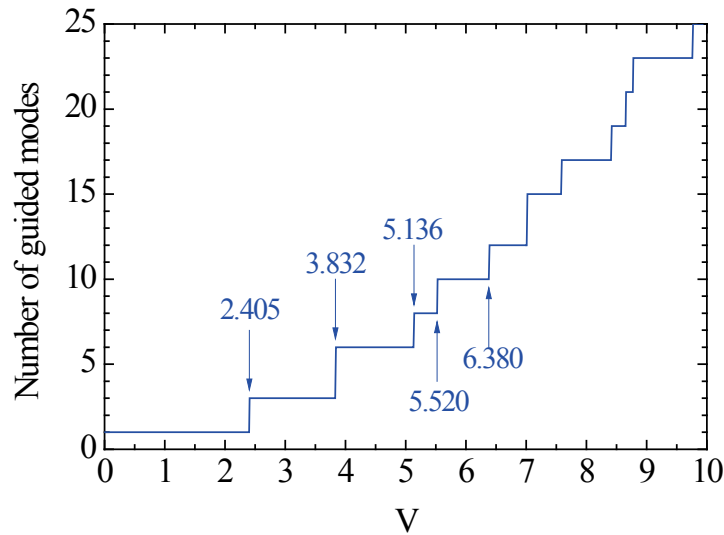


Fig. 5.3. Number of LP modes of an optical fiber per one polarization [48].

For typical optical fibers with similar composition in the core and in the cladding, a specific mode (except for the fundamental mode) will cease to exist when the wavelength is longer than the cut-off wavelength. This is because of that the index difference of a typical fiber is almost independent of the wavelength, thus the V value decays with the increasing wavelength. However, for an HIGC crystal fiber, it is more often to see the “cut-on” behavior, that is, a specific mode starts to exist beyond a certain wavelength.

For example, the $V - \lambda$ curve of an N-LaSF41-clad YAG crystal fiber with a 20- μm core diameter is plotted in Fig. 5.4. The cladding index is assumed to the same with its bulk value. Due to the cross-over between the dispersion curves of core and cladding (see Fig. 5.1), the fundamental mode has a cut-on wavelength at 793 nm. The V value rises rapidly after the cut-on of the fundamental mode, and exceeds 2.405 at 837 nm, which is the cut-on wavelength of the first higher order mode. Therefore, the wavelength range of single-mode operation with this crystal fiber is only from 793 nm to 837 nm. If broader single-mode bandwidth is desired, the most efficient way is to reduce the core diameter.

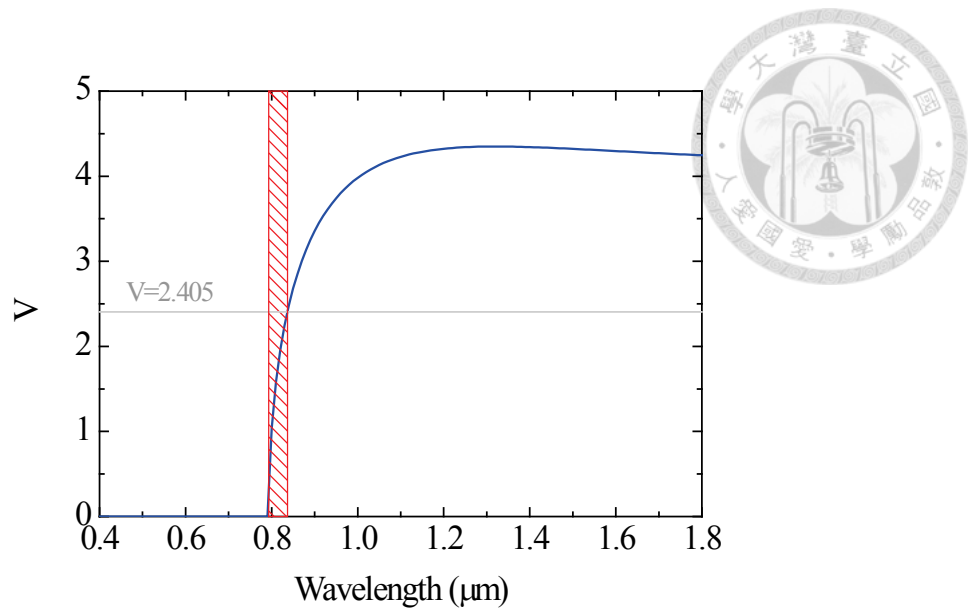


Fig. 5.4. The V value of an N-LaSF41-clad crystal fiber with a core diameter of 20 μm . The cladding index was assumed to be the bulk index. The shaded region indicates the wavelength range of single-mode operation.

5.3 Measuring the Guiding Properties of High-Index-Glass-Clad Crystal Fibers

5.3.1 Refractive Index Profiling

The optical fiber index-profiling techniques include the reflectance mapping methods [24], [69], [70], the refracted near-field methods [71], and the interferometric methods [72]–[74].

In the reflectance mapping methods, the reflectance of the fiber end face is mapped with a laser scanning microscope. The refractive index profile is then deduced from the reflectance profile with the Fresnel reflection equation. The spatial resolution is determined by the focal spot size. The flatness of the end face is critical for this technique. A crystal fiber cannot be cleaved since the core and the cladding are made of different materials. Therefore, polishing is necessary for achieving an optically flat surface. However, the reflectance of polished glass surfaces may change significantly due to the polishing-induced surface layer [75]–[78]. Meanwhile, in our experiences, the reflectance of the YAG crystal does not change much after polishing. Therefore, the reflectance of a polished glass-clad crystal fiber end face cannot be correctly mapped, due to different extent of the polishing-induced reflectance change in the core and the cladding region.

The refracted near-field methods and the interferometric methods all require immersing the test fiber into the fluids with the refractive index matching to that of the cladding. The n_d is 1.8328 for YAG crystal and even higher for the 4 types of high index glasses. However, the highest n_d of the non-toxic commercial index-matching fluids is only 1.81 (19160, Cargille Labs). Imperfect match of the immersion fluid index and the cladding index will result in large error for the refracted near-field methods [79] and reduced sensitivity for the interferometric methods [80].

To summarize, it is hard to obtain an accurate index profile for a YAG crystal fiber cladded with high-index glass, due to the polishing-induced reflectance change in the glass cladding and the lack of the index matching fluids.

5.3.2 Near-Field Mode Imaging

The core modes of the HIGC crystal fibers are imaged with the system illustrated in Fig. 5.5. An SMF28e patch cord was used as the input fiber of the system. The input wavelength could be changed simply by connecting the input fiber to a different fiber-pigtailed light source. Four fiber-pigtailed lasers with wavelengths of 532, 658, 780, and 1064 nm were used as the light sources. The light was collimated and focused by a pair of near-infrared objective lenses (M Plan APO NIR 5X, Mitsutoyo). These objective lenses are chromatically corrected from visible to NIR, and there is no apparent focal shift for wavelengths up to 1100 nm. The light reflected from the crystal fiber input end face was split by a broadband beam splitter for observation with naked eye. The light output from the crystal fiber was imaged on a charge-coupled device (CCD) with an aspherical lens with $f = 14$ mm and $NA = 0.16$ (5726-B-H, New Focus).

During the experiment, the coupling into the crystal fiber was optimized at the visible wavelengths. When switching to infrared wavelengths, there was no need to re-align the crystal fiber due to the good chromatic correction of the objective lenses. However, the imaging system after the crystal fiber needs to be re-focused since the aspheric lens has strong dispersion.

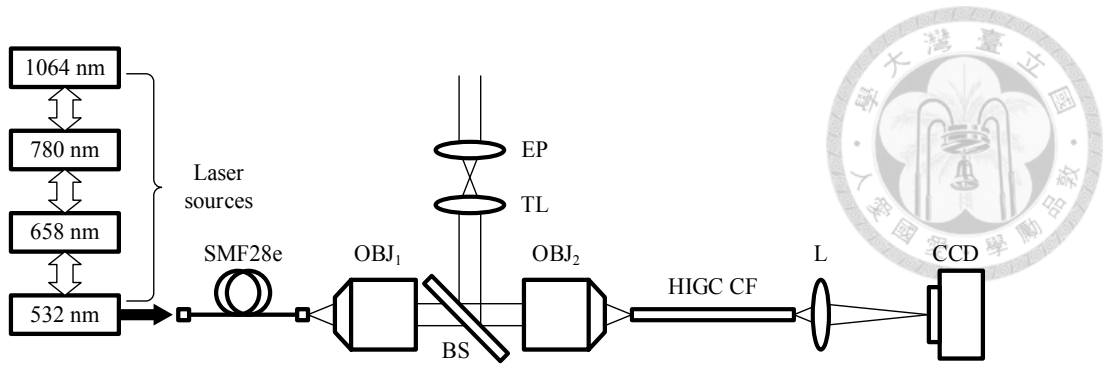


Fig. 5.5. Experimental setup for imaging the modes of the HIGC crystal fiber. OBJ₁ and OBJ₂: objective lenses; BS: beam splitter; TL: tube lens; EP: eye piece; CF: crystal fiber; L: aspheric lens; CCD: charge-coupled device.

5.3.3 Far-Field Intensity Distribution

The setup for measuring the far-field distribution is depicted in Fig. 5.6. The light output from the crystal fiber was directly captured by the CCD without imaging with a lens.

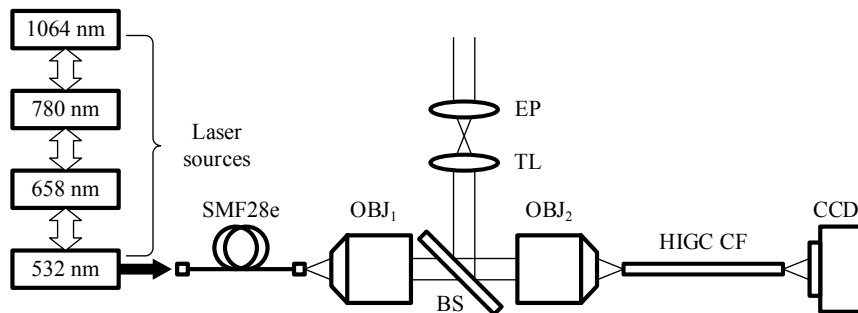


Fig. 5.6. Experimental setup of measuring the far-field distribution of the HIGC crystal fiber.

The reason of measuring the far-field distribution is to clarify that whether the fiber was guided or not. In an unguided fiber, a ray launched into core will be split into reflected ray and transmitted ray when hitting the core-cladding interface, as depicted in Fig. 5.7.

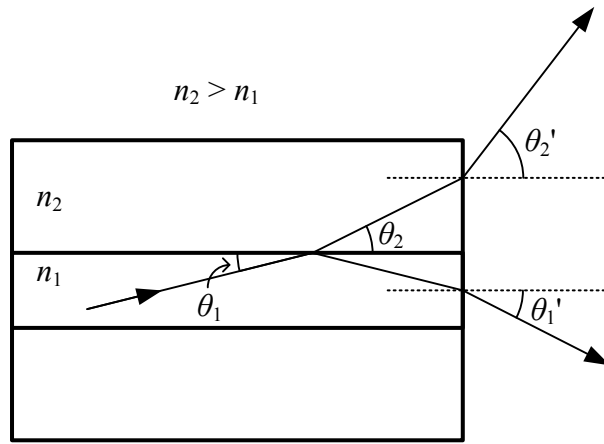


Fig. 5.7. Schematic illustration of the rays propagate in and output from an unguided crystal fiber.

The transmitted light will be refracted so that the propagation angle with respect to the fiber axis becomes larger. If the transmitted rays hit the core-cladding interface again, part of the power will be transmitted back into the core. For the rays leave from the cladding region of the crystal fiber, the exit angle θ'_2 can be described as:

$$\sin \theta'_2 = \sqrt{n_2^2 - n_1^2 \cos^2 \theta_1} \quad (5.4)$$

where n_1 is the ray propagation angle with respect to the fiber axis inside the core, and n_1 and n_2 are the refractive indices of the core the cladding, respectively. This angle has a minimum value of

$$\sin \theta'_{2_min} = \sqrt{n_2^2 - n_1^2} \quad (5.5)$$

Although some of the light was output from the core region, but the relative intensity will be small if the fiber is long enough. Therefore, the output light will exhibit as a cone with a minimum angle of θ'_{2_min} . The intensity pattern captured by the CCD will be a bright ring with a relatively dark inner region.

No ring pattern will be observed if the crystal fiber is guided or if the ray is launched into the crystal fiber at the cladding region. Thus the observation of the ring pattern is a deterministic proof that the crystal fiber is unguided. The refractive index difference between the core and the cladding can also be deduced from (5.5) by measuring the angle of the inner edge of the light cone.

5.4 High-Index-Glass-Clad Pure YAG Crystal Fibers

5.4.1 Few-Mode N-SF57-Clad YAG Crystal Fiber

In previous works [81], the YAG crystals has been prepared with the N-SF57 capillaries. The N-SF57 capillaries were fabricated by Schott for the development of the HIGC crystal fibers. Pure YAG single-crystal fibers with 40- μm diameters were grown by the LHPG method described in section 3.1.2. As listed in Table 5.2, the softening points of the high-index glasses are much lower than the melting point of YAG, which is 1970 °C. Therefore, the high-index glass cladding process is the similar to the Pyrex cladding process described in section 3.1.4.

In order to estimate the upper limit of the cooling rate of the LHPG process, the cooling rate was calculated with extreme assumptions. The Rayleigh range of the CO₂ laser focus in the growth chamber is 46 μm . With a growth speed of 3 mm/min, the time required for passing through the Rayleigh range of the CO₂ laser is 0.93 second. If the cladding temperature drops from the transition temperature, which is 519 °C for N-SF57, to the room temperature of 20 °C in 0.93 second, then the cooling rate will be about 2×10^6 °C/hr.

The as-grown N-SF57-clad crystal fiber were measured with the mode imaging methods, and the results are shown in Fig. 5.8. The recorded near-field mode profile indicated that the fiber was highly multi-mode guided at 633 and 1064 nm, and few-mode guided at 532 nm. The intensity distribution at 532 nm was simulated by summing the intensity distribution of the lowest 4 modes. The propagation loss measured with the cut-back method was 0.1 dB/cm.

Guided at 532 nm indicated that the as-grown N-SF57 clad had an index drop of 0.02, which corresponds to an annealing rate of 2.8×10^8 °C/hr. This rate was obviously unrealistic, since it was two orders of magnitude faster than the estimated upper limit. Therefore it was suspected that Eq. (5.2) is not valid with a cooling rate such high. This is possible, because the LHPG process is not in thermal equilibrium condition, which is the prerequisite of Eq. (5.2).

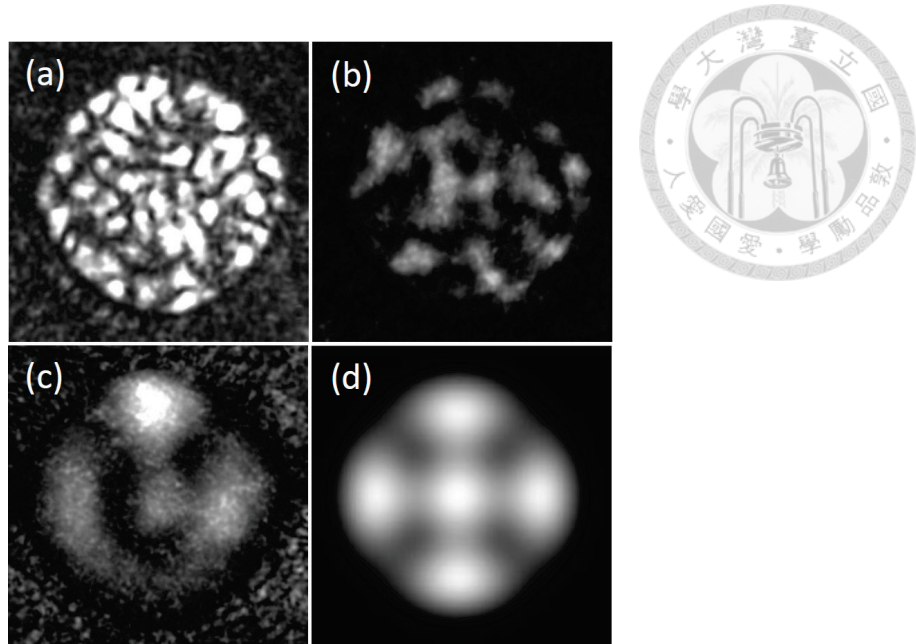


Fig. 5.8. The near-field mode profiles of the N-SF57-clad YAG crystal fiber measured at (a) 780 nm, (b) 633 nm, and (c) 532 nm. (d) Simulated profile using the intensities of the lowest 4 modes.

5.4.2 Few-Mode N-LaSF9-Clad YAG Crystal Fiber

The results of N-SF57-clad YAG crystal fiber indicated that an anomalously large index drop can be induced by the co-drawing LHPG process. Thus N-LaSF9 was chosen to be the cladding material. The refractive index of bulk N-LaSF9 is higher than YAG at all wavelengths. The index difference at 1400 nm is about 0.0067, corresponding to a cooling rate of 4.7×10^4 °C/hr based on Eq. (5.2). After the co-drawing LHPG cladding process, it is possible that the cladding index drops below the core index. If the cladding index drops too more after growth, it can be further tuned with post-growth thermal treatment [82].

N-LaSF9-clad YAG crystal fibers were fabricated. The N-LaSF9 capillary was fabricated by Schott. The inner and outer diameters of the capillary are 50 and 950 μm , respectively. A 2.1-cm long crystal fiber was prepared with a growth speed of 2 mm/min in the cladding process. The core is single-crystalline pure YAG with a 40- μm diameter. The photos of the polished end face are shown in Fig. 5.9.

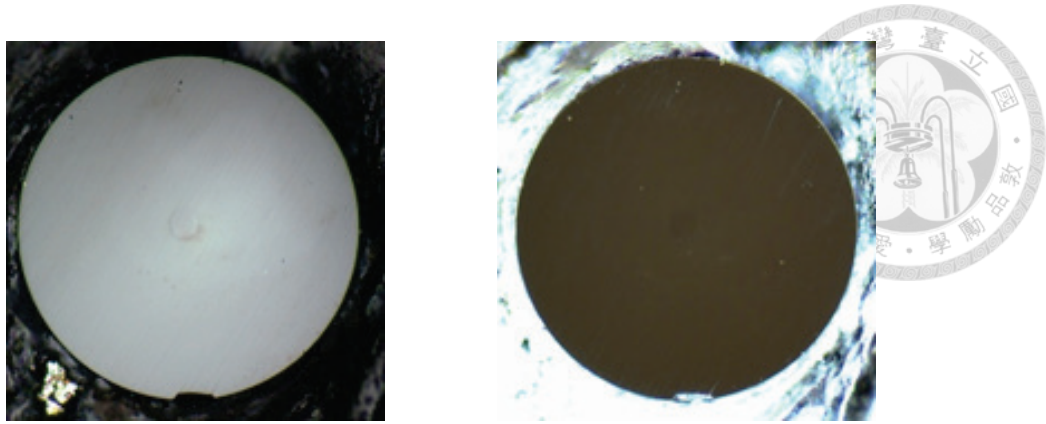


Fig. 5.9. Microscope photos of the N-LaSF9-clad YAG crystal fiber endface, (a) bright field (left), (b) dark field (right). The diameters of the fiber core and cladding are 40 and 945 μm , respectively.

The imaged near-field mode profiles of the N-LaSF9 clad fiber are shown in Fig. 5.10. The patterns are all highly-multimode at all 4 wavelengths. Guided at 532 nm indicated an index drop larger than 0.021.

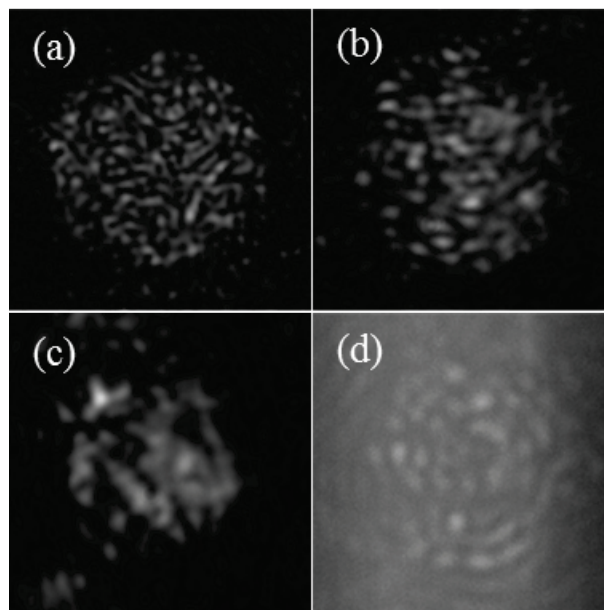


Fig. 5.10. Near-field mode profiles of the as-grown N-LaSF9-clad YAG-core fiber measured at (a) 532 nm, (b) 633 nm, (c) 780 nm, and (d) 1064 nm.

The propagation losses of the as-grown N-LaSF9-clad pure YAG crystal fiber were measured with the cut-back method. The output of the crystal fiber was butt-coupled to a multimode telecom fiber with a 50- μm core to filter out the cladding modes. The measured propagation loss was 0.87, 0.67, and 0.38 dB/cm at 657, 780, and 1064 nm, respectively. The losses were exceptionally high since typical loss of the double-clad

crystal fibers was only 0.05 dB/cm. Thus it was suspected that the fiber might not be guided.

Far-field intensity distribution of the N-LaSF9-clad crystal fiber was measured. Ring-shaped intensity distributions were captured at all wavelengths, as shown in Fig. 5.11. Therefore, the crystal fiber was actually unguided. The divergence angle of the inner rim of the doughnut cannot be determined due to the large intensity fluctuation in the speckle pattern, thus the index difference cannot be obtained from Eq. (5.5).

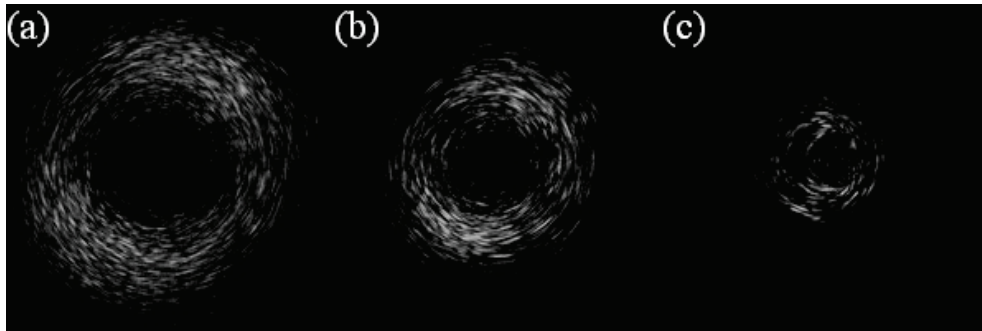


Fig. 5.11. Far-field intensity distribution of the as-grown N-LaSF9-clad pure YAG crystal fiber measured at (a) 650 nm, (b) 780 nm, and (c) 1064 nm. The growth speed was 2 mm/min.

The reason why multimode pattern was captured with the mode imaging method is possibly due to the residual rays within the core. A ray inside the core partially transmits to the cladding when it hits the core/cladding boundary. Thus the power in the core decay quickly along the fiber. The 2.1-cm length might not be long enough for the power in the core to fade out. Thus the mode imaging method is not suitable for judging whether the fiber is guided or not.

Since the N-LaSF9 crystal fiber was unguided, it was clear that the cooling rate of the 2-mm/min growth speed in the cladding process is not fast enough. Therefore, another crystal fiber with a growth speed of 10 mm/min was fabricated. The far-field intensity distribution of the sample was shown in Fig. 5.12. Ring patterns were observed at 650 and 780 nm, but not at 1064 and 1550 nm. The crystal fiber was obviously guided at 1064 and 1550 nm. The required index drop of N-LaSF9 for crystal fiber to be unguided at 780 nm and guided at 1064 nm is between 0.0082 and 0.0114.

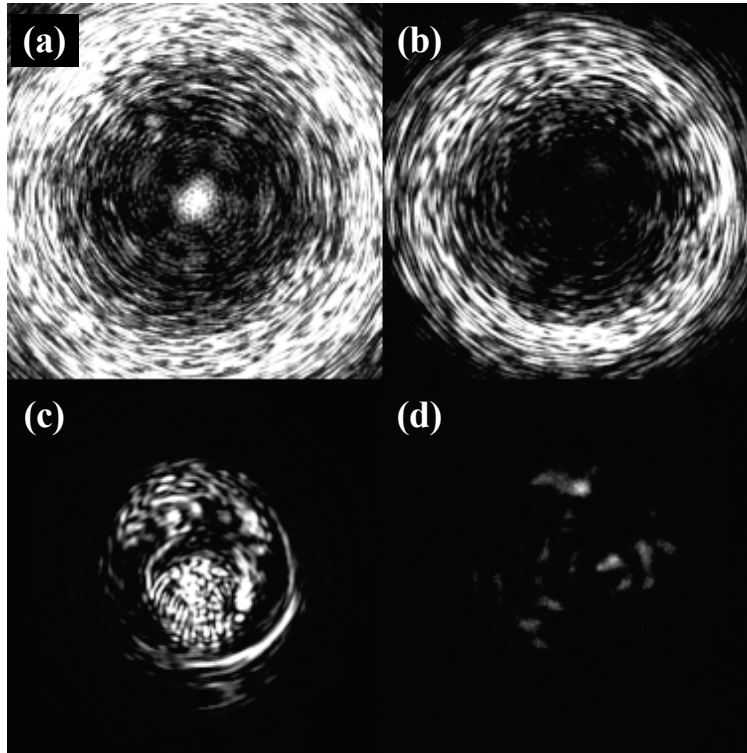


Fig. 5.12. The far-field intensity distribution of the N-LaSF9-clad pure YAG crystal fiber with a 10-mm/min growth speed at (a) 650 nm, (b) 780 nm, (c) 1064 nm and (d) 1550 nm.

Since the N-LaSF9 crystal fiber was unguided, it was clear that the cooling rate of the 2-mm/min growth speed in the cladding process is not fast enough. Faster growth speeds up to 50 mm/min have been tested. Preliminary measurements indicate that the fiber is still unguided with a growth speed of 50 mm/min.

5.5 Design of Single-Mode Cr⁴⁺:YAG Crystal Fiber

The HIGC Cr⁴⁺:YAG crystal fiber must be guided at the pump wavelength and over the emission band. Thus the fiber must be guided from 1064 nm to 1700 nm. The dispersion curves of these materials in this wavelength region are plotted in Fig. 5.13.

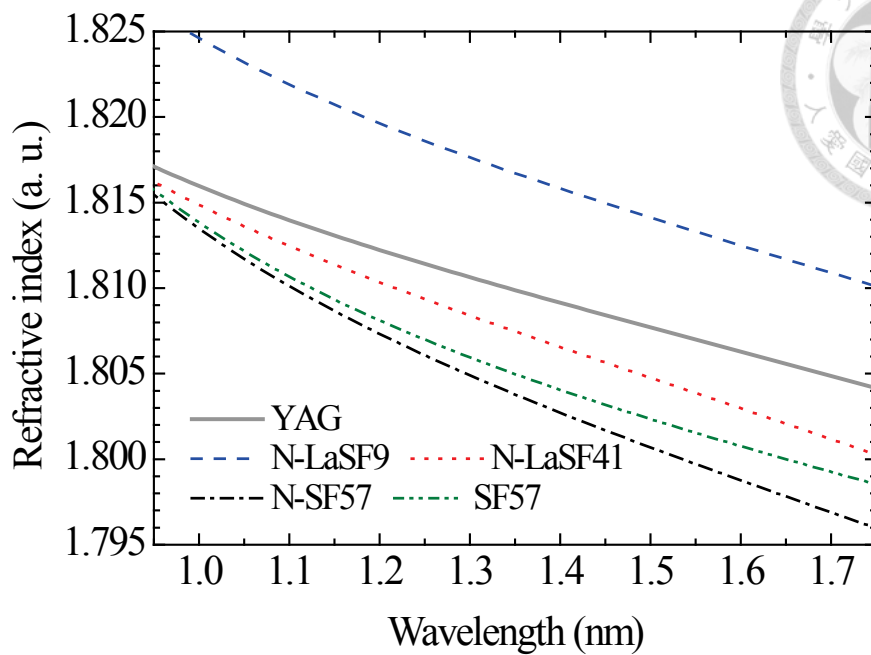


Fig. 5.13. Dispersion curves of YAG and the 4 high-index glasses from 950 nm to 1750 nm.

The cut-on wavelength of the fundamental mode is set at 1000 nm, with a 64-nm margin to the pump wavelength. For each glass, the dispersion curve were tuned up or down to shift the fundamental mode cut-on wavelength to 1000 nm. The $V-\lambda$ curves of the modified high-index glasses were calculated for different core diameters. The results are shown in Fig. 5.14–5.17.

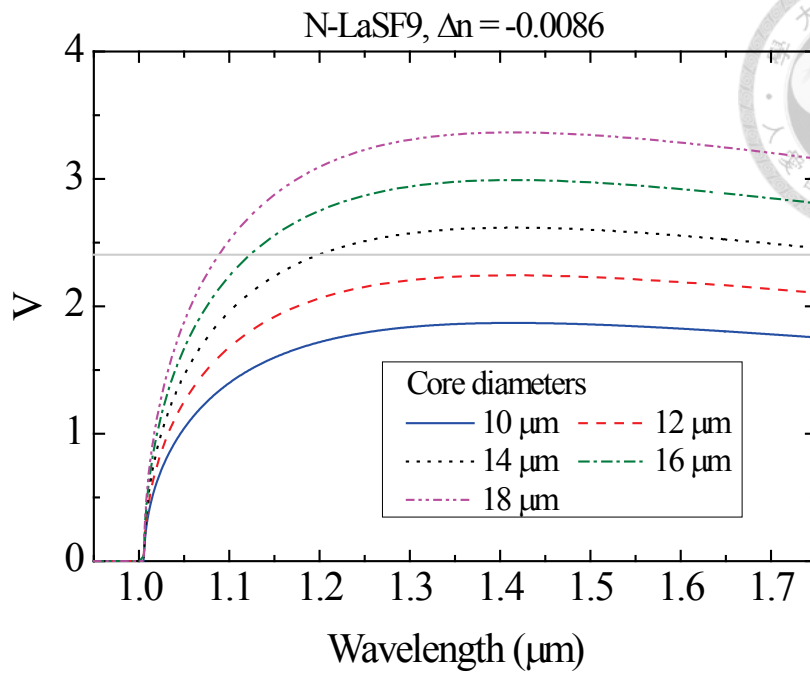


Fig. 5.14. The V values of the N-LaSF9-clad crystal fibers with an index drop of -0.0086 in the cladding due to fast annealing. The gray horizontal lines represents $V=2.405$, below which the fiber is single-mode.

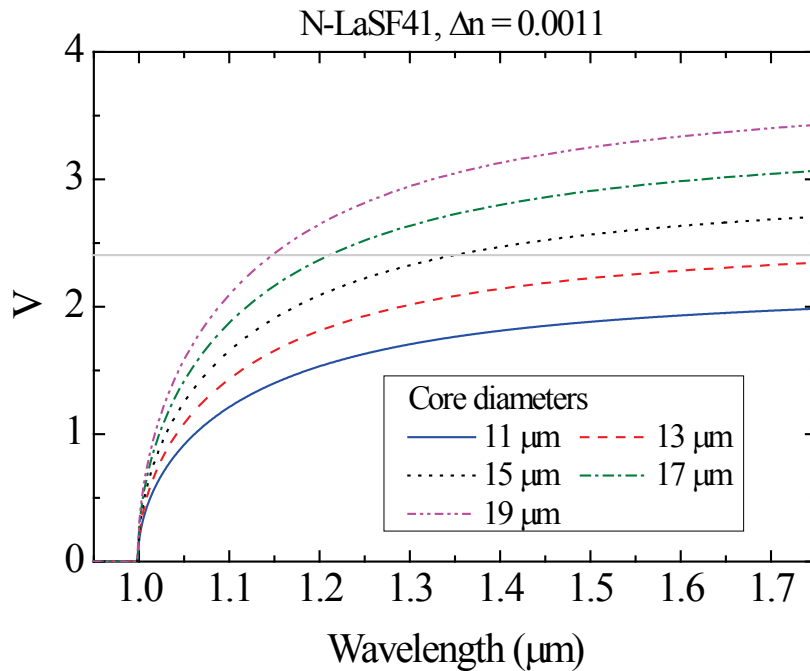


Fig. 5.15. The V values of the N-LaSF41-clad crystal fibers with an index rise of 0.0011 in the cladding due to slow annealing.

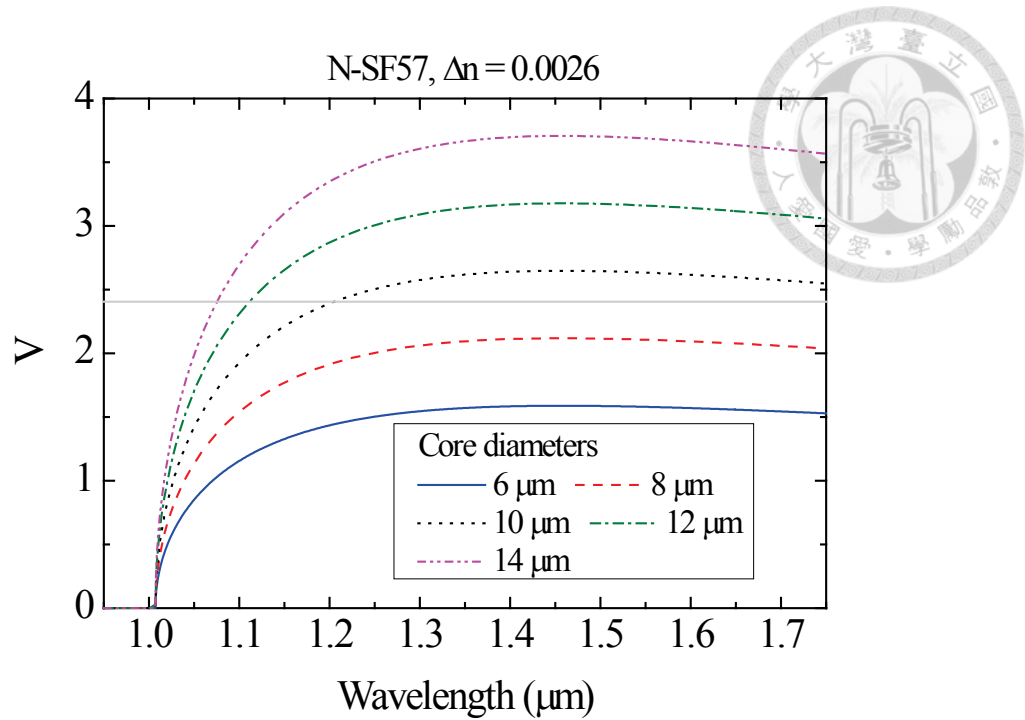


Fig. 5.16. The V values of the N-SF57-clad crystal fibers with an index rise of 0.0026 in the cladding due to slow annealing.

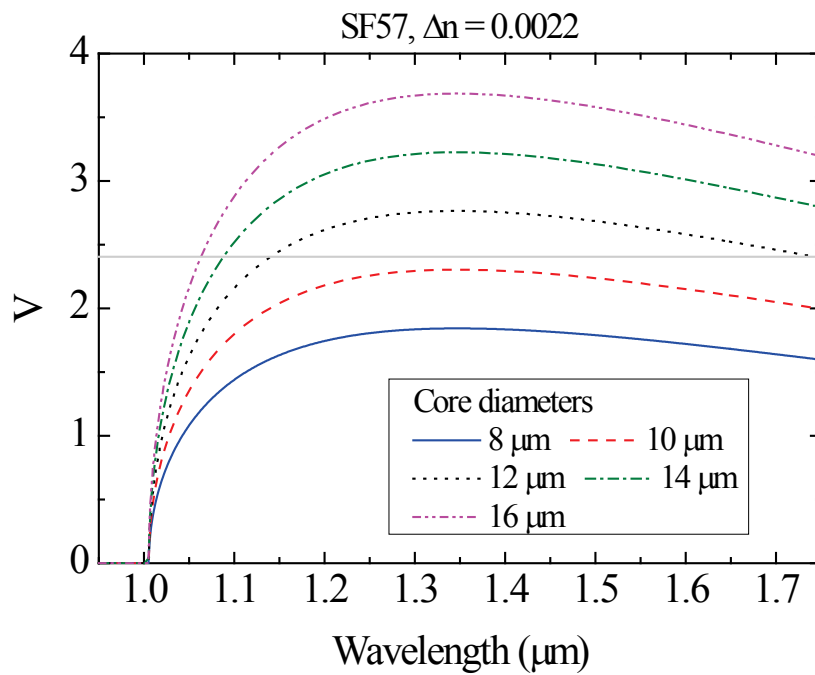


Fig. 5.17. The V values of the SF57-clad crystal fibers with an index rise of 0.0011 in the cladding due to slow annealing.

Table 5.3. Properties of the designed single-mode Cr⁴⁺: YAG crystal fibers with different high-index glass cladding.

	Core diameter (μm)	Index change	Cooling rate ($^{\circ}\text{C/hr}$)
N-LaSF9	12	-0.0086	5.75×10^5
N-LaSF41	13	0.0011	1.39
N-SF57	8	0.0026	0.72
SF57	10	0.0022	0.0005

By choosing the maximum core diameter allowing single-mode operation over 1–1.7 μm in Fig. 5.14 to Fig. 5.17, the optimized designs of all 4 high-index glasses are summarized in Table 5.3. Among the 4 glasses, SF57 is obviously not suitable since its cooling rate is unrealistically slow. N-SF57 is also not preferred due to the relatively small core diameter. The maximum single-mode core diameter is 13 μm with the N-LaSF41 cladding. This diameter is still difficult to grow, since so far the smallest diameter that can be stably grown with the LHPG system is 20 μm . The growth stability of the LHPG system must be further improved before the single-mode HIGC Cr⁴⁺:YAG crystal fiber can be realized. Although the required cooling rate of the N-LaSF9 is very fast, it has been achieved with the LHPG system, as presented in section 5.4.2. The cooling rate of N-LaSF41 is 1.39 $^{\circ}\text{C/hr}$, and the required annealing time from T_g to $T_g - 120$ $^{\circ}\text{C}$ is 86.3 hours.

In summary, N-LaSF9 and N-LaSF41 are both suitable candidate for the cladding material for the single-mode HIGC Cr⁴⁺:YAG crystal fiber. For N-LaSF9, the core diameter must be less than 12 μm , and fast anneal with the LHPG method was required. For N-LaSF41, the core diameter must be less than 13 μm , and the required post-growth annealing rate is 1.39 $^{\circ}\text{C/hr}$.

Chapter 6

Conclusions and Future Work



Diode-pumped high-brightness Ce^{3+} :YAG crystal fiber light source was successfully demonstrated. The Pyrex-cladded crystal fiber has a 20-mm length and a 25- μm core diameter. The single-crystalline core was annealed at 1000 °C for 4 hours before the cladding process. The single-direction conversion efficiency under low pump power was 1.95%, and the quantum yield was estimated to be 95%. The backward fluorescence power was enhanced 40% by attaching a broadband mirror on the opposite end of the crystal fiber to reflect both residual pump and the broadband fluorescence. The highest output power was 19.9 mW under 1.4-W pumping with only passive cooling. The output radiance is 30.3 $\text{W mm}^{-2} \text{sr}^{-1}$ in the axial direction. This light source will be very useful in the applications of optical coherence tomography.

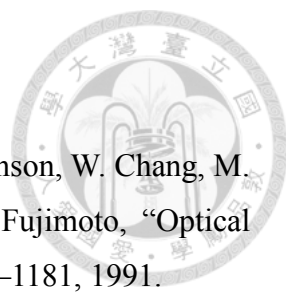
The single-direction conversion efficiency drops more than 30% under a 1.4-W pump power due to thermal quenching. The thermal dissipation can be improved by using a thinner cladding layer. Active cooling on the crystal fiber with a thermoelectric cooler will also help. The enhancement due to the broadband mirror was also lower than expected. To improve the contact to the crystal fiber end face, the broadband high-reflection dielectric coating should be used to replace the broadband mirror.

Efficient operation of the external-cavity Cr^{4+} :YAG double-clad crystal fiber laser was demonstrated with a 17.3% slope efficiency and a 56.6-mW threshold pump power. A numerical simulation with the distributed model was carried out to fit the external-cavity laser results with different output couplers. The fitted propagation loss was only 0.01 dB/cm. Tunable Cr^{4+} :YAG double-clad crystal fiber lasers were demonstrated by using the diffraction grating, the pellicle beam splitter, or the birefringent filter as the wavelength tuning element. The broadest tuning range was 156-nm with the birefringent filter, and the threshold pump power was 70 mW. Wavelength hopping due to multimode interference was observed during the wavelength tuning. The tuning characteristics can be improved by employing a single-mode crystal fiber. The performance of the Cr^{4+} :YAG crystal fiber amplifier was simulated. A 10-cm long crystal fiber amplifier with enhanced doping concentration can provide >10-dB small-signal gain from 1281 to 1622 nm under a 20-W pumping power. The peak small-signal gain is 22.7 dB at the wavelength of 1431

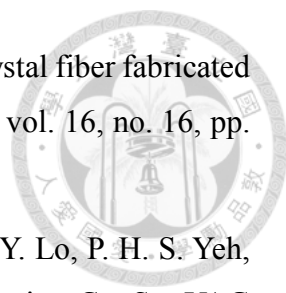
nm.


The design principle of high-index-glass-clad crystal fibers was discussed. The cladding index can be tuned up or down with slow or fast annealing from T_g to $T_g - 120$ °C, respectively. N-SF57-clad and N-LaSF9-clad pure YAG crystal fibers were fabricated with the co-drawing LHPG method. The near-field mode profiles of N-SF57-clad crystal fiber was found to be few-mode at 532 nm. The N-LaSF9-clad crystal fiber with 10 mm/min growth speed was found to be guided at both 1064 and 1550 nm, confirmed with the far-field intensity distribution. By shrinking the crystal core diameter to less than 12 μm , the N-LaSF9-clad crystal fiber can become single-mode at the wavelength range from 1 to 1.7 μm . Finally, the design of single-mode high-index-glass-clad Cr^{4+} :YAG crystal fiber was discussed. The N-LaSF41 is another suitable candidate for the cladding material. The N-LaSF41-clad crystal fiber needs to be cooled from T_g to $T_g - 120$ °C with a cooling rate of 1.4 °C per hour after the cladding process. The core diameter has to be smaller than 13 μm for single-mode operation from 1 to 1.7 μm . The tunable Cr^{4+} :YAG crystal fiber laser could be a promising light source for applications in optical communications and remote sensing once single-mode guiding is achieved.

References

- 
- [1] D. Huang, E. A. Swanson, C. P. Lin, J. S. Schuman, W. G. Stinson, W. Chang, M. R. Hee, T. Flotte, K. Gregory, C. A. Puliafito, and J. G. Fujimoto, “Optical coherence tomography,” *Science*, vol. 254, no. 5035, pp. 1178–1181, 1991.
- [2] R. Tripathi, N. Nassif, J. S. Nelson, B. H. Park, and J. F. de Boer, “Spectral shaping for non-Gaussian source spectra in optical coherence tomography,” *Opt. Lett.*, vol. 27, no. 6, pp. 406–408, 2002.
- [3] I. Hartl, X. D. Li, C. Chudoba, R. K. Ghanta, T. H. Ko, J. G. Fujimoto, J. K. Ranka, and R. S. Windeler, “Ultrahigh-resolution optical coherence tomography using continuum generation in an air–silica microstructure optical fiber,” *Opt. Lett.*, vol. 26, no. 9, pp. 608–610, 2001.
- [4] D. J. Richardson, “Filling the light pipe,” *Science*, vol. 330, no. 6002, pp. 327–328, 2010.
- [5] G. Thomas, B. Shraiman, P. Glodis, and M. Stephens, “Towards the clarity limit in optical fibre,” *Nature*, vol. 404, no. 6775, pp. 262–264, 2000.
- [6] R. J. Mears, L. Reekie, I. M. Jauncey, and D. N. Payne, “Low-noise erbium-doped fibre amplifier operating at 1.54 μm ,” *Electron. Lett.*, vol. 23, no. 19, pp. 1026–1028, 1987.
- [7] P. Doussiere, P. Garabedian, C. Graver, D. Bonnevie, T. Fillion, E. Derouin, M. Monnot, J. G. Provost, D. Leclerc, and M. Klenk, “1.55 μm polarisation independent semiconductor optical amplifier with 25 dB fiber to fiber gain,” *IEEE Photonics Technol. Lett.*, vol. 6, no. 2, pp. 170–172, 1994.
- [8] E. M. Dianov, “Amplification in extended transmission bands using bismuth-doped optical fibers,” *J. Lightwave Technol.*, vol. 31, no. 4, pp. 681–688, 2013.
- [9] G. Blasse and A. Bril, “A new phosphor for flying-spot cathode-ray tubes for color television: yellow-emitting $\text{Y}_3\text{Al}_5\text{O}_{12}\text{-Ce}^{3+}$,” *Appl. Phys. Lett.*, vol. 11, no. 2, pp. 53–55, 1967.
- [10] S. Nakamura, T. Mukai, and M. Senoh, “Candela-class high-brightness InGaN/AlGaIn double-heterostructure blue-light-emitting diodes,” *Appl. Phys.*

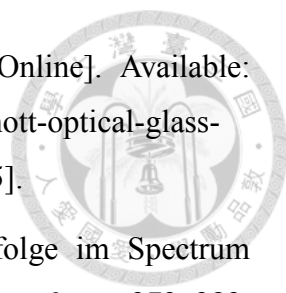
- Lett.*, vol. 64, no. 13, pp. 1687–1689, 1994.
- [11] K. Bando, K. Sakano, Y. Noguchi, and Y. Shimizu, “Development of high-bright and pure-white LED lamps,” *J. Light Vis. Environ.*, vol. 22, no. 1, pp. 2–5, 1998.
- [12] N. B. Angert, N. I. Borodin, V. M. Garmash, V. A. Zhitnyuk, A. G. Okhrimchuk, O. G. Siyuchenko, and A. V Shestakov, “Lasing due to impurity color centers in yttrium aluminum garnet crystals at wavelengths in the range 1.35–1.45 μm ,” *Sov. J. Quantum Electron.*, vol. 18, pp. 73–74, 1988.
- [13] C. Y. Lo, K. Y. Huang, J. C. Chen, C. Y. Chuang, C. C. Lai, S. L. Huang, Y. S. Lin, and P. S. Yeh, “Double-clad Cr^{4+} :YAG crystal fiber amplifier,” *Opt. Lett.*, vol. 30, pp. 129–131, 2005.
- [14] A. Petrova-Mayor, V. Wulfmeyer, and P. Weibring, “Development of an eye-safe solid-state tunable laser transmitter in the 1.4–1.5 μm wavelength region based on Cr^{4+} :YAG crystal for lidar applications,” *Appl. Opt.*, vol. 47, pp. 1522–1534, 2008.
- [15] I. T. Sorokina, S. Naumov, E. Sorokin, E. Wintner, and A. V Shestakov, “Directly diode-pumped tunable continuous-wave room-temperature Cr^{4+} :YAG laser,” *Opt. Lett.*, vol. 24, no. 22, pp. 1578–1580, 1999.
- [16] A. Sennaroglu, C. R. Pollock, and H. Nathel, “Efficient continuous-wave chromium-doped YAG laser,” *J. Opt. Soc. Am. B*, vol. 12, no. 5, p. 930, 1995.
- [17] V. Kartazaev and R. R. Alfano, “Polarization influence of excited state absorption on the performance of Cr^{4+} :YAG laser,” *Opt. Commun.*, vol. 242, no. 4–6, pp. 605–611, 2004.
- [18] D. Welford and M. A. Jaspán, “Single-frequency operation of a Cr:YAG laser from 1332 to 1554 nm,” *J. Opt. Soc. Am. B*, vol. 21, pp. 2137–2141, 2004.
- [19] M. M. Fejer, J. L. Nightingale, G. A. Magel, and R. L. Byer, “Laser-heated miniature pedestal growth apparatus for single-crystal optical fibers,” *Rev. Sci. Instrum.*, vol. 55, no. 11, pp. 1791–1796, 1984.
- [20] C. Y. Lo, K. Y. Huang, J. C. Chen, S. Tu, and S. L. Huang, “Glass-clad Cr^{4+} :YAG crystal fiber for the generation of superwideband amplified spontaneous emission,” *Opt. Lett.*, vol. 29, no. 5, p. 439, 2004.
- [21] K. Y. Huang, K. Y. Hsu, D. Y. Jheng, W. J. Zhuo, P. Y. Chen, P. H. S. Yeh, and S.

- 
- L. Huang, "Low-loss propagation in Cr⁴⁺:YAG double-clad crystal fiber fabricated by sapphire tube assisted CDLHPG technique," *Opt. Express*, vol. 16, no. 16, pp. 12264–12271, 2008.
- [22] Y. S. Lin, T. C. Cheng, C. C. Tsai, K. Y. Hsu, D. Y. Jheng, C. Y. Lo, P. H. S. Yeh, and S. L. Huang, "High-luminance white-light point source using Ce, Sm:YAG double-clad crystal fiber," *Photonics Technol. Lett.*, vol. 22, no. 20, pp. 1494–1496, 2010.
- [23] C. C. Lai, C. P. Ke, S. K. Liu, D. Y. Jheng, D. J. Wang, M. Y. Chen, Y. S. Li, P. S. Yeh, and S. L. Huang, "Efficient and low-threshold Cr⁴⁺:YAG double-clad crystal fiber laser," *Opt. Lett.*, vol. 36, no. 6, pp. 784–786, 2011.
- [24] M. Dignonnet, C. Gaeta, D. O'Meara, and H. Shaw, "Clad Nd:YAG fibers for laser applications," *J. Lightwave Technol.*, vol. 5, no. 5, pp. 642–646, 1987.
- [25] N. Ter-Gabrielyan, V. Fromzel, X. Mu, H. Meissner, and M. Dubinskii, "High efficiency, resonantly diode pumped, double-clad, Er:YAG-core, waveguide laser," *Opt. Express*, vol. 20, no. 23, pp. 25554–25561, 2012.
- [26] N. Soleimani, B. Ponting, E. Gebremichael, A. Ribuot, and G. Maxwell, "Coilable single crystals fibers of doped-YAG for high power laser applications," *J. Cryst. Growth*, vol. 393, pp. 18–22, 2014.
- [27] D. Hamilton, S. Gayen, G. Pogatshnik, and R. Ghen, "Optical-absorption and photoionization measurements from the excited states of Ce³⁺:Y₃Al₅O₁₂," *Phys. Rev. B*, vol. 39, no. 13, pp. 8807–8815, 1989.
- [28] G. Blasse and A. Bril, "Investigation of some Ce³⁺-activated phosphors," *J. Chem. Phys.*, vol. 47, no. 12, pp. 5139–5145, 1967.
- [29] V. Bachmann, C. Ronda, and A. Meijerink, "Temperature quenching of yellow Ce³⁺ luminescence in YAG:Ce," *Chem. Mater.*, vol. 21, no. 10, pp. 2077–2084, 2009.
- [30] S. Kück, "Laser-related spectroscopy of ion-doped crystals for tunable solid-state lasers," *Appl. Phys. B*, vol. 72, pp. 515–562, 2001.
- [31] D. E. McCumber, "Theory of phonon-terminated optical masers," *Phys. Rev.*, vol. 134, no. 2A, pp. A299–A306, 1964.

- 
- [32] J. M. Liu, “Laser amplifiers,” in *Photonic Devices*, Cambridge University Press, 2005, pp. 613–683.
- [33] N. I. Borodin, V. A. Zhitnyuk, A. G. Okhrimchuk, and A. V. Shestakov, “Oscillation of a $\text{Y}_3\text{Al}_5\text{O}_{12}:\text{Cr}^{4+}$ laser in wavelength region 1.34–1.6 μm ,” *Bull. Acad. Sci. USSR, Phys. Ser.*, vol. 54, no. 8, pp. 54–60, 1990.
- [34] Y. Tanabe and S. Sugano, “On the absorption spectra of complex ions. I,” *J. Phys. Soc. Japan*, vol. 9, no. 5, pp. 753–766, 1954.
- [35] H. Eilers, U. Hömmerich, S. M. Jacobsen, W. M. Yen, K. R. Hoffman, W. Jia, and U. Hommerich, “Spectroscopy and dynamics of $\text{Cr}^{4+}:\text{Y}_3\text{Al}_5\text{O}_{12}$,” *Phys. Rev. B*, vol. 49, no. 22, pp. 15505–15513, 1994.
- [36] W. Jia, H. Liu, Y. Wang, U. Hömmerich, H. Eilers, K. R. Hoffman, and W. M. Yen, “Origin of the NIR emission in Cr-doped forsterite, $\text{Y}_3\text{Al}_5\text{O}_{12}$ and Y_2SiO_5 ,” *J. Lumin.*, vol. 60–61, pp. 158–161, 1994.
- [37] B. Henderson and R. H. Bartram, *Crystal-field engineering of solid-state laser materials*. New York: Cambridge University Press, 2000, p. 119.
- [38] K. Y. Huang, “Growth system improvement and characterization of chromium-doped YAG crystal fiber,” PhD. dissertation, Institute of Electro-Optical Engineering, National Sun Yat-Sen University, 2008.
- [39] C. C. Lai, “Active crystal fiber based photonic devices,” PhD. dissertation, Graduate Institute of Photonics and Optoelectronics, National Taiwan University, 2010.
- [40] A. Sennaroglu, “Broadly tunable Cr^{4+} -doped solid-state lasers in the near infrared and visible,” *Prog. Quantum Electron.*, vol. 26, pp. 287–352, 2002.
- [41] D. Y. Jheng, K. Y. Hsu, Y. C. Liang, and S. L. Huang, “Broadly Tunable and Low-Threshold $\text{Cr}^{4+}:\text{YAG}$ Crystal Fiber Laser,” *IEEE J. Sel. Top. Quantum Electron.*, vol. 21, no. 1, p. 0900608, 2015.
- [42] S. Kück, K. Petermann, U. Pohlmann, and G. Huber, “Near-infrared emission of Cr^{4+} -doped garnets: Lifetimes, quantum efficiencies, and emission cross sections,” *Phys. Rev. B*, vol. 51, no. 24, pp. 17323–17331, 1995.
- [43] Z. Burshtein, P. Blau, Y. Kalisky, Y. Shimony, and M. R. Kikta, “Excited-state

- absorption studies of Cr⁴⁺ ions in several garnet host crystals,” *IEEE J. Quantum Electron.*, vol. 34, pp. 292–299, 1998.
- [44] A. Suda, A. Kadoi, K. Nagasaka, H. Tashiro, and K. Midorikawa, “Absorption and oscillation characteristics of a pulsed Cr⁴⁺:YAG laser investigated by a double-pulse pumping technique,” *IEEE J. Quantum Electron.*, vol. 35, no. 10, pp. 1548–1553, 1999.
- [45] X. Zhang, A. Brenier, J. Wang, and H. Zhang, “Absorption cross-sections of Cr⁴⁺:YAG at 946 and 914 nm,” *Opt. Mater.*, vol. 26, no. 3, pp. 293–296, 2004.
- [46] A. G. Okhrimchuk and A. V. Shestakov, “Absorption saturation mechanism for YAG:Cr⁴⁺ crystals,” *Phys. Rev. B*, vol. 61, pp. 988–995, 2000.
- [47] I. Shoji, Y. Sato, S. Kurimura, V. Lupei, T. Taira, A. Ikesue, and K. Yoshida, “Thermal-birefringence-induced depolarization in Nd:YAG ceramics,” *Opt. Lett.*, vol. 27, pp. 234–236, 2002.
- [48] B. E. A. Saleh and M. C. Teich, “Photons and atoms,” in *Fundamentals of Photonics*, 2nd ed., Hoboken, NJ: John Wiley & Sons, Inc., 2007, pp. 483–531.
- [49] D. Gloge, “Weakly guiding fibers,” *Appl. Opt.*, vol. 10, no. 10, pp. 2252–2258, 1971.
- [50] C. C. Lai, H. J. Tsai, K. Y. Huang, K. Y. Hsu, Z. W. Lin, K. D. Ji, W. J. Zhuo, and S. L. Huang, “Cr⁴⁺:YAG double-clad crystal fiber laser,” *Opt. Lett.*, vol. 33, pp. 2919–2921, 2008.
- [51] A. Cucinotta, S. Selleri, L. Vincetti, and M. Zoboli, “Numerical and experimental analysis of erbium-doped fiber linear cavity lasers,” *Opt. Commun.*, vol. 156, pp. 264–270, 1998.
- [52] M.-H. Kim, M. F. Schubert, Q. Dai, J. K. Kim, E. F. Schubert, J. Piprek, and Y. Park, “Origin of efficiency droop in GaN-based light-emitting diodes,” *Appl. Phys. Lett.*, vol. 91, no. 18, p. 183507, 2007.
- [53] W. R. Edmonds, “The reflexicon, a new reflective optical element, and some applications,” *Appl. Opt.*, vol. 12, no. 8, pp. 1940–1945, 1973.
- [54] X. Zeng, G. Zhao, J. Xu, H. Li, X. He, H. Pang, and M. Jie, “Effect of air annealing on the spectral properties of Ce:Y₃Al₅O₁₂ single crystals grown by the temperature

- gradient technique,” *J. Cryst. Growth*, vol. 274, no. 3–4, pp. 495–499, 2005.
- [55] Y. Dong, G. Zhou, J. Xu, G. Zhao, F. Su, L. Su, H. Li, J. Si, X. Qian, X. Li, and J. Shen, “Color centers and charge state change in Ce:YAG crystals grown by temperature gradient techniques,” *J. Cryst. Growth*, vol. 286, no. 2, pp. 476–480, 2006.
- [56] Thorlabs, “Specs of Mounted High-Power LEDs,” 2015. [Online]. Available: http://www.thorlabs.com/newgrouppage9.cfm?objectgroup_id=2692. [Accessed: 08-Jan-2015].
- [57] J. C. Chen, C. Y. Lo, K. Y. Huang, F. J. Kao, S.-Y. Tu, and S. L. Huang, “Fluorescence mapping of oxidation states of Cr ions in YAG crystal fibers,” *J. Cryst. Growth*, vol. 274, no. 3–4, pp. 522–529, 2005.
- [58] C. C. Lai, P. Yeh, S. C. Wang, D. Y. Jheng, C. N. Tsai, and S. L. Huang, “Strain-dependent fluorescence spectroscopy of nanocrystals and nanoclusters in Cr:YAG crystalline-core fibers and its impact on lasing behavior,” *J. Phys. Chem. C*, vol. 116, pp. 26052–26059, 2012.
- [59] K. Y. Hsu, D. Y. Jheng, M. H. Yang, Y. S. Lin, K. Y. Huang, Y. H. Liao, and S. L. Huang, “Bidirectionally pumped Cr⁴⁺:YAG crystal fiber light source for optical coherence tomography,” *J. Opt. Soc. Am. B*, vol. 28, no. 2, pp. 288–292, 2011.
- [60] Thorlabs, “Pellicle Beamsplitters,” 2014. [Online]. Available: https://www.thorlabs.com/newgrouppage9.cfm?objectgroup_id=898. [Accessed: 21-Nov-2014].
- [61] J. E. Antonio-Lopez, A. Castillo-Guzman, D. A. May-Arrijoja, R. Selvas-Aguilar, and P. LiKamWa, “Tunable multimode-interference bandpass fiber filter,” *Opt. Lett.*, vol. 35, pp. 324–326, 2010.
- [62] S. M. Kobtsev and N. A. Svetsitskaya, “Application of birefringent filters in continuous-wave tunable lasers: a review,” *Opt. Spectrosc.*, vol. 73, pp. 114–123, 1992.
- [63] C. N. Tsai, Y. S. Lin, K. Y. Huang, C. C. Lai, and S. L. Huang, “Enhancement of Cr⁴⁺ concentration in Y₃Al₅O₁₂ crystal fiber by pregrowth perimeter deposition,” *Jpn. J. Appl. Phys.*, vol. 47, no. 8, pp. 6369–6373, 2008.

- 
- [64] Schott, "Optical glass 2014 – pocket catalogue," 2014. [Online]. Available: http://www.schott.com/advanced_optics/english/download/schott-optical-glass-pocket-catalog-january-2014-row.pdf. [Accessed: 06-Jan-2015].
- [65] Wilhelm Sellmeier, "Zur Erklärung der abnormen Farbenfolge im Spectrum einiger Substanzen," *Ann. der Phys. und Chemie*, vol. 219, no. 6, pp. 272–282, 1871.
- [66] D. E. Zelmon, D. L. Small, and R. Page, "Refractive-index measurements of undoped yttrium aluminum garnet from 0.4 to 5.0 μm ," *Appl. Opt.*, vol. 37, no. 21, pp. 4933–4935, 1998.
- [67] Schott, "Optical glass 2014 – collection datasheets," 2014. [Online]. Available: http://www.schott.com/advanced_optics/english/download/schott-optical-glass-collection-datasheets-nov-2014-eng.pdf. [Accessed: 06-Jan-2015].
- [68] H. R. Lillie and H. N. Ritland, "Fine annealing of optical glass," *J. Am. Ceram. Soc.*, vol. 37, no. 10, pp. 466–473, 1954.
- [69] M. Ikeda, M. Tateda, and H. Yoshikiyo, "Refractive index profile of a graded index fiber: measurement by a reflection method," *Appl. Opt.*, vol. 14, no. 4, pp. 814–815, 1975.
- [70] Y. Youk and D. Y. Kim, "Reflection-type confocal refractive index profile measurement method for optical waveguides: Effects of a broadband light source and multireflected lights," *Opt. Commun.*, vol. 277, no. 1, pp. 74–79, 2007.
- [71] N. H. Fontaine and M. Young, "Two-dimensional index profiling of fibers and waveguides," *Appl. Opt.*, vol. 38, no. 33, p. 6836, 1999.
- [72] M. E. Marhic, P. S. Ho, and M. Epstein, "Nondestructive refractive-index profile measurements of clad optical fibers," *Appl. Phys. Lett.*, vol. 26, no. 10, pp. 574–575, 1975.
- [73] N. Barakat, A. A. Hamza, and A. S. Goneid, "Multiple-beam interference fringes applied to GRIN optical waveguides to determine fiber characteristics," *Appl. Opt.*, vol. 24, no. 24, p. 4383, 1985.
- [74] A. D. Yablou, "Multi-wavelength optical fiber refractive index profiling by spatially resolved Fourier transform spectroscopy," *J. Lightwave Technol.*, vol. 28,

- no. 4, pp. 360–364, 2010.
- [75] Lord Rayleigh, “The surface layer of polished silica and glass with further studies on optical contact,” *Proc. R. Soc. A Math. Phys. Eng. Sci.*, vol. 160, no. 903, pp. 507–526, 1937.
- [76] H. Yokota, H. Sakata, M. Nishibori, and K. Kinoshita, “Ellipsometric study of polished glass surfaces,” *Surf. Sci.*, vol. 16, pp. 265–274, 1969.
- [77] J. M. Bennett and R. J. King, “Effect of polishing technique on the roughness and residual surface film on fused quartz optical flats,” *Appl. Opt.*, vol. 9, no. 1, pp. 236–238, 1970.
- [78] J. Stone and H. E. Earl, “Surface effects and reflection refractometry of optical fibres,” *Opt. Quantum Electron.*, vol. 8, no. 5, pp. 459–463, 1976.
- [79] K. W. Raine, J. G. N. Baines, and D. E. Putland, “Refractive index profiling—state of the art,” *J. Lightwave Technol.*, vol. 7, no. 8, pp. 1162–1169, 1989.
- [80] F. El-Diasty, “Characterization of optical fibers by two- and multiple-beam interferometry,” *Opt. Lasers Eng.*, vol. 46, no. 4, pp. 291–305, 2008.
- [81] K. Y. Hsu, M. H. Yang, D. Y. Jheng, C. C. Lai, S. L. Huang, K. Mennemann, and V. Dietrich, “Cladding YAG crystal fibers with high-index glasses for reducing the number of guided modes,” *Opt. Mater. Express*, vol. 3, no. 6, pp. 813–820, 2013.
- [82] J. Nishimura and K. Morishita, “Control of spectral characteristics of dispersive optical fibers by annealing,” *J. Lightwave Technol.*, vol. 15, no. 2, pp. 294–298, 1997.